NASA CONTRACTOR REPORT

NASA CR-1863

MODEL TESTS OF CONCEPTS TO REDUCE HOT GAS INGESTION IN VTOL LIFT ENGINES

by Gordon R. Hall

Prepared by
NORTHROP CORPORATION
Hawthorne, Calif.
for Lewis Research Center

NATIONAL AERONAUTICS AND SPACE ADMINISTRATION • WASHINGTON, D. C. • JULY 1971

1. Report No.	2. Government Accession No.	3. Recipient's Catalog No.
NASA CR-1863		

4. Title and Subtitle	5. Report Date
MODEL TESTS OF CONCEPTS TO REDUCE HOT GAS INGESTION IN VTOL LIFT ENGINES	July 1971
	6. Performing Organization Code

7. Author(s)	8. Performing Organization Report No.
Gordon R. Hall	None
	10. Work Unit No.

9. Performing Organization Name and Address	11. Contract or Grant No.
Northrop Corporation Hawthorne, California	NAS 3-10498
	13. Type of Report and Period Covered
12. Sponsoring Agency Name and Address	Contractor Report
National Aeronautics and Space Administration Washington, D.C. 20546	14. Sponsoring Agency Code

15. Supplementary Notes

16. Abstract

An investigation was performed to determine the relative effectiveness of various exhaust gas ingestion suppression concepts for application to VTOL aircraft. The test model used in the investigation was a small-scale simulated VTOL lift engine pod containing two "engines." Ingestion control concepts included: (1) shielding devices integral with the engine pod which act to deflect the reflected upwash gases away from the inlets; (2) concepts designed to alter the issuing exhaust jets (such as exhaust vectoring and jet suppression nozzles); and (3) ground plane platforms which alter the impingement process of the exhaust jets on the ground so that the potential upwash is laterally removed from the engine proximity. Effectiveness of the various ingestion control concepts was based on comprehensive measurements of the inlet thermal environment as well as upon the effect the concept had in altering the structure of the near flow field. The majority of concepts evaluated were found to be effective in producing major reductions in exhaust gas ingestion at low wind conditions. However, none were found to be totally effective in eliminating hot gas ingestion at all wind conditions tested, particularly with the model exposed to crosswinds.

17. Key Words (Suggested by Author(s))	18. Distribution Statement
VTOL	Unclassified - unlimited

19. Security Classif. (of this report)	20. Security Classif. (of this page)	21. No. of Pages	22. Price*
Unclassified	Unclassified	157	$3.00

*For sale by the National Technical Information Service, Springfield, Virginia 22151

PREFACE

This report documents the results of an exploratory investigation of the effectiveness of various concepts designed to reduce hot gas ingestion in VTOL lift engines. The work was performed as a part of NASA Contract NAS 3-10498 entitled "Concepts to Reduce Hot Gas Ingestion in VTOL Lift Engines." This contract provided for a series of exploratory experimental investigations, the primary objective being to determine the relative effectiveness and merits of various exhaust gas ingestion suppression concepts for application to VTOL aircraft. Secondary objectives of the contract were: (1) to establish modeling criteria and test techniques required for proper simulation of full-scale VTOL recirculation and ingestion phenomena in small-scale investigations; and (2) to gain a better understanding of VTOL recirculating flow fields. Nestor Clough of the Lewis Research Center V/STOL and Noise Division was the NASA Project Manager.

The investigations were conducted with a small-scale lift engine pod model in which both dual turbojet and turbofan engines were simulated, and with a geometrically similar full-scale lift engine pod containing dual turbojet engines. Potential ingestion suppression concepts (which were limited to investigation in the small-scale tests) included: (1) shielding devices integral with the engine pod which act to deflect the reflected upwash gases away from the inlets; (2) concepts designed to alter the issuing exhaust jets (such as exhaust vectoring and jet suppression nozzles); and (3) ground plane platforms which alter the impingement process of the exhaust jets on the ground so that the potential upwash is laterally removed from the proximity of the engine pod.

Prior to performing the small-scale investigation of various ingestion suppression concepts, it was essential that the validity of small-scale investigations of recirculation and ingestion phenomena be demonstrated more thoroughly than has been demonstrated heretofore. Thus, program effort related to this objective was performed first, with the full-scale results of this effort documented separately in Reference 1 and the full-scale/small-scale scaling comparisons documented in Reference 2.

Further, it was essential to comprehensibly establish the ingestion and recirculating flow field characteristics for the baseline small-scale model prior to performing the investigation of ingestion suppression concepts. The results of this effort are documented in Reference 3.

Reported herein are the results of the evaluation of various concepts designed to reduce hot gas ingestion.

TABLE OF CONTENTS

TABLE OF CONTENTS
(Continued)

INTRODUCTION

Direct-lift turbojet or turbofan engines, as well as cruise engines with thrust deflectors, are contemplated for use as thrustors on VTOL aircraft. However, when the aircraft is in ground proximity, the engine exhaust gases, which are directed normal to the surface of the ground, can be deflected upward and ingested into the engine inlets.

Ingestion of the recirculating exhaust gases by the engines is of concern due to the rather strong effect that hot gas ingestion can have on engine performance. In particular, ingestion of hot exhaust gases by the engines results in thrust degradation. Additionally, high rates of inlet temperature rise and/or large temperature distortions across the inlet face can result in engine compressor stall. Any loss of thrust that occurs in a VTOL aircraft while it is landing or taking off can have serious consequences. Therefore, the prevention or reduction of the ingestion of hot exhuast gases in the inlets of lift engines is of critical importance in the development of VTOL aircraft.

Experimental work to date with turbojet engines operating as direct-lift thrustors has indicated that hot gas ingestion can be a serious problem (e.g., References 4-8), especially for split-engine configurations in which the location of the vehicle wing relative to the propulsion system is ineffective in shielding the engine inlets from the recirculating upwash flow. The available results also indicate that the severity of the gas ingestion is very much a function of the specific configuration of the aircraft and engine mounting arrangement. Considering the many other problems and compromises involved in the design of VTOL aircraft, it is desirable not to have to introduce further design or operation restraints, or other limitations, due to the hot gas ingestion problem. Thus, there is an incentive to investigate concepts and methods of alleviation of hot gas ingestion that are simple in principle, and that can be made relatively independent of the specific aircraft configuration.

One such approach would be to incorporate some form of shielding device integral with, or in proximity of, the engines which would act to deflect the reflected upwash gases away from the engine inlets. Another approach would be incorporation of concepts designed to alter the issuing exhaust jets, such as inclination of the engine exhausts from vertical or the use of special jet suppression nozzles that promote rapid

mixing of the hot exhaust jet with the surrounding air, thus reducing the jet velocity and temperature at impingement. The above concepts represent devices which could be regarded as part of the aircraft propulsion system. Another approach to reducing the ingestion of hot exhaust gases is the development of ground surface platforms that alter the impingement process of the exhaust jets on the ground so that the potential upwash is laterally removed from the engine proximity, or otherwise act to reduce the strength and temperature of the upwash flow. This approach would apply primarily to operations from prepared or permanent landing sites.

Reported herein are the results of an investigation to determine the effectiveness of various exhaust gas ingestion suppression devices designed to operate by the principles outlined above. The basic test model (henceforth referred to as the reference model) of the investigation was a small-scale simulated VTOL lift engine pod containing two "engines." This model was tested alone and then with various ingestion suppression concepts. For each ingestion suppression concept, the relevant parameters associated with the concept were investigated at fixed operating conditions of the reference model (i.e., fixed model exhaust condition, model height above the ground plane, and low external wind). Following these tests, a favorable combination of parameters was selected for each ingestion suppression concept for further tests. For these tests, operating conditions of the reference model were varied (i.e., model exhaust conditions, model height above the ground plane, and external wind speed and direction).

SYMBOLS

d	Air curtain slot width
D	Nozzle diameter
h	Air curtain slot location with respect to model inlet plane
H	Height of model undersurface above ground plane (or above ground plane platform)
H_o	Height of ground plane platform above ground plane
L	Shield, or air curtain slot, length
P	Pressure
ΔP	Pod pressure minus ambient pressure
q	Jet stagnation pressure minus ambient pressure
r	Distance from nozzle centerline
R	Nozzle radius
T	Temperature
W	Shield width
Z	Vertical distance from nozzle exit
α	Air curtain slot angle relative to horizontal (positive downward)
β	Exhaust jet angle relative to vertical in the fore-aft plane of the model
γ	Exhaust jet angle relative to vertical in the right-left plane of the model
σ	Ground plane grate porosity (percent open area)
ϕ	Air curtain flowrate (two sides)/nozzle flowrate (two nozzles)

Ingestion Indices

$\overline{T}$	Instantaneous spatial average inlet temperature. $\overline{T} = \frac{1}{n}\sum_{i=1}^{n} T_i$
$\Delta\overline{T}$	Instantaneous spatial average inlet temperature increment above ambient, $\overline{T} - T_\infty$
ϵ	Instantaneous temperature distortion within inlet, $T_{max} - T_{min}$
$\dot{\overline{T}}$	Instantaneous rate of rise of spatial average inlet temperature

Subscript

n	Nozzle
∞	Ambient
c.l.	Centerline

Superscript

$\wedge$	Time-average (applied to $\Delta\overline{T}$, ϵ, and $\dot{\overline{T}}$)

TEST FACILITY AND MODEL

Test Facility

The tests were performed at Northrop Corporation, Aircraft Division, VTOL Ground Effects Test Facility. A brief description of this facility is given below, with Reference 9 providing details of the design features and performance capabilities.

Figures 1 and 2 show the facility and model support system. Test models are centrally located with respect to a 40' x 40' smooth and level ground plane located 30" above earth level. Directly below the model is a 14" x 30" trap door through which the exhaust jets flow during temperature stabilization of the model and ducting system. Beneath the trap door is a deflector which diverts the exhaust flow outward beneath the ground plane.

Test models are mounted on a cantilever structure supported by a tripod base. Simulated engine exhaust flow is supplied from bottles of compressed air (Figure 1) and heated to the desired exhaust temperature (up to 1200°F) in passing through a pebble bed heater enroute to the model. Simulated engine inlet flow is induced by a vacuum system. The model exhaust and inlet flows are routed along and through, respectively, the support structure. Vertical position of the model (or continuous motion simulating take-off/landing transients) is accommodated by telescoping assemblies in the exhaust nozzle supply lines and by a flexible hose in the inlet suction lines.

The test area is large enough, and sufficiently vented, to avoid heating of the local "external" environment during periods of sustained testing. Additionally, all vertical obstructions are far enough removed from the exhaust jet source to avoid "jet reflection" effects. Wind protection in the test area is afforded by surrounding buildings and by installation of canvas wind screens (15' high) at the north and west ends of the test area as indicated in Figure 1. With the wind screens installed, local wind conditions within the test site are suppressed to levels typically less than 3 mph during the morning and early afternoon.

Airflow to simulate wind effects is supplied from a 9' x 12' duct which terminates near the edge of the ground plane. The drive system of the wind generator is an ejector concept which provides secondary to primary airflow in the ratio of about 80 to 1, the secondary air being drawn from the atmosphere and the primary air being provided by

the same bottles of compressed air which supply the model exhaust flow. Uniform, low turbulence winds in excess of 30 mph can be provided. Orientation of test models with respect to wind direction is achieved by rotation of the model support system.

Reference Model

The reference model, a simulated VTOL lift engine pod containing two "engines," is shown in Figures 3 and 4. The nominal spacing between the two engines, S, in terms of the 2.25" nozzle diameters, D, was S/D = 7.35.

Figures 5 and 6 show details of the model inlets and basic exhaust nozzles. Centerbodies were provided in order to give close simulation of full-scale inlet and nozzle flows. The inlet flow rate, with the inlets operating at a nominal inlet Mach number of 0.5, was approximately equal to the exhaust nozzle flow rate, when operating at the nominal turbojet exhaust pressure ratio of $P_n/P_\infty = 1.9$ and nominal exhaust temperature of 1200°F.

A perforated plate (.05" holes) was used to separate the exhaust flow supply duct from the nozzle chamber (Figure 6). The plate served to drop the pressure between the supply duct (≈ 80 psia) and the nozzle chamber (≈ 26 psia), thereby allowing a smaller supply duct cross section than would otherwise be required. The plate also eliminated problems of exhaust flow misalignment which would have been severe without the plate.

Inlet suction and exhaust flow were supplied at each end of the model with an internal partition separating the forward "engine" flow from the aft "engine" flow. Air suction systems at each end of the model were essential in order to attain the desired inlet flow without geometric distortion of the model, distortion being necessary to accommodate the duct size required for a "single end" suction system.

Heat absorption by the model (and therefore model heating and cooling time) was minimized by insulating the model structure from the hot exhaust flow. The insulation resulted in maximum model structure temperatures (with exception of the nozzle) of about 400°F.

Ingestion Suppression Concepts

Various concepts to reduce hot gas ingestion in the reference model were investigated. Specific ingestion suppression concepts included: (1) shielding devices integral with the engine pod which act to deflect the upwash gases away from the inlets; (2) concepts designed to alter the issuing exhaust jets; and (3) ground plane platforms which alter the impingement process of the exhaust jets on the ground so that the potential upwash is laterally removed from the proximity of the model. Details of the various concepts are provided in subsequent discussions which separately report the results for each of the concepts.

INSTRUMENTATION

1. Inlet Temperatures - The inlets of the reference model were instrumented with twelve high-response bare-bead thermocouples. The locations of the thermocouples were selected to represent equal flow areas within the inlet. The output of these thermocouples was recorded on FM magnetic tape.

The locations and details of construction of the inlet thermocouples are shown in Figures 5 and 7. The sensing element of the thermocouples was fabricated from .003" chromel/alumel wire. Based on Reference 10, the time constant for the thermocouple/flow environment combination was approximately 18 m.s. (or in terms of response to a sinusoidal input signal, flat response within 10 percent up to a frequency of about 5 cps), assuming an ideal butt weld junction through which the local thermal mass is not increased above that of the parent wire. Details of the design considerations relating to the construction concept, junction wire size, junction material, and operational reliability are given in Reference 1.

2. Inlet Proximity Temperatures - Twelve high response bare-bead thermocouples (identical to those in the inlets) were cantilevered from the sides of the model in the plane of the inlets (Figure 8). These thermocouples, which were recorded on oscillograph, were located to measure the temperature (and longitudinal concentration) of the upwash flow between the engines.

3. Pod Pressures - Pressure taps were located on the lower surface of the model along the longitudinal centerline (Figure 9). These pressure measurements provided information on the strength and location of the upwash flow between the exhaust jets.

4. Exhaust Measurements - Exhaust nozzle pressure and temperatures were measured with high response sensing elements (three per nozzle ganged together for a single output) and recorded on oscillograph. Figures 6 and 10 show instrumentation detail for the basic nozzle configuration.

5. External Wind - External wind speed, azimuth, and elevation were monitored prior to testing and recorded continuously on oscillograph during the tests.

PROCEDURE

Exhaust Jet Calibration

Prior to conducting recirculation tests, calibrations of the jet exhausts were made for the basic exhaust nozzles of Figures 6 and 10. These calibrations are relevant to subsequent recirculation effects. This was borne out in the findings of Reference 11 which demonstrated that recirculation effects are extremely sensitive to jet exit angles and moderately sensitive to jet dynamic pressure decay (i.e., turbulence).

Jet Pressure Profiles - Dynamic pressure profiles (i.e., jet total less ambient pressure) of the jets were measured at various distances, Z, from the nozzle exit using a cruciform pressure rake with probes aligned to measure the jet pressure profiles in the fore-aft plane and in the right/left plane. Measurements were made from the nozzle exit up to Z/D of about 10, with the rake aligned such that the centerprobe of the cruciform was approximately coincident with a plumb line suspended from the nozzle centerline. The measurements were taken at the nominal turbojet exhaust pressure ratio of $P_n/P_\infty = 1.9$ and nominal exhaust temperature of 1200°F.

The dynamic pressure profiles, q, nondimensionalized with respect to the dynamic pressure measured within the nozzle, q_n, are shown in Figure 11. The depression in the dynamic pressure in the central region of the jets at lower values of Z/D is indicative of flow separation from the nozzle centerbody. At larger values of Z/D, the relatively localized effects of the centerbody are not apparent, with the pressure profiles resembling a distribution characteristic of the asymptotic profiles for a conventional open nozzle.

Figure 12 shows the variation in jet centerline dynamic pressure with Z/D. For comparative purposes, the dynamic pressure decay for a 3" open nozzle supplied by a plenum (i.e., low initial turbulence level) is also shown. Resevoir conditions for the reference nozzle (Reference 12) were $T_n = 1200°F$ and $P_n/P_\infty = 2.0$. The effect of the nozzle centerbodies is clearly apparent at the smaller values of Z/D. At the larger values of Z/D, the rate of dynamic pressure decay is seen to be similar to that of the small-scale reference nozzle.

Jet Alignment - At the larger values of Z/D, a small offset of the dynamic pressure peak from vertical (i.e., r/R = 0) is generally observed in Figure 11. These offset values in the dynamic pressure profiles were used to determine the alignment of the jets relative to vertical, assuming the jet centerline to be defined by the locus of the dynamic pressure peaks. Based on this method, the maximum misalignment of the jets relative to vertical was determined to be less than one degree.

Alternate methods to determine the alignment of the jets were also employed. For example, Figure 13 shows the results of an oil streak technique in which a small pool of oil (approximately equal to the nozzle exit diameter) was placed on the ground plane directly below each of the nozzles. The jets were then turned on, allowing the oil to smear under the viscous action of the radially spreading ground jets. The resulting pattern is essentially radial, except in the region of the interaction plane midway between, and perpendicular to a line joining, the nozzle centerlines. In this region, the opposing ground jet flows meet and are turned outward and upward.

Also indicated in Figure 13 is a vertical projection of the nozzle centerline. Based on the displacement of the jet stagnation points (i.e., convergence point of the radial streak lines) from the vertical projection of the nozzle centerlines, and on the height of the model above the ground plane, the jet misalignment from vertical may be determined. Based on this method, which was performed at reduced exhaust pressure and temperature conditions, the jet alignment, relative to vertical, as before, was determined to be slightly forward and to the right with a resultant misalignment of less and one degree.

Figure 14 shows a flow visualization photograph of the issuing jets with the ground plane trap door open. The visualization was obtained by injecting a small quantity of oil into the hot jets at the nozzle exit, thereby resulting in vaporization and combustion. Although less accurate than the preceding techniques of determining the jet alignment, the results tend to confirm the previous misalignment values. Additionally, the jet spreading as indicated in Figure 14 is in good agreement with the quantitative jet spreading data of Figure 11.

Test Conditions

Five different ingestion suppression concepts were investigated. A detailed description of each of the concepts, and associated test conditions, is provided in subsequent discussions wherein the results obtained with each of the concepts are reported separately. In addition, tests were conducted with the reference model to obtain baseline data from which to evaluate the effectiveness of the various suppression devices.

The test plan format for each of the suppression concepts were generally similar, with the testing occurring in two phases. The first phase was devoted to investigation of suppression concept design variables at fixed model operating conditions (i.e., fixed H/D and low wind conditions). The second phase was devoted to evaluation of one specific suppression configuration selected from each of the five concepts over a range of model heights (H/D) and wind conditions.

Both the reference model and model configurations employing ingestion suppression devices were tested predominately at simulated turbojet exhaust conditions of $P_n/P_\infty = 1.9$ and $T_n = 1200°F$. In addition, numerous tests were performed at simulated turbofan exhaust conditions of $P_n/P_\infty = 1.4$ and $T_n = 440°F$.

Test Procedure

Prior to each of the tests, external wind conditions were monitored. For the nominally "no wind" tests, wind conditions were less than 3 mph within the test area. For the "wind" tests, wind velocity was controlled using the wind generator described previously.

Quantitative Data - Once the desired ambient wind condition was attained, the inlet suction system was set to give an inlet Mach number of 0.5, after which time the model and test facility ducting was preheated to the desired operating temperature. Upon establishing the desired pre-run exhaust conditions, the wind generator was set to give the desired wind velocity, after which time data acquisition was initiated and the ground plane trap closed (trap door closure time was about 150 m.s.). Data acquisition subsequent to trap door closure was typically 40 seconds.

Flow Field Evaluation - In addition to the quantitative data obtained at full exhaust temperature, qualitative evaluations of the structure of the near flow field in the proximity of the model were made at reduced exhaust temperatures for many of the configurations tested. Sketches were made showing the relevant features of the near flow field for each of the configurations evaluated. These sketches were based on combined information obtained from: (1) streamline, turbulence, and stagnation point information obtained by localized smoke injection into the flow field from a smoke gun; (2) manual surveys of the flow field; and (3) tuft patterns.

These flow field evaluations provided valuable insight into the effect of the various ingestion suppression devices in altering the structure of the near flow field from that of the reference model. The results obtained from these evaluations were generally consistent with the results of the quantitative ingestion data. That is, ingestion suppression devices which were found to be effective in significantly reducing the upwash flow in the region of the inlets were also found to be effective, as one would expect, in significantly reducing ingestion levels.

Data Reduction

Data reduction techniques applied to the inlet temperature data were oriented toward statistical analyses due to the random, or sporadic, nature of the data. For data of this type, a statistical oriented approach to data analysis is essential for objective characterization of the data.

As noted previously, the inlet temperatures were sensed with high response thermocouples and recorded on magnetic tape. For each of the tests, the raw inlet temperature data were played back on analog tapes. In addition, the following temperature indices, yielding quantitative information on the inlet temperature levels, temperature distortion, and temperature rate of rise, were computed from the raw data using a Comcor 175 Analog Computer.

(1) The instantaneous spatial average of the n individual temperatures within the inlet:

$$\overline{T}(t) = \frac{1}{n} \sum_{i=1}^{n} T_i(t)$$

(2) The cumulative time-average of (1).

(3) The instantaneous temperature distortion within the inlet:

$$\epsilon(t) = T_{max}(t) - T_{min}(t)$$

(4) The cumulative time-average of (3).

(5) The instantaneous rate of rise of (1):

$$\dot{\overline{T}}(t) = \frac{d\overline{T}}{dt}$$

(6) The cumulative time-average of the absolute value of (5).

REFERENCE MODEL

Ingestion and recirculating flow field characteristics for the reference engine pod model, without ingestion suppression devices, are presented in this section. These data are taken from Reference 3 [1] and repeated here to provide the reader with basic insight into the steady state ingestion and recirculation characteristics of the reference model, thus forming a base point for evaluation of the effectiveness of the various ingestion suppression devices, as well as an understanding of the data analysis techniques, which were similar for all the data.

As noted previously, both the reference model and configurations employing ingestion suppression devices were tested predominately at simulated turbojet exhaust conditions of $P_n/P_\infty = 1.9$ and $T_n = 1200°F$. In addition, numerous tests were performed at simulated turbofan exhaust conditions of $P_n/P_\infty = 1.4$ and $T_n = 440°F$. The general character of the data and the relative effectiveness of the various ingestion suppression devices were found to be similar for turbojet and turbofan exhaust conditions, with differences being in the absolute levels of the data rather than in the general character of the data or in the relative effectiveness of the ingestion suppression device. Accordingly, in the discussions which follow, data are presented exclusively at turbojet exhaust conditions with the discussion of the data being generally applicable to more generalized exhaust conditions.

Ingestion Characteristics

Figure 15 through 17 show time histories which illustrate the basic character of the inlet thermal environment, including the effect of wind, for the reference model without ingestion control devices. The data were obtained by playback of the raw data from magnetic tape.

---

[1] Reference 3 provides a complete account of the reference model in terms of the transient development of the recirculating flow field, steady state ingestion and recirculation flow field characteristics, and dynamic simulation of take-off and landing.

Although the data presented are for H/D = 4, they are generally characteristic of operation at other values of H/D, with differences being predominately in the levels of the data rather than in the general character of the data. The data are also representative of full scale ingestion characteristics as seen in Reference 1 which reports the ingestion characteristics of a geometrically similar, and similarly instrumented, full-scale engine pod model.[1]

Low Wind - For low wind conditions (Figure 15) in which the exhaust gas ingestion is dominated by the upwash, or fountain, resulting from mutual interaction of the jets and the ground plane (Figure 13), several general characteristics of the data are immediately obvious. First of all, it is observed that the forward inlet is essentially at the pre-run ambient temperature throughout the test with the exception of some occasional temperature spikes after trap door closure (i.e., t = 0). In contrast, the aft inlet is significantly above the pre-run ambient temperature throughout the test.

Nonsymmetrical distribution of exhaust ingestion by the inlets as indicated by Figure 15 was also found to be typical at low wind conditions at other values of H/D, and found to occur in full-scale tests with a similar configuration (Reference 1). Due to geometric symmetry of the model in the region between the inlets, the ingestion prone inlet was found to vary from test to test. In a few tests, the ingestion was found to shift from one inlet to the other within the test.

The nonsymmetrical distribution of exhaust gas ingestion in a configuration with geometric symmetry at low wind conditions is the result of the low stability characteristics of the upwash, which when coupled with the inlet suction flow field, results in a fluid amplifier effect. The net result occurring within the combined upwash/inlet flow field is an unstable upwash flow which is entrained, predominately, within one inlet or the other as indicated in Figure 18, the particular inlet depending upon small biases such as slight differences in the exhaust jet pressure levels, minor angular misalignment of the jets with respect to the ground plane, and random wind effects. For more

[1] Detailed comparisons of full-scale/small-scale recirculation characteristics as related to scaling are presented in Reference 2.

detailed discussion of these effects on upwash stability, the reader is referred to Reference 11. For discussion of additional aspects of nonsymmetrical ingestion as related to full-scale tests, the reader is referred to Reference 1.

Another obvious characteristic of the data of Figure 15 is the sporadic nature of the inlet temperature environment. Temperature spikes are observed which typically persist for a small fraction of a second, and frequently reach levels in excess of 100°F above ambient. These temperature spikes, or pulses, are sometimes very local in nature, as evidenced by simultaneous response of only a few thermocouples, while at other times they are observed to encompass a large section of the inlet as evidenced by simultaneous response of the majority of the thermocouples. During time intervals between temperature spikes, the temperature level is typically ambient. In no test was a prolonged temperature rise observed which could be considered a "steady" temperature, rather than a series of closely spaced temperature pulses.

Similarly, the upwash temperature environment in the proximity of the inlets, as measured by the instrumentation indicated in Figure 8,was found to exhibit temperature fluctuation characteristics much like those of the inlets. The inlet proximity traces, however, were found to be considerably "smoother" than the inlet traces due to the lower velocity of the flow past the thermocouples, the flow velocity affecting both the thermocouple response and passage time of hot gas bubbles for a given spatial temperature gradient. The result is that local fluctuations in the range of 50°F - 100°F were observed, with peak fluctuations up to about 150°F. Further, the relative level of thermal activity in the proximity of the inlets was found to correlate with the inlet environment in that the activity in the proximity of the ingestion prone inlet was found to be considerably greater than that in the proximity of the non-ingestion prone inlet.

Analysis of the inlet and inlet proximity thermal environments suggests an upwash model composed predominately of large clumps of hot gas (as evidenced by the simultaneous response of several inlet proximity thermocouples). In approaching the inlet, acceleration of the flow results in stretching of the clumps, or bubbles, into elongated stream tubes which may occupy anywhere from a very small fraction of the inlet cross section to the major portion of the inlet cross section.

Headwind - Figure 16 shows the inlet temperature environment with a 20 mph headwind. Major reduction in ingestion levels from the low wind data of Figure 15 is

observed. Specifically, the forward inlet (i.e., upstream with respect to the wind) shows minor temperature pulses, typically less than 25°F, distributed over the entire inlet. The aft inlet (i.e., downstream with respect to the wind) typically shows somewhat sharper, higher level, temperature pulses which are more spatially localized.

The more uniform temperature pulses observed in the forward inlet indicate a well mixed flow of exhaust gases which are swept up from the ground plane in the far field and blown back over the model. The sharper, more lozalized pulses of the aft inlet indicate an upwash which, although predominately suppressed and deflected by the wind, are occasionally entrained within the inlet flow.

Crosswind - Figure 17 shows the inlet temperature environment with a 20 mph crosswind. The fluctuating character of the data observed at low wind continues to persist at crosswind conditions. The ingestion is more severe and, unlike the low wind data, was found to be relatively evenly distributed within the two inlets. The increased severity and the relatively symmetrical distribution of ingestion in both inlets were found to be typical at all values of H/D for crosswind conditions.

Ingestion Indices

Instantaneous Indices - Figures 19 through 21 present time histories of the spatial average inlet temperature ($\overline{T}$), the temperature distortion within the inlet (ϵ), and the rate of rise of the spatial average temperature ($\dot{\overline{T}}$), obtained from the raw data of Figures 15 through 17.

Since the temperature spikes observed in the raw data are generally localized, the corresponding peak values of $\overline{T}$ are accordingly less than the localized peak values of the individual temperatures observed in the raw data. Thus, traces of $\overline{T}$, while still rather sporadic in nature, are considerably smoother than the individual temperature traces of the raw data. The generally localized nature of ingestion is also indicated by the distortion parameter, ϵ, which frequently shows large values of temperature distortion without significant increase in $\overline{T}$ above the pre-run ambient temperature level.

Cumulative Time-Averages - The instantaneous temperature indices for each of the tests were cumulatively time-averaged in order to provide a single run-average

index for each of the fluctuating quantities $\overline{T}$, ϵ, and $\dot{\overline{T}}$. These time-average quantities were obtained by continuous integration and division by time using an analog computer, the computing process beginning 2 seconds following trap door closure and continuing for 30 seconds thereafter.[1] For the case of $\dot{\overline{T}}$, the integral taken was that of the absolute value rather than of the algebraic value (the integral of the algebraic value of $\dot{\overline{T}}$ must be zero unless there is a net increase in $\overline{T}$ with time).

The cumulative time average of $\overline{T}$, ϵ, and $\dot{\overline{T}}$ were found to be independent of time. That is, although the quantities $\overline{T}$, ϵ, and $\dot{\overline{T}}$ are of a sporadic nature on a short time basis, there is no net change (i.e., no "long time" time-dependence) in the average value of these quantities over the duration of the tests. Thus, run-average indices, which are independent of time and representative of inlet temperature level ($\hat{\Delta\overline{T}}$), temperature distortion ($\hat{\epsilon}$), and temperature rate of rise $|\hat{\dot{\overline{T}}}|$, are provided for each of the steady state tests.

Ingestion Levels - Figures 22 and 23 show ingestion trends in terms of the above-described run-average indices $\hat{\Delta\overline{T}}$, $\hat{\epsilon}$, and $|\hat{\dot{\overline{T}}}|$. The data shown are for the ingestion prone inlet except at crosswind conditions. At crosswind conditions, the distribution of ingestion between the two inlets was found to be relatively equal (as discussed previously) in which case the data represent the average value for the two inlets.

Figure 22 shows the effect of H/D on ingestion. Ingestion is seen to generally decrease with H/D with the exception of a hump in the curves in the region from H/D = 4-6. This hump was also observed in the full-scale/small-scale results of Reference 2 for engine pod models similar to the engine pod model reported herein.

Figure 23 shows the effect of wind on ingestion. The data show significant reduction in ingestion for headwinds greater than about 10 mph, with ingestion becoming negligible at about 20 mph as discussed previously for the time histories of the raw inlet temperature data.

---

[1] In a few tests, the ingestion was found to shift from one inlet to the other during the test. For these tests, the averaging was performed over a suitable time interval during which the ingestion remained stabilized within one inlet.

The effect of crosswind, however, is adverse (also discussed previously for the time histories of the raw inlet temperature data). The inlet temperature level ($\Delta\bar{T}$) is seen to increase with increasing wind speed, until at 30 mph, the level becomes about three times more severe than the low wind level. The effect on temperature rate of rise ($|\dot{\bar{T}}|$) is even greater. The distortion (ϵ), however, is relatively unaffected by the crosswind. This is due to the fact that much of the ingestion occurring with crosswind results from backflow of well mixed exhaust gases across the model.

Pod Pressure Distribution

Upwash Flow Field - At low wind conditions, the ground jets in the region between the engines flow toward one another, eventually interacting in the plane midway between the jet centerlines (Figure 13). Within the interaction process, the ground jet flows are turned outward and upward as indicated in Figure 24. The upward flow continues unimpeded until reaching the undersurface of the pod, where it impinges and is deflected around, and up, the sides of the pod.

It is noted that although ingestion was generally found to be significant in one engine or the other for two engine operation, but not in both, the upwash between the ground plane and the pod was found to be relatively symmetrical, with the upwash asymmetry discussed previously occurring between the pod undersurface and the plane of the inlets as indicated in Figure 18.

The upwash of exhaust gases produces a pressure field on the vehicle undersurface which can, in general, result in significant force levels when considering the total surface area affected. Characteristic of the pressure distribution for two engine operation is a positive pressure field approximately midway between the engines, with a negative pressure field on either side, the level of the pressure field being strongly dependent on H/D. The positive pressure field results from impingement of the upwash flow, or fountain, on the pod at velocities in excess of 200 fps at the lower values of H/D. The negative pressure field on either side of the positive pressure field results from high mass flow entrainment by the jets (and, to a lesser extent, entrainment by the upwash flow), coupled with limited area from which to draw the free air necessary to satisfy the scavenging characteristics of the jets (Figure 24).

Effect of H/D - Figures 25 and 26 show the effect of H/D on the pressure field on the undersurface of the pod. The data show a rapid decline in the strength of the upwash with increasing H/D, primarily due to the increase in path length, and associated mixing of the exhaust gases in traveling from the exhaust nozzle to the undersurface of the pod. In addition, the entrainment field of the free jets has a significant retarding effect on the upflow of exhaust gases, the effect increasing with increase in H/D.

Effect of Wind - Figures 27 and 28 show the effect of wind speed and direction on the pod undersurface pressure field. The data show significant reductions in the strength of the upwash with headwind (i.e., wind normal to the plane of the upwash), while the crosswind (i.e., wind parallel to the plane of the upwash) has a much less effect.

MECHANICAL SHIELDS

Tests were conducted to evaluate the effect of shielding panels designed to deflect the upwash of hot gases away from the inlets. Shields of various lengths and widths, simulating foldout panels at the nozzle exit plane and at the nozzle inlet plane, were investigated. Table 1 gives a list of test conditions. Tests were first conducted to evaluate the effect of shield design variables (Table 1A), followed by tests to evaluate the effect of model operating conditions (Table 1B).

Ingestion Characteristics

Effect of Shield Size and Location - Figure 29 shows the effect of shield length, width, and location on ingestion. Shield lengths ranging from approximately 1/3 the distance between nozzle centerlines to approximately the distance between nozzle centerlines, and shield widths of 1/4 of the pod width up to the pod width, were investigated. Also shown are the ingestion levels of the reference model without shields.

All shields tested at the nozzle exit plane (Figure 29a) were found to be effective in deflecting the upwash away from the inlets, thus reducing ingestion to low levels typical of operation with a single jet, in which there is no upwash flow. The smallest of these shields is shown in Figure 30.

On the contrary, all shields tested at the inlet plane were found to be ineffective in reducing ingestion (Figure 29b); in fact, all but the largest configurations resulted in an increase in ingestion. In contrast to the totally effective nozzle exit plane shield shown in Figure 30, is the totally ineffective inlet plane shield (largest tested) shown in Figure 31.

Effect of H/D - Figure 32 shows the effect of H/D on shield effectiveness for a shield (L = 12.15", W = 2.5") located at the nozzle exit plane (Figure 33). The shield is seen to be most effective in reducing ingestion at the lower values of H/D where the upwash flow is most coherent, and thus, more effectively deflected by the shield. Also, at the lower values of H/D, the increased strength of the deflected upwash results in stronger entrainment of free air than at higher values of H/D, the importance of the entrainment mechanism as related to shield effectiveness to be discussed later.

Based on extrapolation of the data of Figure 32, the shield would become ineffective at $H/D \approx 10$. At this value of H/D, however, ingestion levels without the shield are low enough that deterioration of shield effectiveness is of little consequence.

Effect of Wind - Figure 34 shows the effect of wind on shield effectiveness. For a 10 mph headwind, (Figure 34a) the shield is seen to result in significant reduction in ingestion levels, while at 20 and 30 mph the headwind in itself is seen to suppress ingestion in the reference configuration such that no shield is required at winds greater than about 20 mph.

In reviewing the raw data in detail, it may be seen that the ingestion prone inlet for the shield configuration with a 10 mph headwind is the forward inlet rather than the aft inlet as for the case of no shield; forward inlet ingestion was found to be the same for the reference model and for the shield configuration, but aft inlet ingestion was found to be greatly reduced with the shield. Thus, the shield is effective in deflecting the upwash away from the aft inlet with the 10 mph headwind, but has no effect on the forward inlet where ingestion results primarily from the far field flow being swept back across the model as discussed previously for the reference model.

For crosswinds in the range from 10-30 mph, the shield is seen to have virtually no effect on temperature level ($\Delta\hat{\overline{T}}$), but is seen to result in significant reductions in temperature distortion ($\hat{\epsilon}$), and in temperature rate of rise ($|\hat{\dot{\overline{T}}}|$), the reduction in distortion diminishing with wind speed and the reduction in rate of rise becoming more pronounced with wind speed.

The reduction in distortion and rate of rise with the shield is the result of a more well mixed flow being blown across the model than for the reference configuration, due to the local outward deflection of the upwash in the proximity of the shield. The reduced level of distortion and rate of rise, as reflected in the character of the instantaneous spatial average temperature, $\overline{T}$, is shown in Figure 35 which compares $\overline{T}$ for the reference configuration and with the shield at a crosswind of 20 mph. With the shield, $\overline{T}$ is seen to be considerably "smoother" than without the shield, although the time average of $\overline{T}$ with respect to the pre-run ambient temperature level (i.e., $\Delta\hat{\overline{T}}$) is about the same for both configurations (Figure 34b).

Flow Field

Additional insight into the factors affecting shield effectiveness in reducing ingestion was gained through flow field studies performed as indicated in the "PROCEDURE." Although much of the detail of these investigations (documented in notes and sketches) is beyond the scope of this report, some significant results are presented in the following paragraphs.

Exit Plane Shields - Figure 36 shows a typical schematic representation of the near flow field for an exit plane shield at low wind conditions. Although Figure 36 is for a shield with L = 12.15" and W = 2.5" (corresponding to Figure 33), the flow field structure shown is generally representative of exit plane shields of other sizes, except where noted differently.

As noted above, very small exit plane shields were found to be effective in deflecting the upwash flow away from the inlets. In addition to the shields deflecting the upwash, entrainment of free air into the highly turbulent deflected upwash was found to be an important factor. This is illustrated in Figure 36 which shows entrainment of free air into the highly turbulent boundary of the deflected upwash, as well as into the free jets. As a result, the flow along the sides of the pod is downward, thus forming a stagnation line on the pod, and associated dividing streamsurface in the field, which prohibits exhaust flows from the near flow field from entering the inlets.

Exit plane shields may be considerably less than the distance between the nozzle centerlines and still effectively deflect the upwash. For the shield of Figure 36, the flow around the ends of the shield is downward and into the exhaust jets. For shorter shields (e.g., Figure 30), although the flow at the ends of the shield is upward, the upward component of momentum is insufficient to overcome the strong sink effect of the free jet. The direction of the flow is thus reversed before reaching the influence of the inlets, eventually being entrained into the free jets.

It is also noted that for shields longer than that of Figure 36, the ends of the shield serve to shield the favorable entrainment characteristics of the free jet and thus should generally be avoided. That is, the free jets provide a powerful sink effect, inducing downflow along the sides of the pod except in the region midway between the

jets where a strong upwash exists. Thus, any shielding of the jet sink effect, which inherently is an ingestion suppression effect, should be avoided.

The width of the shield was found to govern the angle at which the upwash is deflected outward, wider shields deflecting the upwash at lower angles relative to the ground plane. Within limits, the angle at which the upwash is deflected is not important. What is important is that the deflected upwash induces a downflow of free air which results in the formation of a stagnation line and associated dividing streamsurface as discussed above. The minimum width shield investigated (i.e., W = 1.25") was sufficiently wide to provide the desired flow field structure, although the angle of the deflected upwash was found to approach the angle of the dividing streamsurface. Further reduction in width of the shield would probably have resulted in collapse of the dividing streamsurface due to limited area of flow circulation between the streamsurface and the deflected upwash boundary. It is thus speculated that shields down to a critical width would be totally effective in reducing near field ingestion, while shields less than the critical width would be totally ineffective in reducing near field ingestion.

Inlet Plane Shields - As indicated previously, inlet plane shields were found to be ineffective in deflecting the upwash flow away from the inlets. This is illustrated in Figure 37 which shows a schematic representation of the near flow field with an inlet plane shield of the same size as the exit plane shield of Figure 36 (i.e., L = 12.15", W = 2.5").

The flow field with the inlet plane shield is very much similar to that with no shields at all. That is, the low velocity upwash along the sides of the pods, having been reduced in strength by impingement on the pod undersurface, is not of high enough velocity, and not coherent enough, to be effectively vectored outward by the shield. Further, due to the low velocity of the upwash at the plane of the inlet, entrainment of free air by the upwash, even if it were deflected, would be reduced considerably from that of the exit plane shield. Thus, formation of a definite dividing streamsurface which provides a separating barrier between the inlet flow and the upwash flow would be prohibited. The result is that the upwash simply flows around the inlet shield and into the inlets, predominately being ingested in one inlet or the other as discussed previously for the reference configuration without shields.

Although Figure 37 is for a relatively small inlet plane shield, the above comments are representative of larger shields up to and including the largest shield tested (Figure 31).

Pod Pressure Distribution - All shields tested had negligible effect on the pod undersurface pressure distributions. That is, pod pressure distributions with the shields were found to be virtually the same as for the reference model data of Figures 25 through 28.

AIR CURTAIN

Tests were conducted to evaluate the effectiveness of an air curtain concept as a means of suppressing ingestion. This concept involves blowing a sheath of air from the sides of the vehicle which blocks, deflects, and entrains the upwash of hot gases away from the inlets as indicated schematically in Figure 38. In an application of the concept, engine compressor bleed could serve as a convenient source of air for the air curtain.

Table 2 gives a list of air curtain test conditions. The air curtain configurations were supplied by air from plenum chambers located on each side of the model. The air curtain configurations were formed by slotted plates which were attached to the sides of the model, the plates forming the outer wall of the plenum chambers and the slot forming the flow channel for the air curtain. Configuration variation was achieved by interchange of the slotted plates, each pair having a different slot geometry in terms of the slot width, slot length, slot location, and slot angle.

Air curtain flowrate/nozzle flowrate, ϕ, for a given geometric configuration was controlled by varying the plenum pressure level. The range of supply pressure, P/P_∞, was typically P/P_∞ = 2 to 5. This pressure range is commensurate with realistic air curtain supply pressures with engine compressor bleed as a supply source, the lower end of the range corresponding to a high loss internal ducting system from the engine to the air curtain plenum, and the higher end of the range corresponding to a low loss internal ducting system.

Ingestion Characteristics

Effect of Design Variables - Figure 39 shows the effect of geometric variables and flow rate on air curtain effectiveness. The geometric variables include slot width, d, slot length, L, slot location, h, and slot angle, α ($\alpha = 0$ corresponds to horizontal with positive α corresponding to air curtain flow directed downward). In general, the air curtain concept was found to be effective in producing major reductions in ingestion using supply flow rates well below typical limits of engine compressor bleed.

Figure 39a shows that air curtain effectiveness is optimized (in terms of maximum benefit relative to a given value of ϕ) by decreasing the slot width and increasing the supply pressure. That is, for a given value of ϕ, the air curtain momentum, which is a measure of the air curtain "rigidity" in blocking the upwash and penetration depth, is maximized by reducing the slot width and increasing the air curtain supply pressure. Thus, in application of the air curtain concept utilizing engine compressor bleed as an air supply source , a low loss internal ducting system between the compressor bleed port and air curtain supply plenum in combination with "small" slot widths (to limit ϕ) is desirable.

Figure 39b shows that air curtain effectiveness is also improved, for a given value of ϕ, by reducing the slot length down to about one-half, or less, the distance between the exhaust jet centerlines. The shortest length tested (which was about 30% of the distance between exhaust jet centerlines) however, was apparently not long enough in that even at the higher supply pressures, significant ingestion is seen to occur.

Figure 39c shows additional data on the effect of slot dimensions. Major reductions in ingestion (i.e., residual ingestion of the same order as for single jet operation in which there is no upwash) are observed for values of $\phi \approx .02$.

The effect of slot location is shown in Figure 39d. For the slot length and locations tested, there was little effect of slot location. However, the slot length and locations tested were selected (based on a preliminary investigation of the air curtain concept) to be outside the influence of the inlets. A longer slot, closer to the plane of the inlets, can result in the air curtain being pulled into the inlets locally at the ends, with the local breakdown of the air curtain causing collapse of the air curtain to areas otherwise outside the influence of the inlets due to self-coherence tendencies of the air curtain. It should be noted that the strong interaction of the air curtain with the inlet, when placed close to the inlet, precludes the application of the air curtain in the form of a peripheral ring, integral with the engine, around the inlet.

Figure 39e shows the effect of slot angle. Directing the air curtain downward is seen to improve its effectiveness, the downward component of momentum counteracting more directly the upflow of exhaust gases. Angles in excess of about 30°, however, should be avoided in that the air curtain intersects the ground jet relatively

close to the model thus forming a volume which is essentially closed to free air except at the ends. The result is that the air curtain and ground jet have limited access from which to draw free air to satisfy their scavenging characteristics. Thus, the volume between the air curtain and the ground jet drops to subambient pressure, thus causing collapse of the air curtain into the ground jet, or attachment of the air curtain to the side of the pod due to the coanda effect (which is really no more than an entrainment effect).

Although the data of Figure 39 (and subsequent figures) are for an air curtain supply at ambient temperature, tests were conducted at supply temperatures comparable to engine compressor bleed temperatures (e.g., 300°F). The tests at elevated supply temperatures were found to produce results similar to the ambient temperature results within the limits of repeatability. This can be appreciated in considering that the air curtain temperature drops to near ambient levels within a few inches from the sides of the pod due to rapid mixing and entrainment of free air into the air curtain and that any air curtain flow ingested by the inlet has traversed a relatively long path before entering the inlet due to the high outward momentum of the air curtain flow at the source.

Effect of H/D - Figure 40 shows the effect of H/D on air curtain effectiveness for a configuration operating at $\phi = .036$. The results are quite similar to those of Figure 32 which show the effect of H/D with an exit plane mechanical shield of the same length as the air curtain of Figure 40. Specifically, as for the mechanical shield configuration, the air curtain is seen to be most effective in reducing ingestion at the lower values of H/D where the upwash flow is most coherent, and thus, more effectively deflected and entrained by the air curtain. Also, as for the mechanical shield configuration, the air curtain would appear to become ineffective at $H/D \approx 10$. At this value of H/D, however, ingestion levels without the air curtain are low enough that deterioration of air curtain effectiveness is of little consequence.

Effect of Wind - Figure 41 shows the effect of wind on air curtain effectiveness. Again, the results are quite similar to Figure 34 which shows the effect of wind with an exit plane mechanical shield of the same length as the air curtain.

For a 10 mph headwind (Figure 41a), the air curtain is seen to result in significant reduction in ingestion levels, while at 20 and 30 mph the headwind in itself is seen to suppress ingestion in the reference configuration such that no shield is required at winds greater than about 20 mph.

In reviewing the raw data in detail, it may be seen that the ingestion prone inlet for the air curtain configuration with a 10 mph headwind is the forward inlet rather than the aft inlet as for the case of no air curtain; forward inlet ingestion was found to be the same for the reference configuration and for the air curtain configuration, but aft inlet ingestion was found to be greatly reduced with the air curtain. Thus, the air curtain is effective in deflecting the upwash away from the aft inlet with the 10 mph headwind, but has no effect on the forward inlet where ingestion results primarily from the far field flow being swept back across the model as discussed previously for the reference model.

For crosswinds in the range from 10-30 mph, the air curtain is seen to have virtually no effect on temperature level ($\Delta\hat{\bar{T}}$), but is seen to result in significant reductions in temperature distortion ($\hat{\epsilon}$), and in temperature rate of rise ($|\hat{\dot{\bar{T}}}|$), the reduction in distortion diminishing with wind speed and the reduction in rate of rise becoming more pronounced with wind speed.

The reduction in distortion and rate of rise with the air curtain is the result of a more well mixed flow being blown across the model than for the reference configuration due to the local outward deflection of the upwash in the proximity of the air curtain. The reduced level of distortion and rate of rise, as reflected in the character of the instantaneous spatial average temperature, $\bar{T}$, is shown in Figure 42 which compares $\bar{T}$ for the reference configuration and with the air curtain at a cross wind of 20 mph. With the air curtain, $\bar{T}$ is seen to be considerably "smoother" than without the air curtain, although the time average of $\bar{T}$ with respect to the pre-run ambient temperature level (i.e., $\Delta\hat{\bar{T}}$) is about the same for both configurations (Figure 41b).

Flow Field

Flow field studies, similar in nature to those discussed previously for the mechanical shield configurations, were performed for the air curtain configurations. Figure 43 shows a schematic representation of the near flow field for the air curtain

configuration of Figures 40 and 41 at low wind conditions. The flow structure shown, however, is generally typical of other air curtain configurations evaluated.

As noted previously, the majority of the air curtain configurations was effective in deflecting the upwash flow away from the inlets. In addition to the air curtain blocking and deflecting the upwash,entrainment of the upwash and entrainment of free air into the air curtain was found to be a very important factor. The amount of air entrained by the air curtain can be appreciated by noting that at a distance of one pod width (i.e., 5 inches for the model tested) away from the sides of the pod, the mass flow within the air curtain configuration shown, based on the air curtain supply flow of $\phi = .036$ of Figures 40 and 41, is about 50% of the exhaust flow, based on well defined information on the entrainment characteristics of 2-D jets (e.g., Reference 13). Further, from conservation of momentum considerations, the average velocity of the air curtain at a distance of one pod width from the source (including the entrained mass of air as defined above) is still in excess of 100 ft/sec.

As a result of the strong entrainment characteristics of the air curtain, the flow of free air around the air curtain (i.e., above, below, and at the ends) is in the direction of the air curtain as indicated in Figure 43. Further, entrainment of free air by the exhaust jets outside the region of influence of the air curtain results in a down flow of air along the sides of the pod in the proximity of the jets. As a result of the sink effects of the air curtain, the exhaust jets, and the inlets, a "triple point" stagnation point is formed as shown in Figure 43. This point was defined by introducing a low velocity smoke stream into the flow in the proximity of the "triple point" and observing whether the smoke was entrained by the air curtain, the exhaust jet, or the inlet. In the proximity of the triple point, small movements of the smoke stream resulted in switching of the smoke flow toward the predominant sink.

Entrainment of free air by the air curtain also results in formation of a dividing streamsurface of flow over the top of the model as indicated in Figure 43. The dividing streamsurface terminates on the top and sides of the pod in the form of the stagnation lines shown.

As would be expected, there was no influence of the air curtain on the pod pressure distributions. That is, pod pressure distribution with the air curtains was the same (within the limits of repeatability) as for the reference model data of Figures 25 through 28.

CANTED NOZZLES

Tests were conducted to evaluate the effect of nozzle canting from the nominally vertical orientation of the reference model. Table 3 gives a list of test conditions and defines the three modes of nozzle canting investigated.

Ingestion Characteristics

Effect of Cant Mode and Angle - Figure 44 shows the effect of nozzle cant angle for the three cant modes indicated in Table 3. Canting the nozzles aft as little as 8° is seen to reduce ingestion to insignificant levels. Canting the nozzles outward (up to 20°), although reducing ingestion to some degree, is not nearly as effective as the aft cant mode. In addition, canting the nozzles outward, in reducing the strength of the upwash flow, was found to cause the ingestion to switch from one inlet to the other due to low velocity random wind (<3 mph), rather than remaining predominately within one inlet throughout the test as discussed earlier for the vertical jet reference model. Rolling the nozzles (up to 20°) was found to aggravate the ingestion problem, particularly in localized regions of the inlet on the side to which the nozzles were rolled.

Effect of H/D and Wind - Figure 45 shows the effect of H/D on ingestion with the nozzles canted aft 8°. The 8° nozzle cant is seen to be effective in reducing ingestion to insignificant levels over the entire range of H/D.

Figure 46 shows the effect of wind on nozzle cant angle effectiveness. For a 10 mph headwind, significant reduction in ingestion results due to nozzle canting, while at 20 and 30 mph the headwind in itself is seen to suppress ingestion in the reference model. As with the shields discussed previously, the ingestion prone inlet with the 10 mph headwind is the forward inlet where ingestion results primarily from the far flow field being swept back across the model.

Nozzle canting is also effective in reducing ingestion with crosswind. The effectiveness in a crosswind is greater than for the shielding devices discussed previously due to total suppression of the upwash which occurs with nozzle canting as opposed to lateral deflection of the upwash which occurs with shielding devices, the latter leaving the upwash susceptable to the influence of crosswind.

Flow Field

Effect of Cant Mode and Angle - Figures 47 and 48 show the effect of nozzle cant mode and angle on the pod undersurface pressure field. Major reductions in the strength of upwash are seen to occur by canting the nozzles aft, with the upwash virtually eliminated for a nozzle cant angle of 8°. In addition, the bias in the upwash flow towards the aft nozzle is seen to increase with nozzle cant angle.

Characteristic of the flow field with the nozzle canted aft is an amplification in the bias in the upwash flow relative to the nozzle cant angle. The amplified bias results from the unbalanced force produced by the entrainment characteristics of the free jets and by the inlets, the unbalanced force progressively increasing as the upwash is deflected from center. Counterbalancing the unbalanced sink effect of the free jets and inlets is the momentum vector of the upwash at the source which acts as a restoring force (note that the restoring force of the "blocked" upwash between the pod undersurface and the plane of the inlets in the reference configuration is insufficient to overcome the unbalanced sink effect of the inlets (Figure 18), thus leading to ingestion assymetry as discussed previously).

Figure 49 shows a schematic representation of the flow field with the nozzles canted aft 8°. The upwash flow is redirected downward by the entrainment forces of the aft jet before reaching the pod undersurface, subsequently flowing outward from the sides of the pod in the structure of a helical vortex[1]. This is reflected in the negative pressure distribution along the undersurface of the pod as indicated in Figure 47a, except for a slight positive pressure in the proximity of the aft inlet. The flow along the sides of the pod is downward, due to entrainment of the ambient environment by the free jets, the redirected upwash, and the ground jets, except for a small region in the proximity of the inlets where the sink effect of the inlet is dominant over the entrainment effects of the exhaust flows. Similar patterns were observed for smaller nozzle cant angles except that the upwash bias was less and

---

[1] Reference 11 provides additional detail of the effect of nozzle cant on flow field structure, including oil streak photographs which clearly show the detail of the helical vortex.

impingement of the upwash on the undersurface of the pod occurred as indicated by the data of Figures 47a and 48.

With the nozzles canted outward (Figures 47b and 48), the flow structure was found to retain its basic symmetry in the region below the pod (Figure 18), but with significant reduction in the strength of the upwash relative to the vertical jet reference configuration. Rolling the nozzles (Figures 47c and 48) was found to have little effect on the strength of the upwash impinging on the pod undersurface, but resulted in a significant bias in the upwash along the sides of the pod on the side to which the nozzles were rolled.

Effect of H/D and Wind - Figures 50 through 53 show the effect of H/D and wind on the pod undersurface pressure field for nozzles canted aft 8°. The upwash flow is seen to be totally suppressed at all conditions except for at H/D = 2 where minor impingement occurs. Even at H/D = 2, however, ingestion is insignificant in that although the upwash reaches the undersurface of the pod, it is entrained by the exhaust flow field (free jets and ground jet) prior to reaching the region of influence of the inlets.

SUPPRESSION NOZZLES

Tests were conducted with suppression nozzles designed to promote rapid mixing of the exhaust gases with the external environment. Table 4 gives a list of suppression nozzle test conditions, with details of the suppression nozzle configuration shown in Figure 54. The suppression nozzle geometry selected was virtually identical to one of the configurations of Reference 12 (viz. configuration 2.4) in which extensive tests were performed to determine the thrust, discharge, and exhaust pressure/temperature decay characteristics of several suppression nozzle configurations.

As shown in Figure 54, the exit area of the nozzles consists of four rectangular slots, with the distance between the slots equal to the slot width, and with the slot length aligned across the pod. The combined exit area of the four slots is equal to the exit area of the basic circular exhaust nozzle of Figure 10.

Desirable characteristics of suppression nozzles are that noise levels are reduced relative to levels for a conventional circular nozzle of the same exit area and mixing of the exhaust jet with the external environment is enhanced, thereby resulting in a more rapid decay of exhaust jet dynamic pressure and temperature. These effects are generally favorable with respect to noise problems and other adverse ground proximity effects associated with VTOL aircraft.

The primary undesirable characteristic of suppression nozzles is relatively low thrust coefficients compared to conventional circular nozzles, the lower thrust coefficients being attributed to the contribution of the highly aspirated-low pressure base area between the slots, rather than due to deterioration of internal nozzle performance. Based on the data of Reference 12, the thrust coefficient (i.e., measured thrust/ideal thrust based on measured flow rate) of the nozzle of Figure 54 is about .95.

Prior to conducting ingestion tests, calibration of the exhaust jets with the suppression nozzles were performed. These calibrations, which were performed in the manner described previously in the "PROCEDURE" for the basic circular nozzles, included measurement of the exhaust jet dynamic pressure profiles and determination of exhaust jet alignment.

Figure 55 shows the variation in jet centerline dynamic pressure with Z/D_e (D_e = 2.25" is the diameter of a circular nozzle with the same exit area). For comparative purposes, the dynamic pressure decay with the basic circular nozzles is also shown. The effect of increased mixing of the suppression nozzle exhaust jets with the external environment is reflected in the rapid decay rate of the centerline dynamic pressure relative to that for the basic circular nozzles, with maximum values of dynamic pressure within the exhaust jet reduced to one-half the value of the nozzle exit dynamic pressure within two equivalent diameters of the nozzle exit. Additional exhaust decay characteristics of a geometrically similar suppression nozzle are given in Reference 12.

Ingestion Characteristics

Figure 56 shows the effect of H/D on ingestion for the suppression nozzle and reference nozzle configuration. Other than at very low values of H/D (i.e., H/D $\lesssim 4$), there is no significant reduction in ingestion with the suppression nozzles; in fact, at the higher values of H/D, the suppression nozzles produce a significant increase in the rate of rise parameter $|\hat{\dot{T}}|$.

Figure 57 shows the effect of wind on ingestion for the suppression nozzle configuration at H/D = 4. Significant reduction in ingestion is evident over the range of wind speeds, except for headwind values in excess of 20 mph where the headwind of itself is sufficiently strong to suppress ingestion to insignificant levels with the reference nozzle configuration.

Flow Field

Figures 58 and 59 show the effect of H/D on the pod undersurface pressure field. Although the pressure decay rate of the free jets was found to be considerably greater for the suppression nozzles than for the basic circular nozzles, the upwash strength, as measured by the pod pressure distribution, was found to be comparable. Although this result is somewhat surprising, it is pointed out that the processes of impingement of the free jet on the ground plane, flow of the ground jet to the interaction plane, and interaction of the ground jets to form an upwash, reduce the dynamic

pressure by an order of magnitude (i.e., $\Delta P_{max}/q_n \leq .03$) from the values immediately prior to impingement of the free jet on the ground plane. Thus, the pressure decay trend of the free jets as shown in Figure 55 represents only a small portion of the overall factor by which the jet flows decay in traversing from the nozzle exit to the pod undersurface.

GROUND PLANE PLATFORMS

Tests were conducted with ground plane platforms designed to suppress the upwash of exhaust gases by diffusing the impinging exhaust jets and laterally deflecting the gases away from the model. This approach to suppression of hot gas ingestion would apply primarily to permanent landing sites.

Table 5 gives a list of ground plane platform test conditions, with Figures 60 and 61 showing details of a ground plane platform consisting of a grated surface mounted on a louvered support frame. Figure 62 shows additional detail of the louvered support frame. In addition to grate and louver combinations, tests were performed as indicated in Table 5, with grate alone in which the effects of grate porosity (percent open area). σ, and platform height above the ground plane, H_o/D were investigated.

Wind directions, with respect to model and louver orientations, identified in Table 5 are defined in Figure 63.

Ingestion Characteristics

Effect of σ and H_o/D - Figure 64 shows the effect of grate porosity, σ, and platform height, H_o/D, on ingestion at low wind conditions for platform configurations consisting of grates only (i.e., no louvers beneath the grates). Note that the 100% porosity data correspond to the reference model without a platform at a height equal to $H/D + H_o/D$.

The data show some rather surprising, but consistent, trends with respect to the effects of grate porosity, σ. First of all, ingestion is seen to decrease with increasing σ from the reference condition of $\sigma = 0$ up to $\sigma \approx 40\%$. In the range from $\sigma \approx 40\%$ to $\sigma = 50\text{-}60\%$, there is a rapid and very substantial increase in ingestion at the lower values of H_o/D, resulting in peak values of ingestion which are several times more severe, in terms of $\Delta\hat{\bar{T}}$ and $\hat{\epsilon}$, than for the reference model, and about twice as severe in terms of $\left|\hat{\bar{T}}\right|$. In the range from $\sigma = 50\text{-}60\%$ to $\sigma \approx 80\%$, ingestion decreases rapidly, with no apparent effect of the grate for $\sigma \geq 80\%$. Further, unlike the reference model or other configurations employing ineffective ingestion suppression devices, the ingestion for the configurations of Figure 64 was found to

be equally distributed between the two inlets rather than unsymmetrically distributed as discussed for the reference model.

Although the data of Figure 64 are not completely understood, it is speculated that near field buoyancy effects (i.e., the rise of hot gases due to reduced density as opposed to the strong dynamic upwash flow due to the interaction of opposing ground jet flows) are largely responsible for the high levels of ingestion experienced in the range from $\sigma \approx 40\%$ to $\sigma \approx 70\%$. This is based on several observations. First of all, the strength of the upwash is greatly suppressed for all values of grate porosity in this range as measured by the pressure distribution on the undersurface of the pod (to be discussed in more detail later). Further, manual surveys of the flow field at reduced exhaust temperatures indicated very little upwash, while manual surveys of the flow field at ambient exhaust temperature showed a definite downflow of air along the sides of the model, and through the grate, the downflow being induced by the entrainment field of the free jets and ground jet flow beneath the grate. Thus, it is speculated that the severe inlet temperature environment experienced at full exhaust temperature is due primarily to hot gases which rise due to buoyancy forces rather than due to an upflow of gases resulting dynamic interactions of high velocity ground jets. This idea is further supported by the fact that the ingestion was found to be equally distributed between the inlets as would be expected for a buoyancy model upwash comprised of a large volume of low velocity upwash flow, this model differing from the coherent fountain of upwash gases resulting from ground jet dynamic interactions, which leads to upwash instability and unsymmetrical ingestion as discussed previously.

Figures 65 and 66 show the effect of σ and H_o/D on ingestion at low wind conditions for grate plus louver combinations where the louvers are oriented to vector the exhaust flow aft and vector the exhaust flow left. Note that the 100% porosity data of Figure 65 corresponds to configurations with louvers only (i.e., no grate).

In strong contrast to Figure 64, Figure 65 shows that all values of grate porosity investigated were found to be effective in reducing ingestion to insignificant levels when used in combination with louvers, including the grates which produced the most severe ingestion when tested without louvers. Additionally, all platform heights investigated were found to be effective in reducing ingestion to insignificant levels, although the lowest platform height ($H_o/D = 2$) was probably marginal based

on evaluations of the near flow field which showed the platform was restricting the natural growth of the ground jet beneath the platform, thus producing excessive regions of upflow through grate near the edges of the platform.

Effect of H/D and Wind - Figure 67 shows the effect of H/D on ingestion for grate plus louver combinations for fixed values of platform height and porosity. The platform is seen to be most effective at the lower values of H/D.

Figure 68 shows the effect of wind on ingestion for grate plus louver combinations. Similar data for the reference model are presented in Figure 23. With headwind, for louvers vectoring the exhaust flow either aft or left, reduction in ingestion was experienced at wind speeds less than about 15 mph. At wind speeds greater than about 15 mph, however, where ingestion is low with the reference model, ingestion was found to be significant with the ground plane platforms. With crosswind, for louvers vectoring the exhaust flow either aft or left, ingestion levels were generally suppressed below levels of the reference model; even so, ingestion was still quite significant at high crosswinds.

Flow Field

Grate Only - Figures 69 and 70 show the effect of σ and H_o/D on the pod undersurface pressure field for platform configurations consisting of a grate without louvers. Major reductions in the strength of the upwash are seen to occur for all values of σ investigated. It is also observed that increasing σ to values greater than $\sigma = 36\%$ tends to result in an increase in the upwash at the lower values of H_o/D.

Figure 71 shows a typical schematic representation of the flow field for a grate without louvers. As mentioned before, surveys of the flow field for configurations without louvers operating at reduced temperatures indicated little upwash flow, while surveys at ambient temperature indicated predominately downflow in the near flow field region. However, due to the severe ingestion experienced with these configurations at full exhaust temperature, and the pressure distributions on the undersurface of the pod as indicated in Figures 69 and 70 (also measured at full exhaust temperature), Figure 71 incorporates near field buoyancy effects which occur at full exhaust temperature superimposed on the flow field measured at reduced exhaust temperature.

The overall result is a flow field in which the upwash due to buoyancy effects prevails and the upwash due to dynamic interaction effects is minimal.

Grate Plus Louvers - Figures 72 and 73 show the effect of σ and H_o/D on the pod undersurface pressure field for grate plus louver combinations. With louvers, the upwash flow is seen to be totally suppressed for all values of σ and H_o/D. Figure 74 shows the details of the near flow field for typical grate plus louver combination.

With the exhaust jets vectored aft (Figure 74a), the potential upwash of exhaust gases is totally suppressed, with the flow of exhaust gases over the grate confined within a thin layer approximately two inches, or less, in depth. This relatively thin layer of exhaust gases results from upflow of exhaust gases through the grate in regions where the flow beneath the platform is opposed to the direction of the louvers, and also in the region between the nozzles where the flow from the forward nozzle is partially blocked by the flow from the aft nozzle beneath the platform. In the remaining region of the grate, the flow through the grate is downward, being induced by the entrainment field of the ground jet beneath the platform. Further, the flow of free air about the sides of, and under, the entire model is downward, the downflow being induced by the entrainment field of the free jets and ground jet flows.

The above described general flow pattern was found to occur at other values of σ and other values of H_o/D, although the flow of exhaust gases over the surface was found to increase with decreasing σ and decreasing H_o/D. At the lowest value of σ investigated (i.e., $\sigma = 36\%$), the upflow of exhaust gases between the nozzles was found to persist to a height just slightly below the pod undersurface before being redirected downward into the free jets and ground jet flow.

The potential upwash of exhaust gases beneath the model was also found to be totally suppressed with the exhaust jets vectored left (Figure 74b). However, with the exhaust jets vectored left, the flow of exhaust gases over the grate was found to be significantly greater than for the exhaust jets vectored aft.

Specifically, with the exhaust jets vectored left, there is a significant upflow of exhaust gases through the grate in the region of the interaction plane on the right side of the model where the flow beneath the platform is opposed to the direction of the louvers. Away from the interaction plane, the upflow of the counterflowing exhaust

gases on the right side of the model is considerably less, being comparable to the upflow of the counterflowing exhaust gases for the configuration in which the exhaust jets are vectored aft.

On the left side of the model, and in the region of the interaction plane, there is also an upflow of exhaust gases through the grate near the edge of the platform where the ground jet has thickened and is thus physically restricted by the platform. This upflow of exhaust gases is directed toward the model due to the louver orientation. Before reaching the model, however, the flow is recirculated downward through the grate, due to the entrainment field of the ground jet beneath the grate where the ground jet is still relatively thin compared to the platform height.

As a result of the above described exhaust flow pattern in the proximity of the platform, the flow of free air about the sides of, and under, the entire model is downward due to the entrainment field of the free jets and ground jet flow. Further, the effects of σ and H_o/D in altering the flow field pattern were similar to those discussed previously for the exhaust jets vectored aft, namely, that decreasing σ and H_o/D was found to increase the quantity of exhaust flow above the grate.

Effect of H/D and Wind - Figures 75 through 77 show the effects of H/D and wind on the pod undersurface pressure field for grate plus louver combinations. The configurations are seen to be totally effective in suppressing upwash at all values of H/D and wind conditions. It is recalled, however, that ingestion was found to be significant at most of the wind conditions tested, thus indicating that significant ingestion results from interaction of the wind with the ground jet flow field.

SUMMARY OF RESULTS

An investigation was performed to determine the relative effectiveness of various exhaust gas ingestion suppression concepts for application to VTOL aircraft. The test model used in the investigation was a small-scale simulated VTOL lift engine pod containing two "engines."

The majority of the ingestion suppression concepts evaluated were found to be effective, in varying degrees, in reducing hot gas ingestion. However, none were found to be totally effective in eliminating hot gas ingestion at all model operating conditions, particularly at crosswind conditions. Some specific results for each of the concepts investigated are given below.

Mechanical Shields

At low wind conditions, relatively small mechanical shields simulating fold out panels located at the nozzle exit plane were effective in deflecting the upwash of exhaust gases away from the inlets, thus resulting in major reductions in hot gas ingestion. Shields located at the inlet plane, even though relatively large in extent, were ineffective in deflecting the upwash and reducing ingestion, and in most cases, resulted in an increase in ingestion.

With H/D, exit plane shields were found to be most effective at lower values of H/D where the upwash is most coherent, and thus, most effectively deflected by a small surface at the nozzle exit plane.

With headwind, exit plane shields were found to result in significant reduction in ingestion. With crosswind, inlet temperature levels were virtually unaffected, but significant reductions in temperature distortion and temperature rate of rise were observed.

Air Curtain

This concept involves blowing a sheath of air from the sides of the vehicle which blocks, deflects, and entrains the upwash of hot gases away from the inlets. In an

application of the concept, engine compressor bleed could serve as a convenient source of air for the air curtain.

Air curtain configurations supplied by as little as 2% of the nozzle flow rate were found to be effective in deflecting the upwash of exhaust gases and producing major reductions in hot gas ingestion at low wind conditions. With H/D, air curtain effectiveness was found to be higher at lower values of H/D where the upwash is most coherent, and thus, most effectively blocked and deflected by a relatively short air curtain.

With headwind, an air curtain configuration supplied with less than 4% of the inlet flow was found to result in significant reduction in ingestion. With crosswind, inlet temperature levels were virtually unaffected, but significant reductions in temperature distortion and temperature rate of rise were observed.

Canted Nozzles

At low wind conditions, canting the nozzles aft as little as 8° eliminated the upwash of exhaust gases and associated hot gas ingestion over the range of H/D. With wind (headwind and crosswind), significant reduction in ingestion was experienced with the nozzles canted aft 8°.

Canting the nozzles outward (up to 20°) was found to result in significant reduction in the strength of the upwash but no significant reduction in ingestion. Rolling the nozzles (up to 20°) was found to have little effect on the strength of the upwash, and found to aggravate the ingestion problem.

Suppression Nozzles

Suppression nozzles, designed to promote rapid mixing of the exhaust gases with the external environment, were investigated. Although effective in reducing hot gas ingestion at low values of H/D (i.e., $H/D \leq 4$), both at low wind and high wind conditions, no significant reduction in ingestion occurred at higher values of H/D.

Ground Plane Platforms

Ground plane platforms were designed to suppress the upwash of exhaust gases by diffusing the impinging exhaust jets and deflecting the gases away from the model. For platforms consisting of only a porous grate, ingestion was found to be several times more severe for many of the grate porosity/platform height combinations investigated than for the reference model, even though the grates produced major reductions in the strength of the upwash. Analysis of the data for these configurations indicate that ingestion is governed primarily by near field buoyancy effects rather than by an upwash resulting from dynamic interaction of the ground jet flows.

In contrast, platforms comprised of a grate plus louver combination were found to be totally effective in suppressing the upwash and reducing ingestion to low levels at low wind conditions. With headwind, grate plus louver combinations resulted in a reduction in ingestion at wind speeds less than about 15 mph while at wind speeds greater than about 15 mph, where ingestion is low with the reference model, ingestion was found to be significant. With crosswind, ingestion levels were generally suppressed below levels of the reference configuration.

REFERENCES

1. Hall, G. R. "Recirculation and Ingestion Characteristics of a Large-Scale VTOL Lift Engine Pod." NASA CR-72410, August 1968.

2. Hall, G. R., "Scaling of VTOL Recirculation Effects." NASA CR-1625, August 1970.

3. Hall, G. R., "Recirculation Characteristics of a Small-Scale VTOL Lift Engine Pod" NASA CR-1774, 1970.

4. Lavi, R., "Parametric Investigations of VTOL Ground Proximity Effects." AIAA Paper Number 67-44, July 1967.

5. McLemore, H. C., Smith, C. C., Jr., "Hot-Gas Ingestion Investigation of Large-Scale Jet VTOL Fighter-Type Models." NASA TN-D-4609, June 1968.

6. Lavi, R., Hall, G.R., Stark, W. W., "Full-Scale Ground Proximity Investigation of a VTOL Fighter Model Aircraft." NASA CR-1098, June 1968.

7. Kirk, J. A., Barrack, J.P., "Reingestion Characteristics and Inlet Flow Distortion of V/STOL Lift Engine Fighter Configurations." AIAA Journal of Aircraft, March-April 1969.

8. McLemore, H. Clyde, Smith, Charles, C., Jr., and Hemeter, Patricia G., "Generalized Hot-Gas Ingestion Investigation of Large-Scale Jet VTOL Fighter-Type Models." NASA TN-D-5581, January 1970.

9. Watson, W. W., Weddell, A., Murakoshi, A., "Real Time, Real Temperature Jet V/STOL Test Facility." AIAA Paper Number 69-310, March 1969.

10. Hall, G. R., Bogdanovic, J. A., "Response of Bare Wire Thermocouples to Temperature Variations in a Jet Engine Intake." AIAA Journal of Aircraft, July-August 1967.

11. Hall, G. R., Rogers, K.H., "Recirculation Effects Produced by a Pair of Heated Jets Impinging on a Ground Plane." NASA CR-1307, May 1969.

12. Higgins, D. C., Kelly, D. P., Wainwright, T. W., "Exhaust Jet Wake and Thrust Characteristics of Several Nozzles Designed for VTOL Downwash Suppression." NASA CR-373, January 1966.

13. Abramovich, G. N., The Theory of Turbulent Jets, Cambridge, Mass., The M.I.T. Press, 1963.

TABLE 1. MECHANICAL SHIELD TEST CONDITIONS

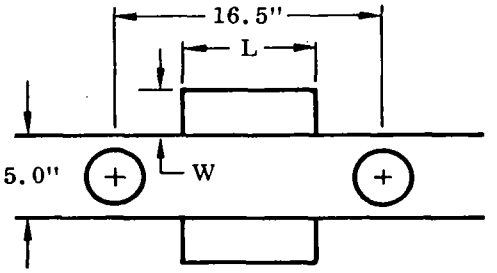

(A) Effect of Design Variables

Model Operating Conditions			Mechanical Shield Design Variables		
H/D	Exhaust Condition	Wind Condition	Location	Width, W	Length, L
4 ↓	Turbojet ↓	<3 MPH ↓	Exit Plane ↓	1.25" ↓	5.0" 8.25" 12.15" 20.85"
			Exit Plane ↓	2.50" ↓	5.0" 8.25" 12.15" 20.85"
			Inlet Plane ↓	2.50" ↓	8.25" 12.15" 20.85"
			Inlet Plane ↓	5.0" ↓	8.25" 12.15" 20.85"

(B) Effect of Model Operating Conditions

Model Operating Conditions			Mechanical Shield Design Variables		
H/D	Exhaust Condition	Wind Condition	Location	Width, W	Length, L
2 4 6 8	Turbojet ↓	<3 MPH ↓	Exit Plane ↓	2.50" ↓	12.15" ↓
2 4 6 8	Turbofan ↓	<3 MPH ↓			
4 ↓	Turbojet ↓	10 MPH Headwind 20 ↓ 30 ↓			
4 ↓	Turbojet ↓	10 MPH Crosswind 20 ↓ 30 ↓			

TABLE 2. AIR CURTAIN TEST CONDITIONS

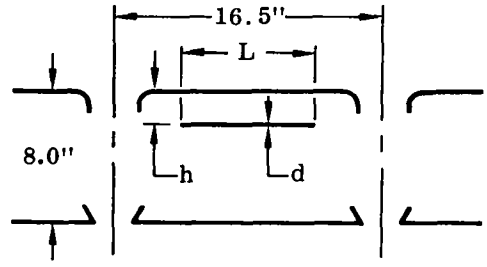

(A) Effect of Design Variables

Model Operating Conditions			Air Curtain Design Variables*			
H/D	Exhaust Condition	Wind Condition	Slot Width, d	Slot Length, L	Slot Location, h	Slot Angle, α
4	Turbojet	<3 MPH	.004"	8.25"	2.4"	15°
			.004" .008" .012"	12.15"	2.4"	15°
			.008"	5.0" 8.25" 20.85"	2.4"	15°
			.008"	12.15"	1.0" 3.8"	15°
			.004"	12.15"	2.4"	0° 30°

*Typical range of air curtain supply pressure for each configuration was P/P_∞ = 2-5.

(B) Effect of Model Operating Conditions

Model Operating Conditions			Air Curtain Design Variables*			
H/D	Exhaust Condition	Wind Condition	Slot Width, d	Slot Length, L	Slot Location, h	Slot Angle, α
2 4 6 8	Turbojet	<3 MPH	.004"	12.15"	2.4"	15°
2 4 6 8	Turbofan	<3 MPH				
4	Turbojet	10 MPH Headwind 20 30				
4	Turbojet	10 MPH Crosswind 20 30				

*Air curtain supply pressure P/P_∞ = 4.

TABLE 3. CANTED NOZZLE TEST CONDITIONS

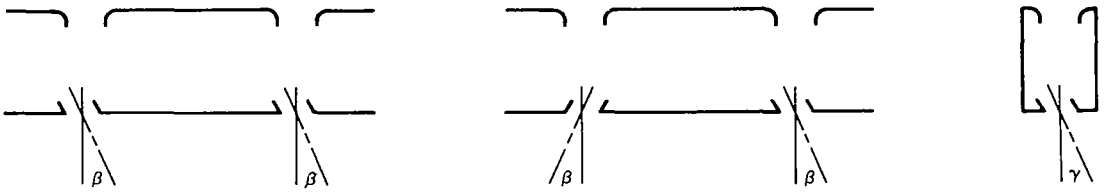

Canted Aft | Canted Outward | Rolled

(A) Effect of Nozzle Cant Variables

Model Operating Conditions			Nozzle Cant Variables	
H/D	Exhaust Conditions	Wind Conditions	Mode	Angle β (γ)
4 ↓	Turbojet ↓	<3 MPH ↓	Canted Aft ↓	2° 4° 6° 8°
			Canted Outward ↓	4° 8° 14° 20°
			Rolled ↓	4° 8° 14° 20°

(B) Effect of Model Operating Conditions

Model Operating Conditions			Nozzle Cant Variables	
H/D	Exhaust Conditions	Wind Conditions	Mode	Angle
2 4 6 8	Turbojet ↓	<3 MPH ↓	Aft ↓	8° ↓
2 4 6 8	Turbofan ↓	<3 MPH ↓		
4 ↓	Turbojet ↓	10 MPH Headwind ↓ 20 30		
4 ↓	Turbojet ↓	10 MPH Crosswind ↓ 20 30		

TABLE 4. SUPPRESSION NOZZLE TEST CONDITIONS

H/D	Exhaust Condition	Wind Condition
2 4 6 8 12	Turbojet ↓	< 3 MPH ↓
4 ↓	Turbojet ↓	10 MPH Headwind 20 ↓ 30
4 ↓	Turbojet ↓	10 MPH Crosswind 20 ↓ 30

TABLE 5. GROUND PLANE PLATFORM TEST CONDITIONS

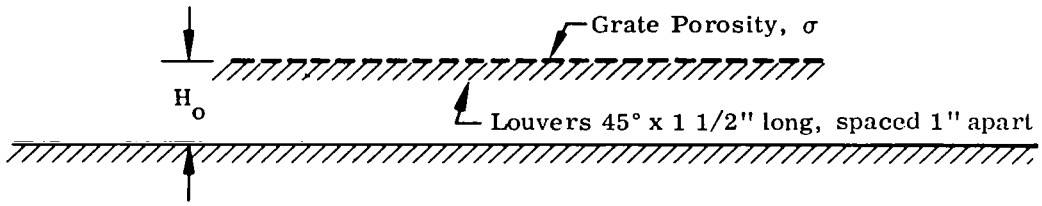

(A) Effect of Design Variables

Model Operating Conditions			Ground Plane Platform Design Variables		
H/D	Exhaust Condition	Wind Condition	Configuration	Grate Porosity, σ	Height Above Ground Plane, H_o/D
4	Turbojet	<3 MPH	Grate Only	36% 51% 67%	2
			Grate Only	23% 36% 51% 58% 67%	3
			Grate Only	36% 51% 67%	4
			Grate Only	36% 51% 67%	8
			Grate Only	36% 51% 67%	16
			Grate Plus Louvers Vectored Aft	36% 51% 67% 100% (i.e., no grate)	3
			Grate Plus Louvers Vectored Left	36% 51% 67% 100% (i.e., no grate)	3
			Grate Plus Louvers Vectored Aft	67%	2 4
			Grate Plus Louvers Vectored Left	67%	2 4

TABLE 5 (cont'd). GROUND PLANE PLATFORM TEST CONDITIONS

(B) Effect of Model Operating Conditions

Model Operating Conditions*			Ground Plane Platform Design Variables		
H/D	Exhaust Conditions	Wind Conditions	Configuration	Grate Porosity, σ	Height Above Ground Plane, H_o/D
2 4 6 8	Turbojet	<3 MPH	Grate Plus Louvers Vectored Aft	51%	3
2 4 6 8	Turbofan	<3 MPH			
4	Turbojet	10 MPH Headwind 20 30			
4	Turbojet	10 MPH Crosswind 20 30			
4	Turbojet	10 MPH Tailwind 20 30			
2 4 6 8	Turbojet	<3 MPH	Grate Plus Louvers Vectored Left	51%	3
2 4 6 8	Turbofan	<3 MPH			
4	Turbojet	10 MPH Crosswind #1 20 30			
4	Turbojet	10 MPH Headwind 20 30			
4	Turbojet	10 MPH Crosswind #2 20 30			

* See Figure 63 for wind orientation definition

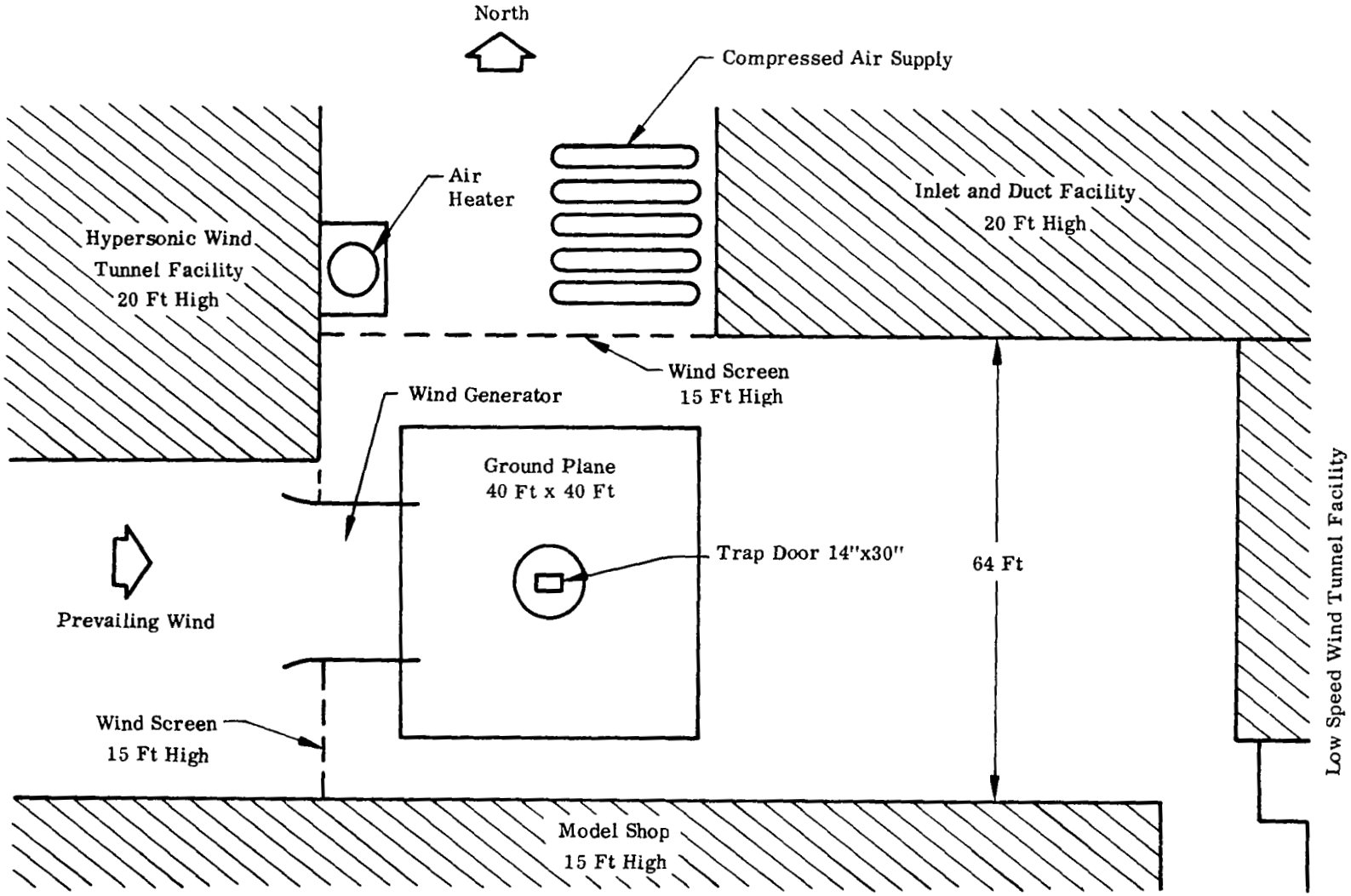

FIGURE 1. NORTHROP V/STOL GROUND EFFECTS TEST FACILITY

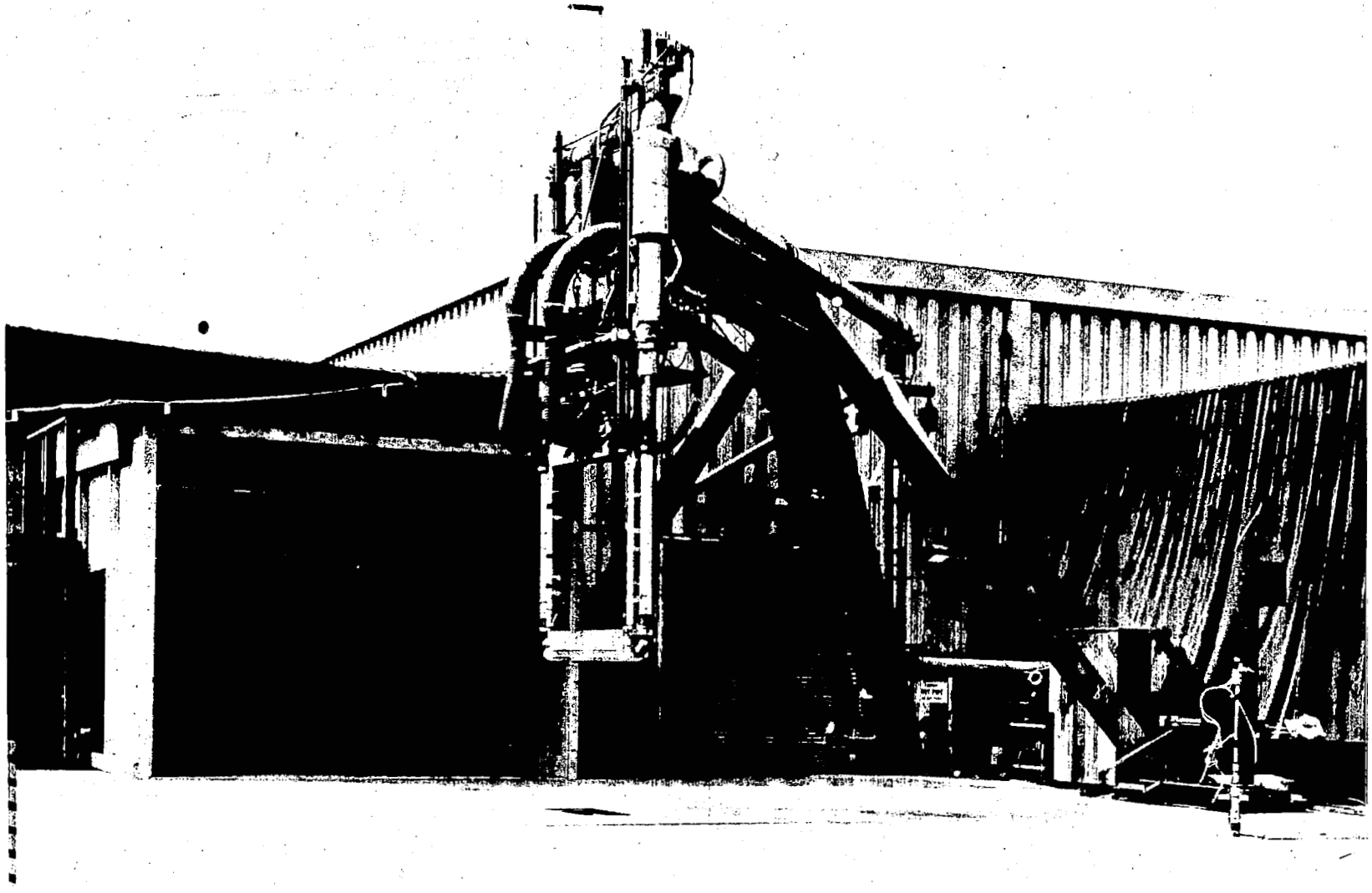

FIGURE 2. NORTHROP V/STOL GROUND EFFECTS TEST FACILITY

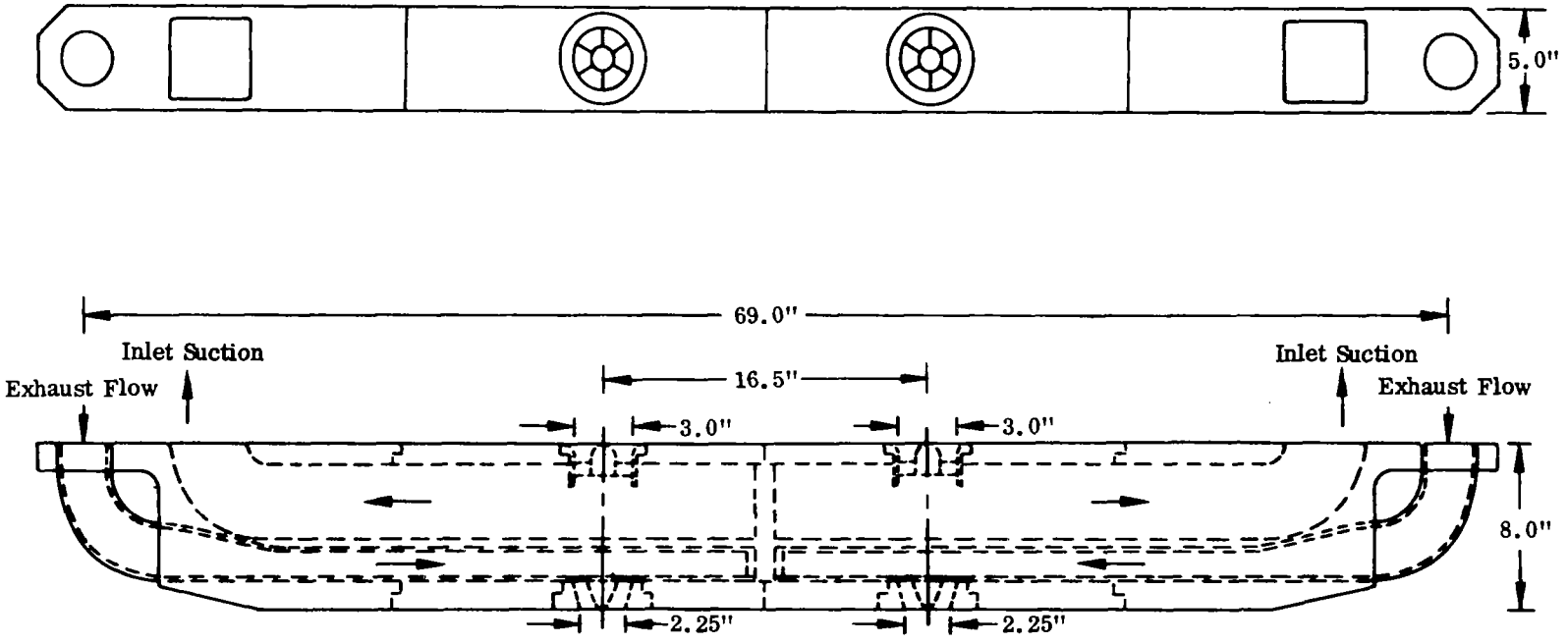

FIGURE 3. ENGINE POD MODEL

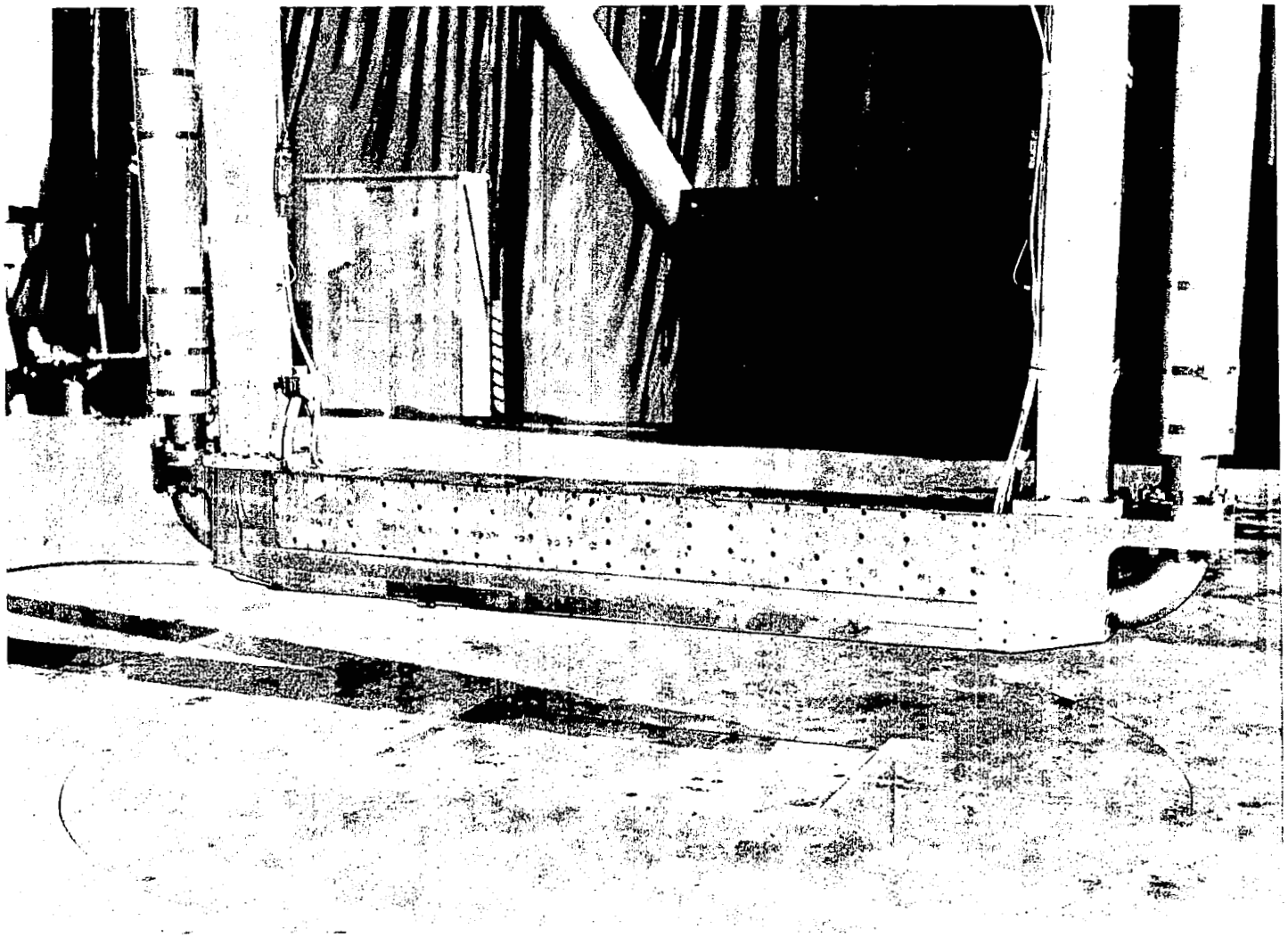

FIGURE 4. ENGINE POD MODEL

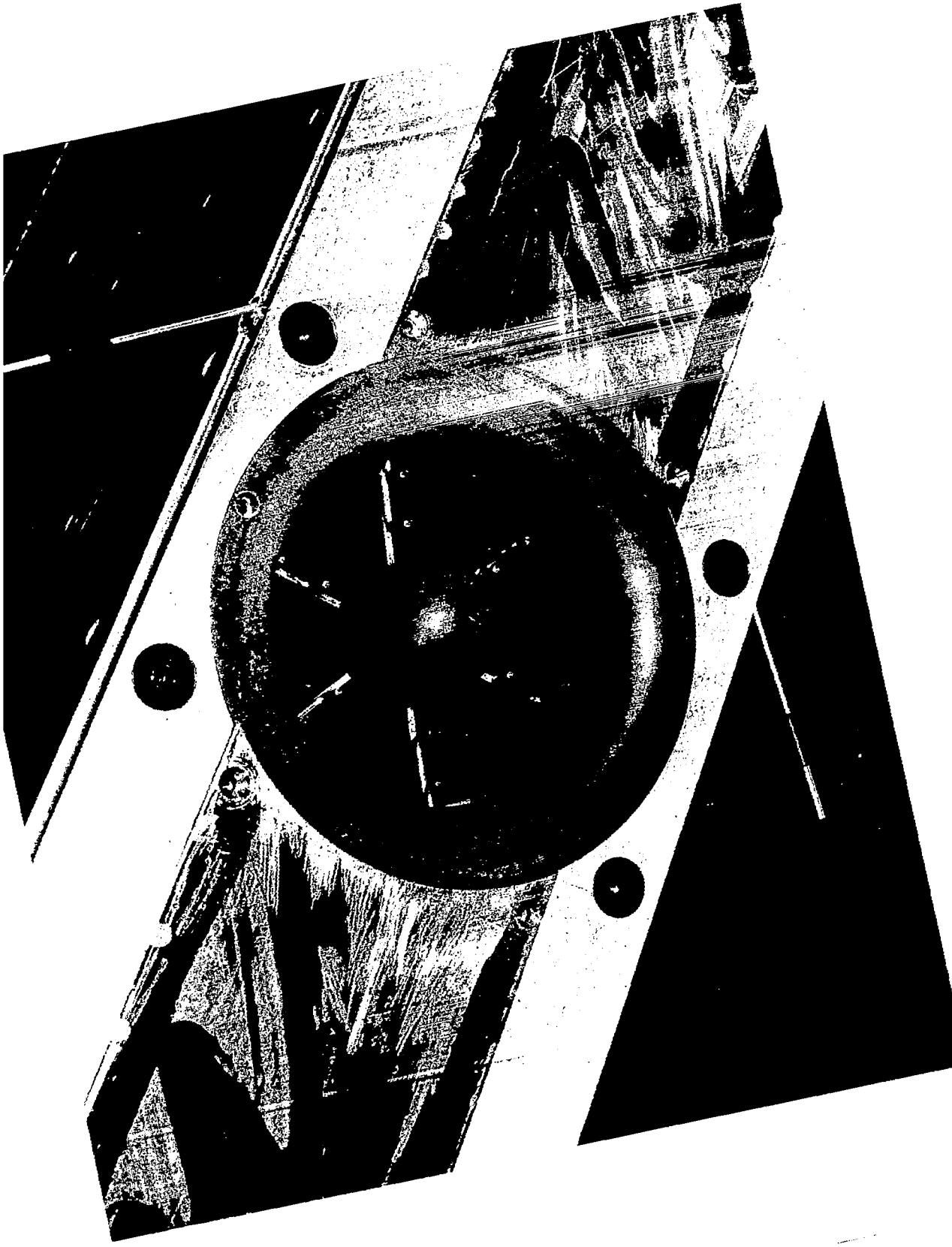

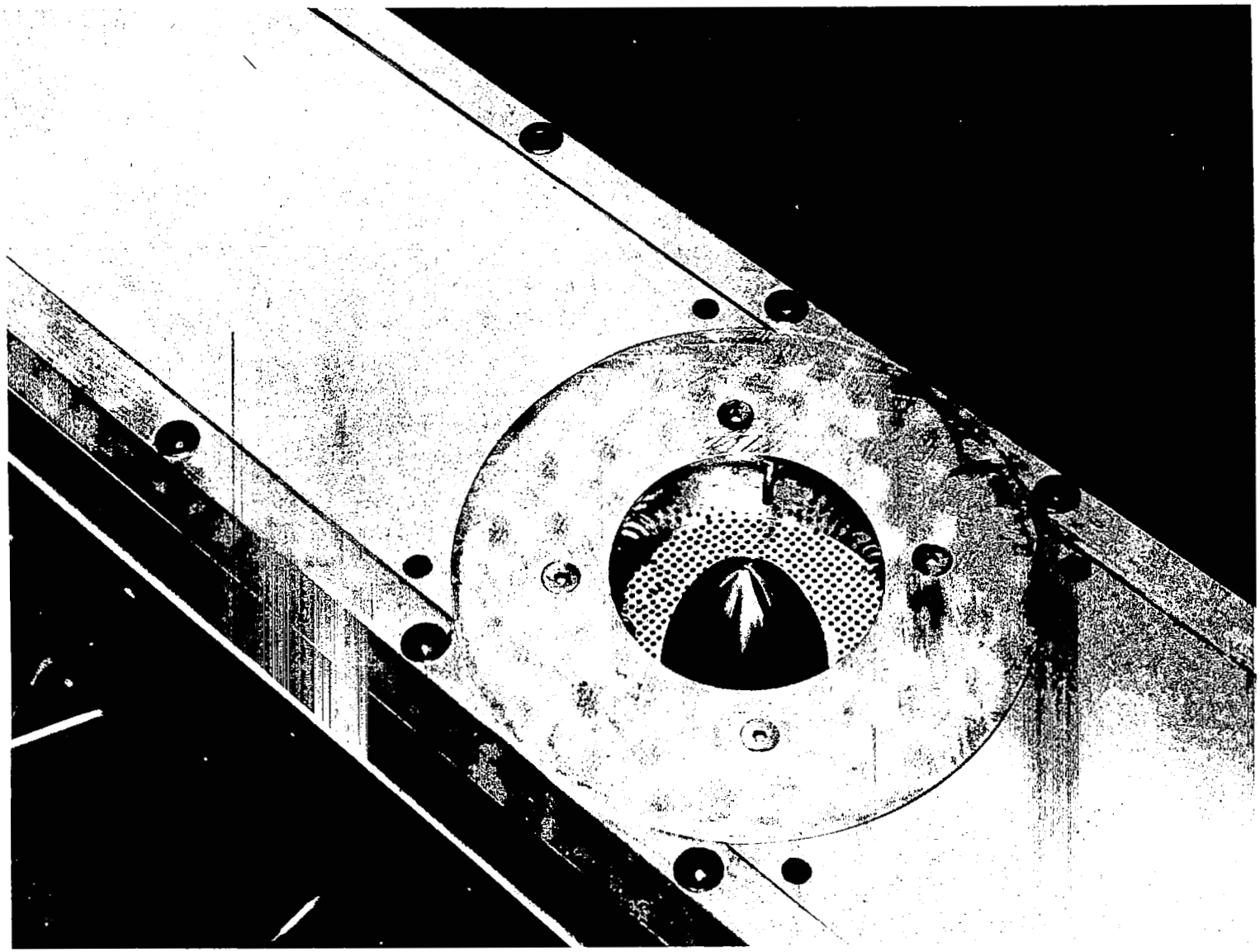

FIGURE 6. BASIC EXHAUST NOZZLE DETAIL

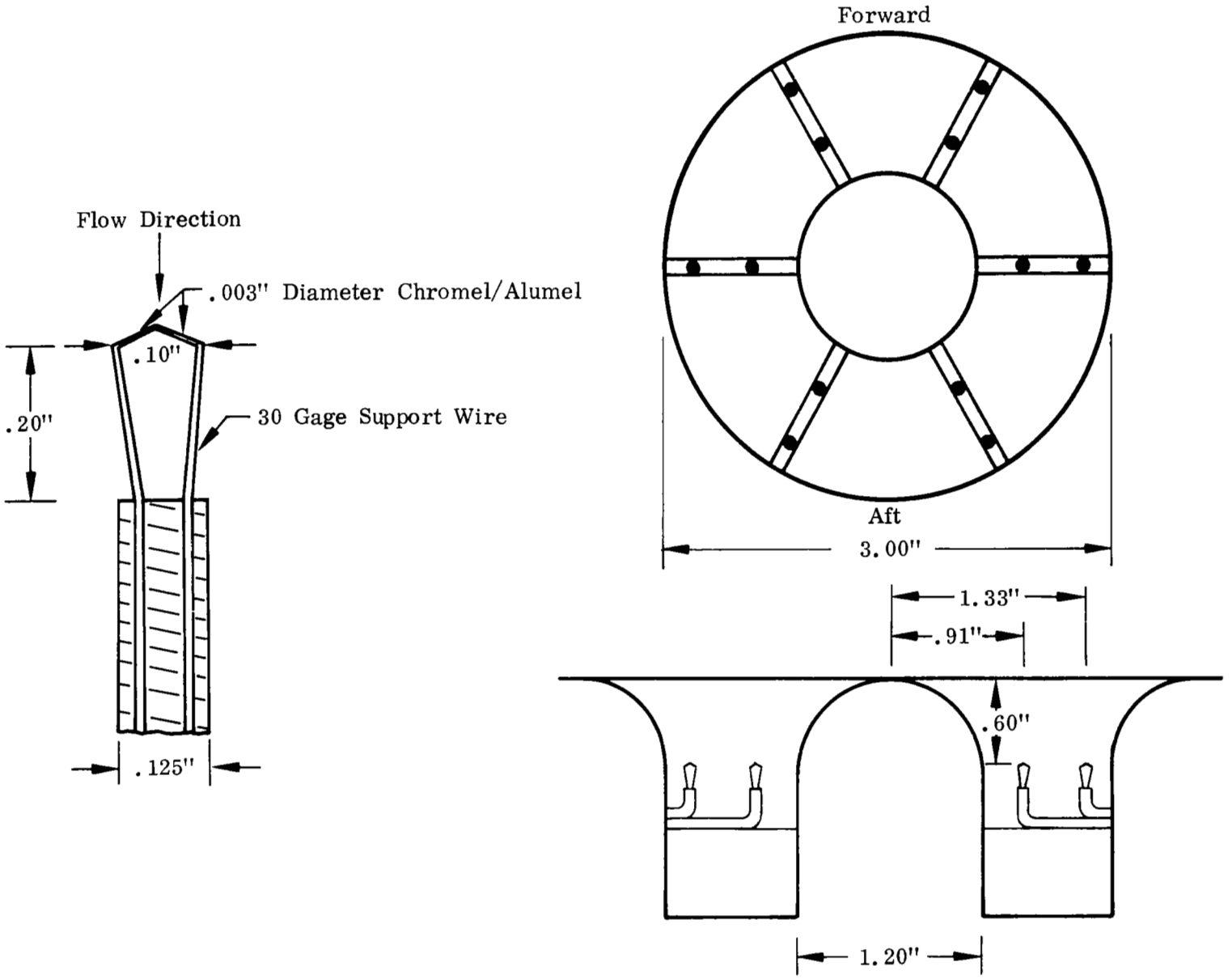

FIGURE 7. INLET THERMOCOUPLE INSTRUMENTATION

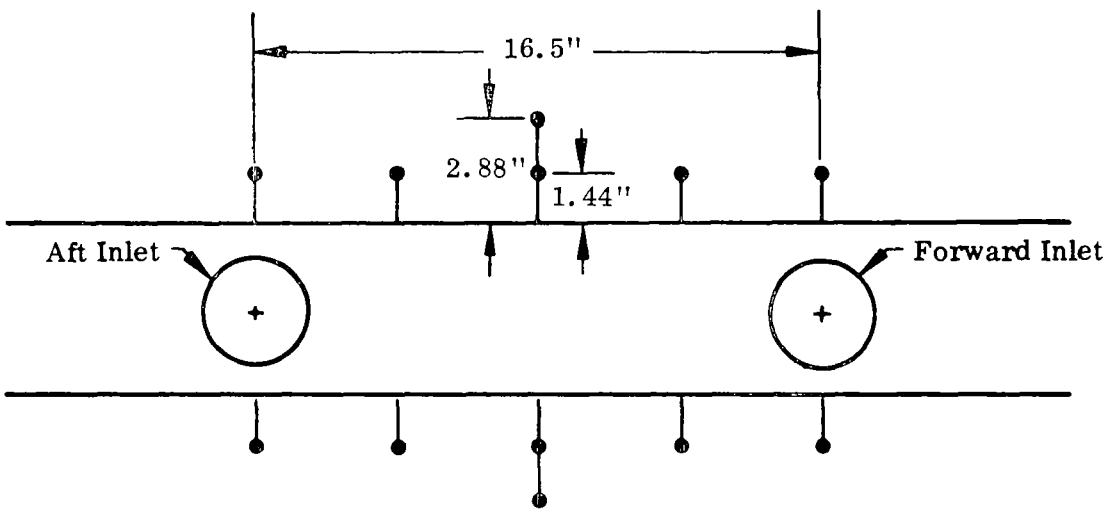

Note: T-C's located in plane of the inlets

FIGURE 8. INLET PROXIMITY THERMOCOUPLES

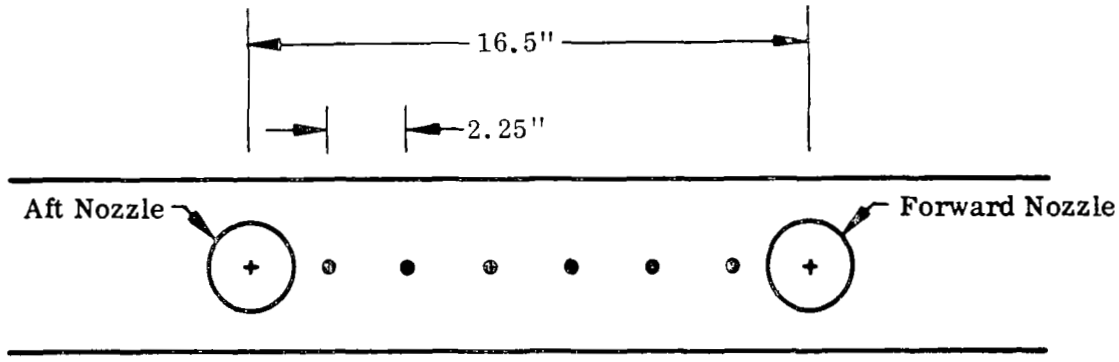

Note: Pressure taps located on pod lower surface

FIGURE 9. POD PRESSURE INSTRUMENTATION

Turbojet ($T_n = 1200^{o}F$, $P_n/P_\infty = 1.9$)

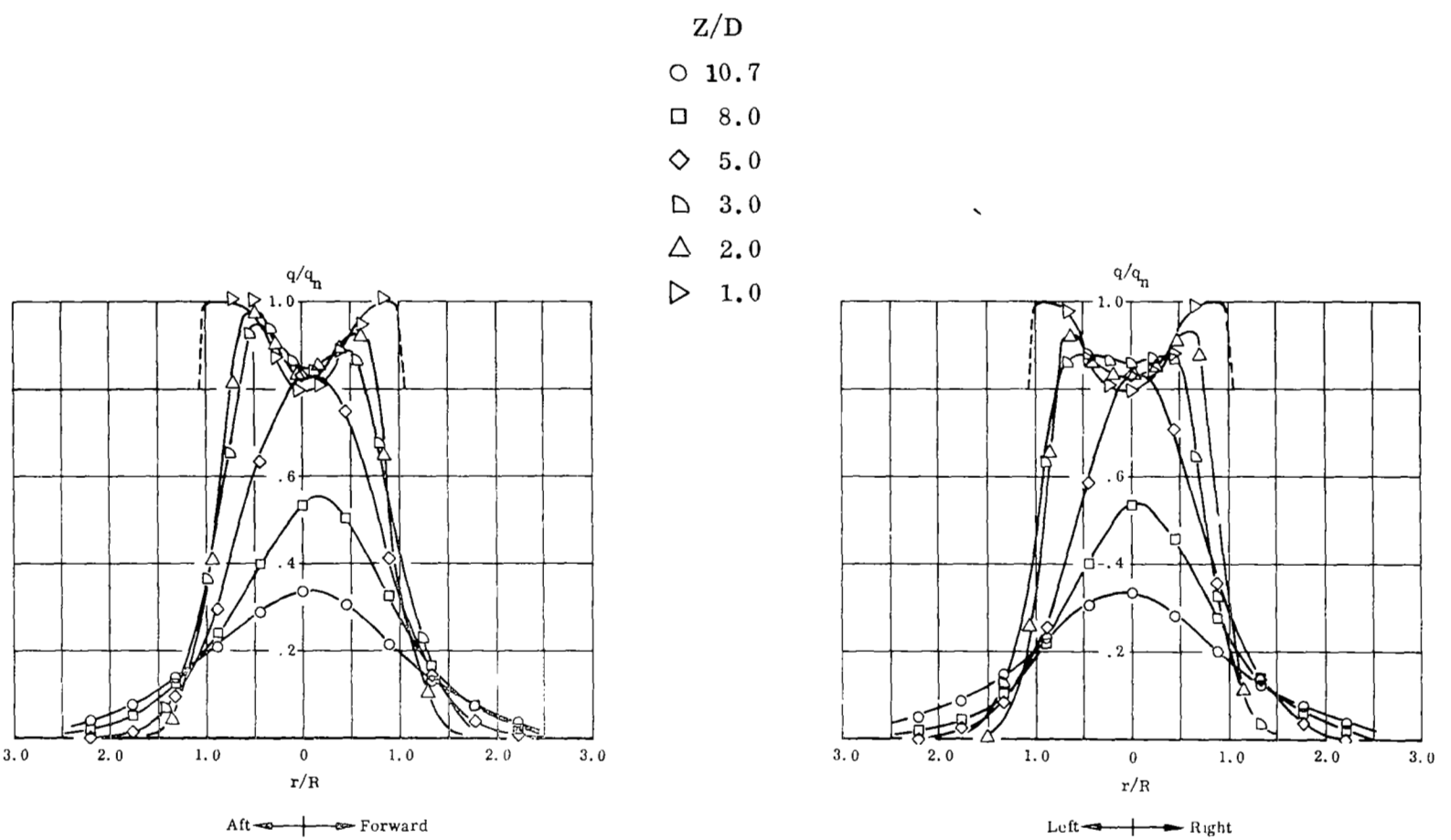

(b) Aft Nozzle

FIGURE 11 (cont'd). EXHAUST JET CALIBRATION - BASIC NOZZLE

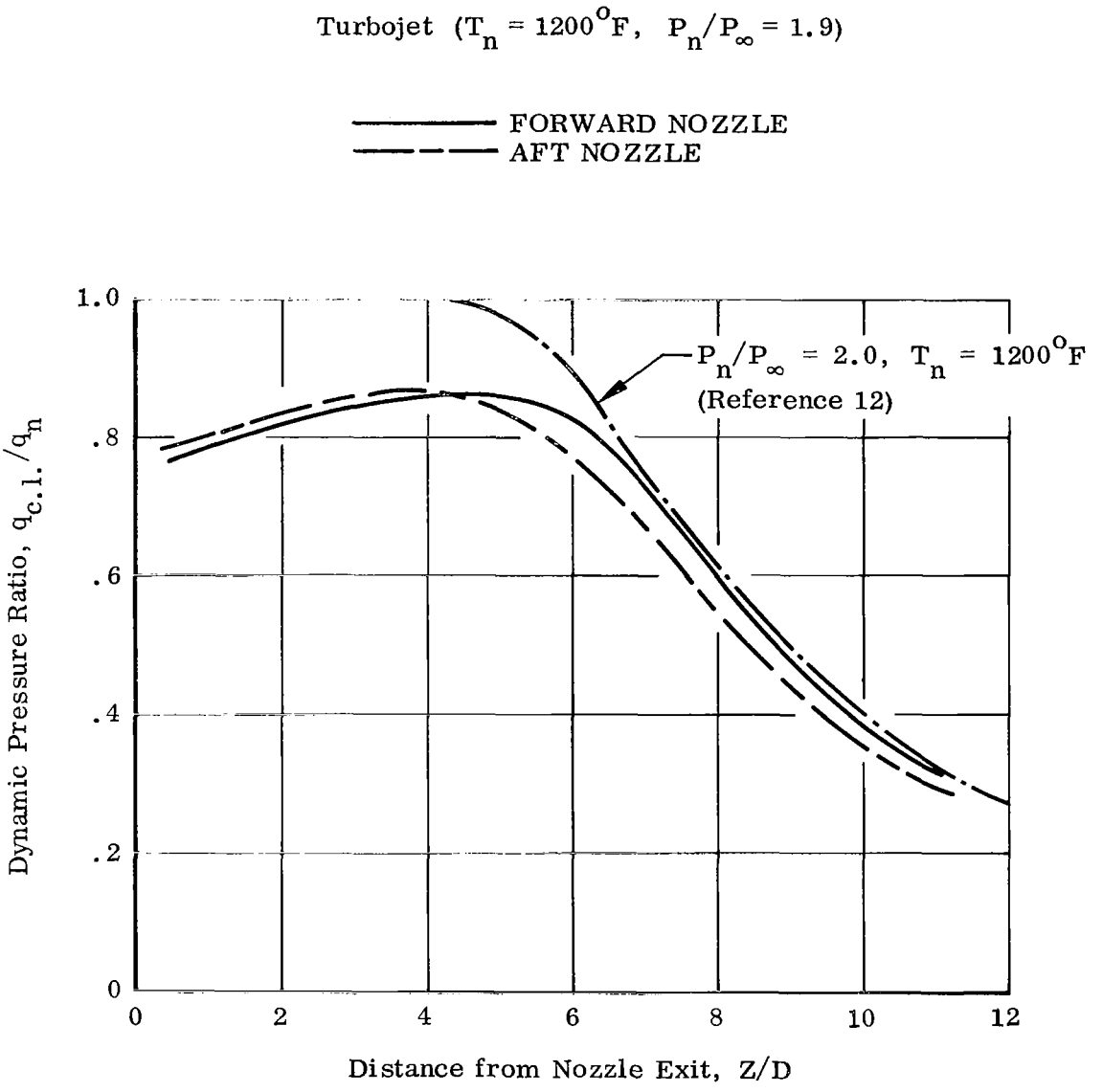

FIGURE 12. EXHAUST JET CENTERLINE DYNAMIC PRESSURE DECAY - BASIC NOZZLE

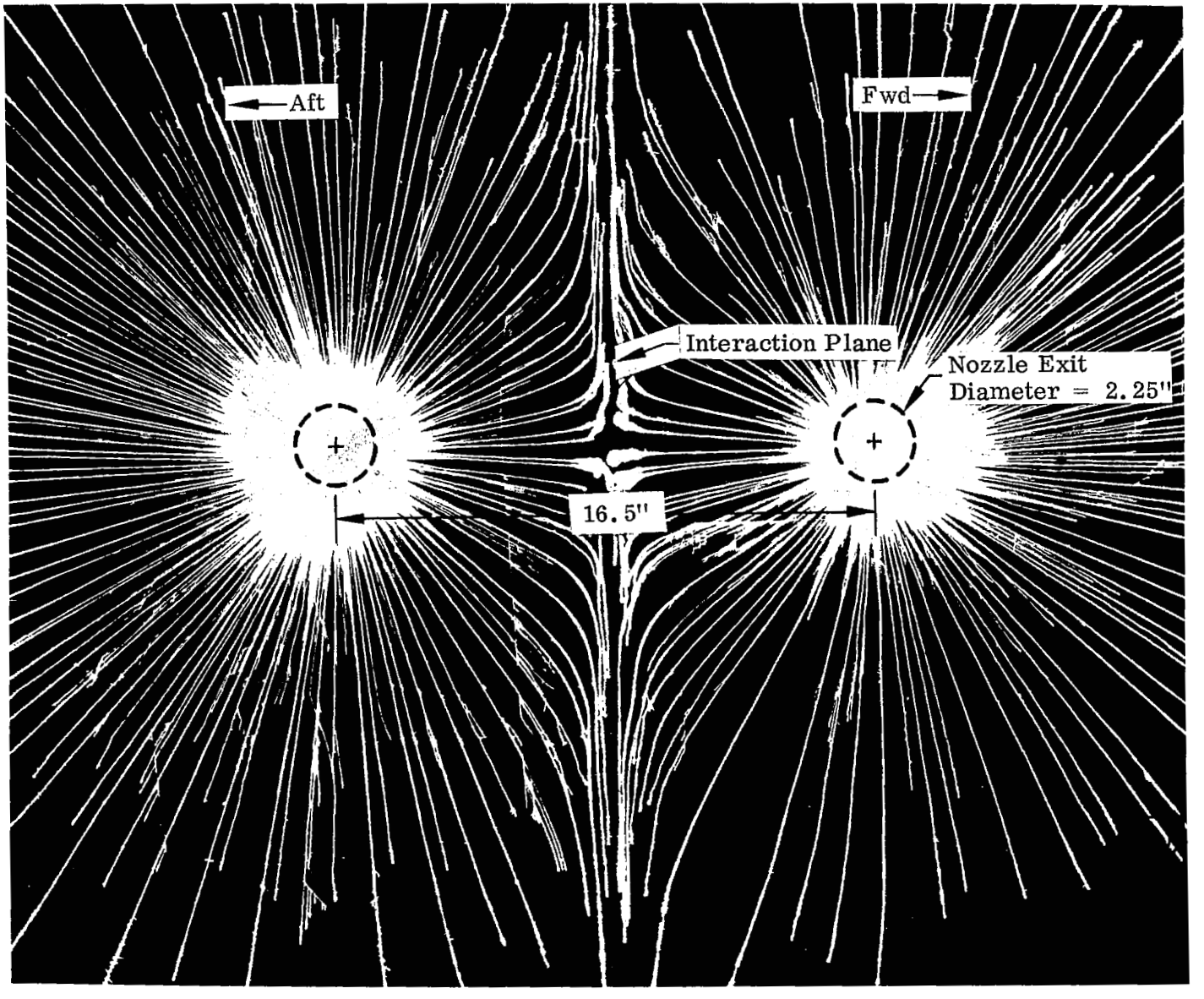

FIGURE 13. GROUND PLANE OIL STREAK PATTERN

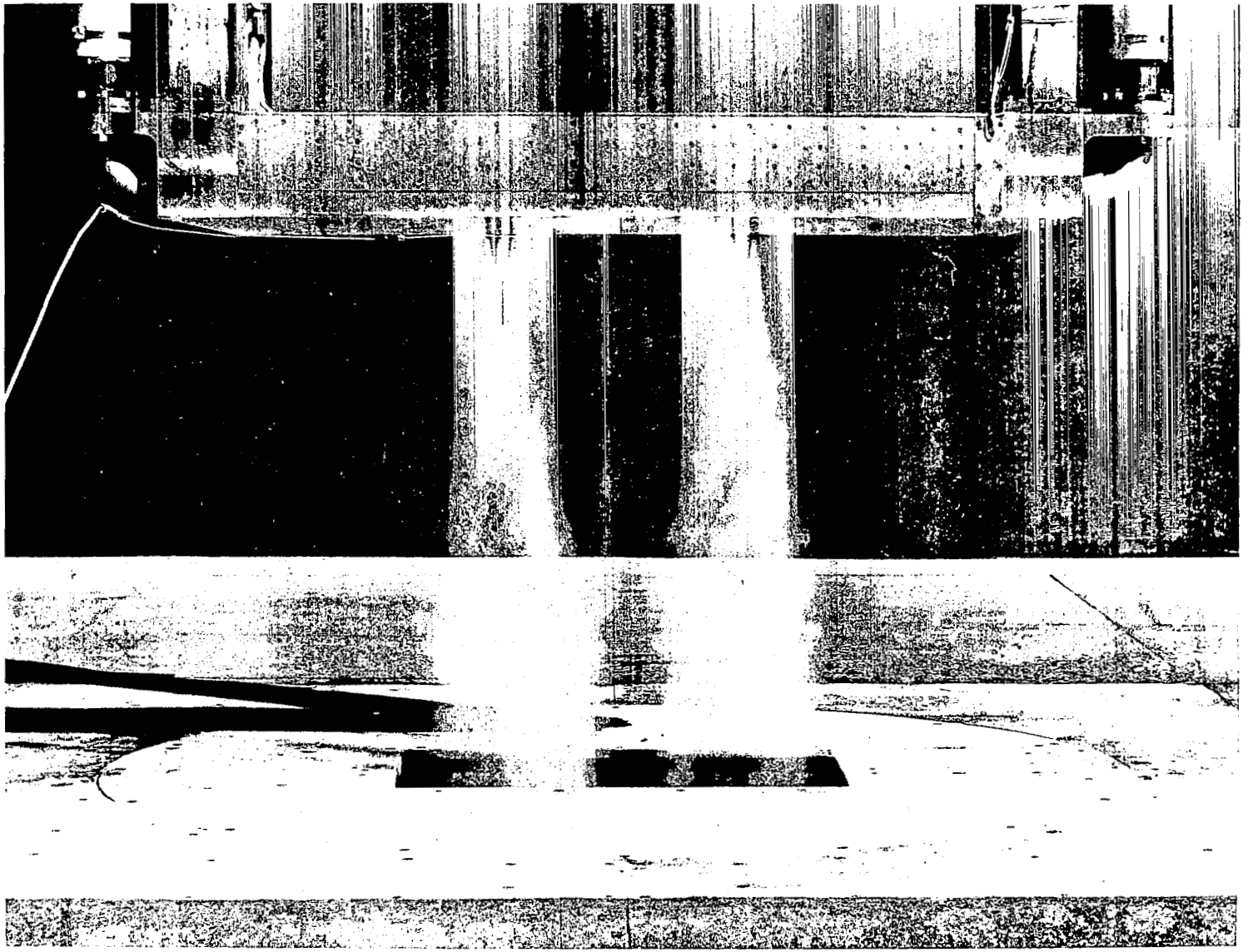

FIGURE 14. EXHAUST JET FLOW VISUALIZATION

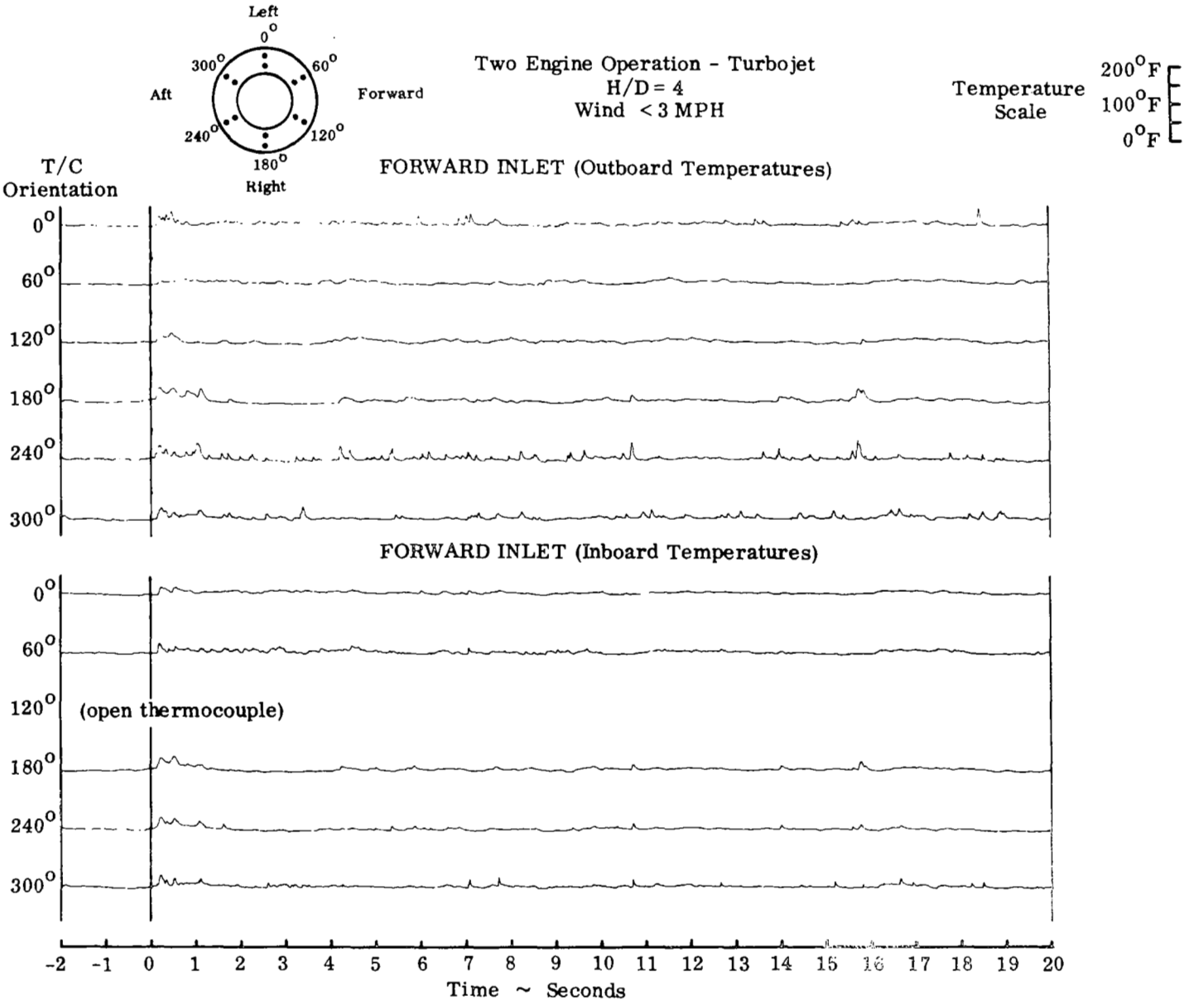

FIGURE 15. REFERENCE CONFIGURATION INLET TEMPERATURE HISTORY - LOW WIND

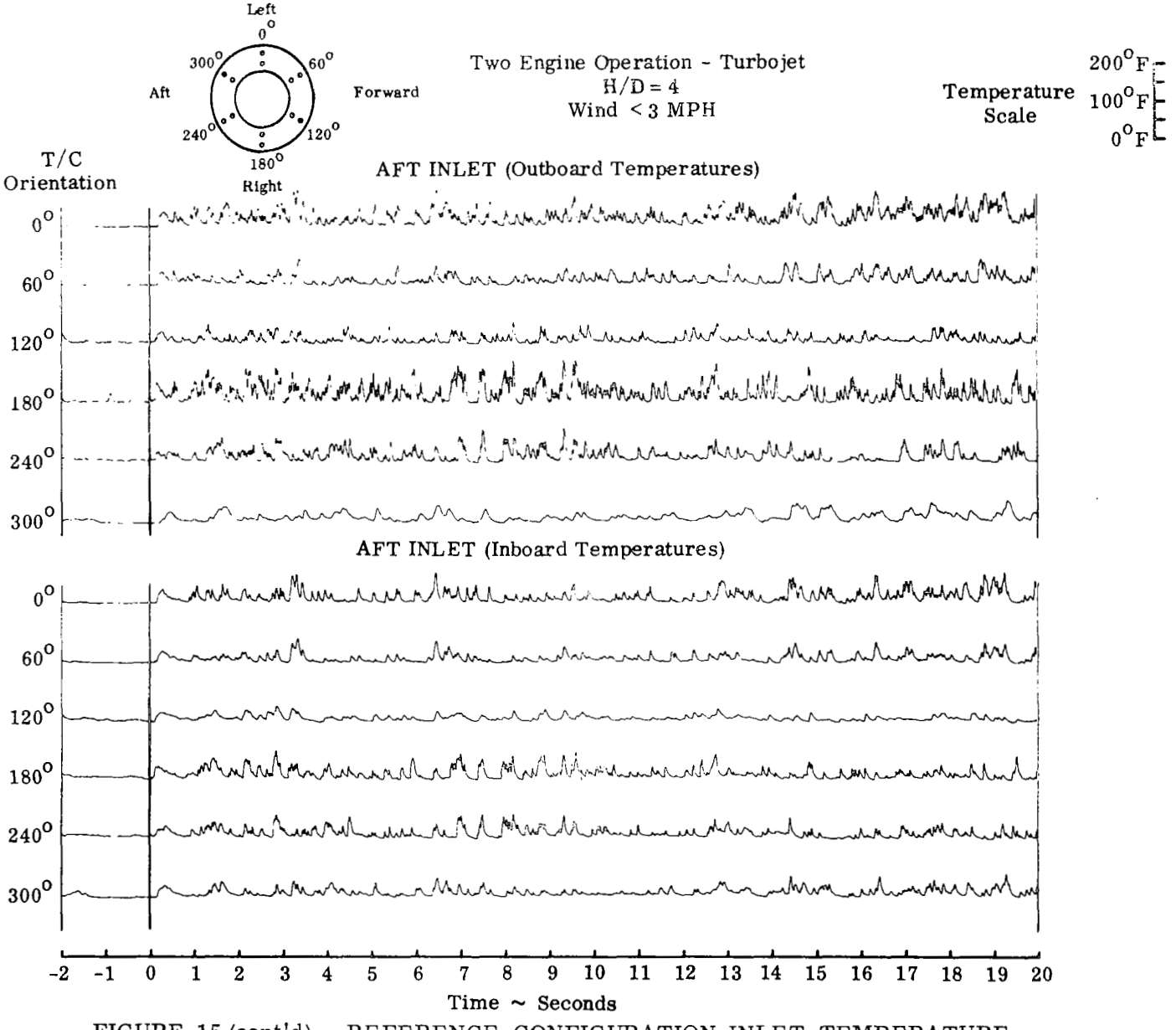

FIGURE 15 (cont'd). REFERENCE CONFIGURATION INLET TEMPERATURE HISTORY - LOW WIND

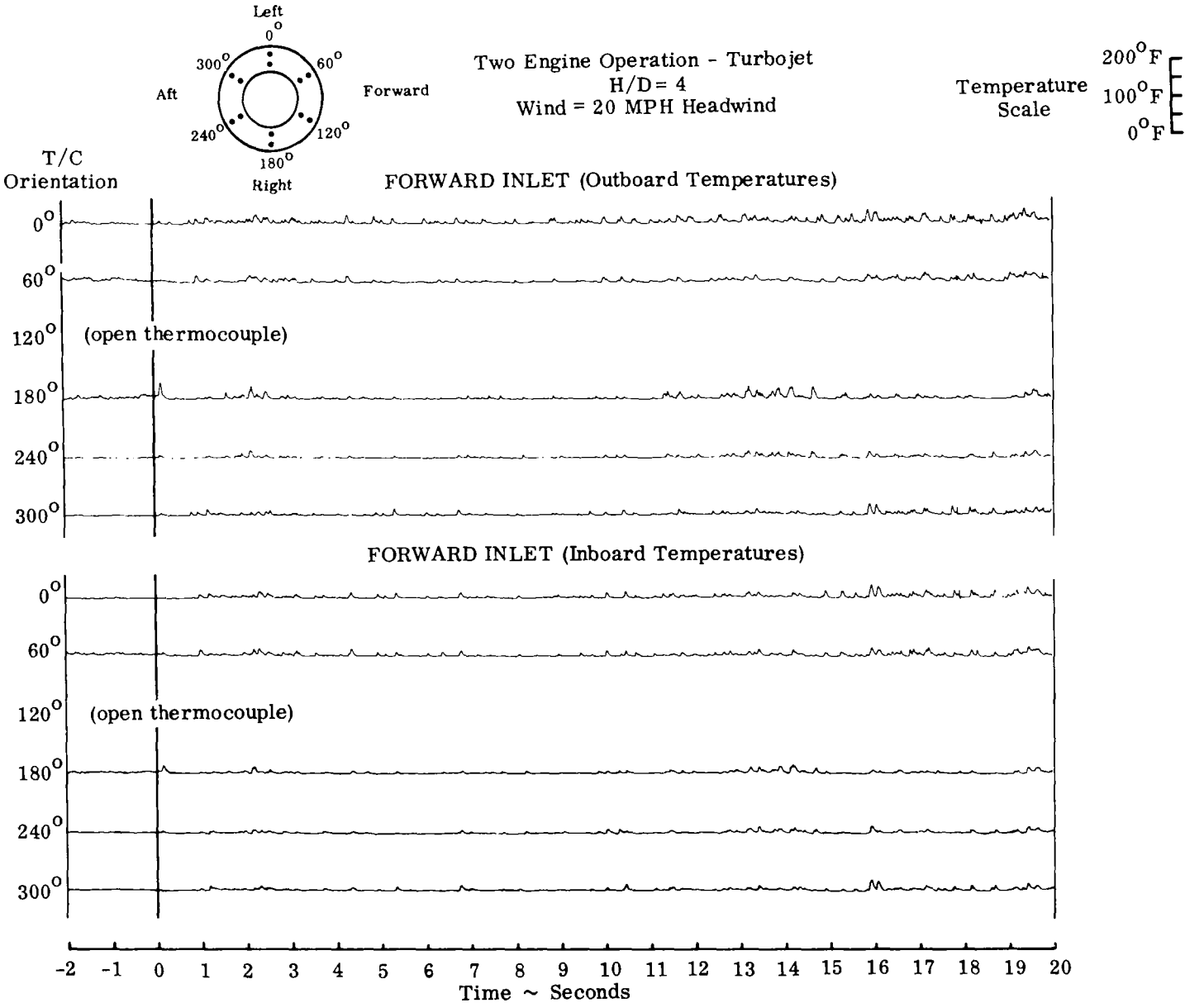

FIGURE 16. REFERENCE CONFIGURATION INLET TEMPERATURE HISTORY - 20 MPH HEADWIND

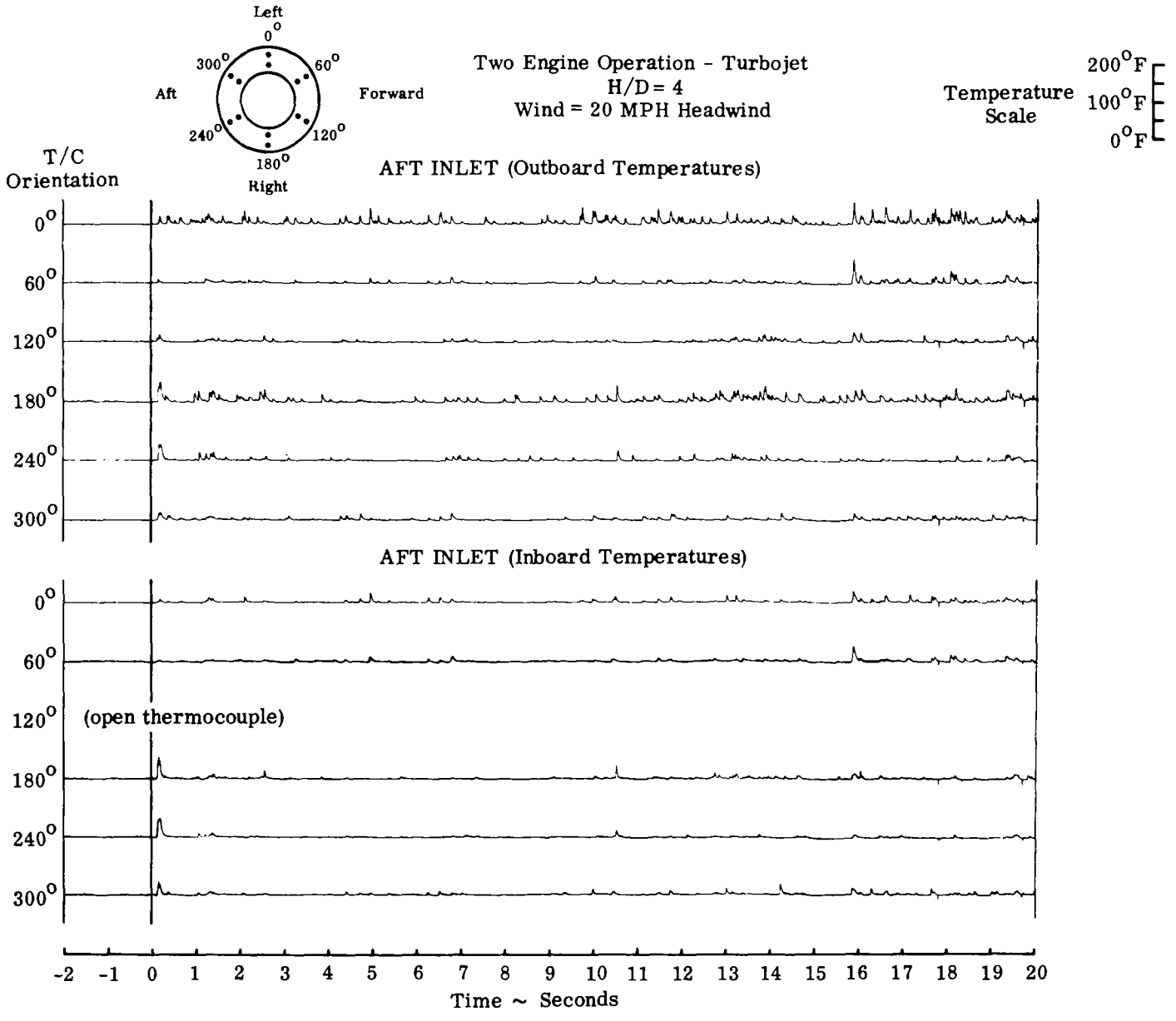

FIGURE 16 (cont'd). REFERENCE CONFIGURATION INLET TEMPERATURE HISTORY - 20 MPH HEADWIND

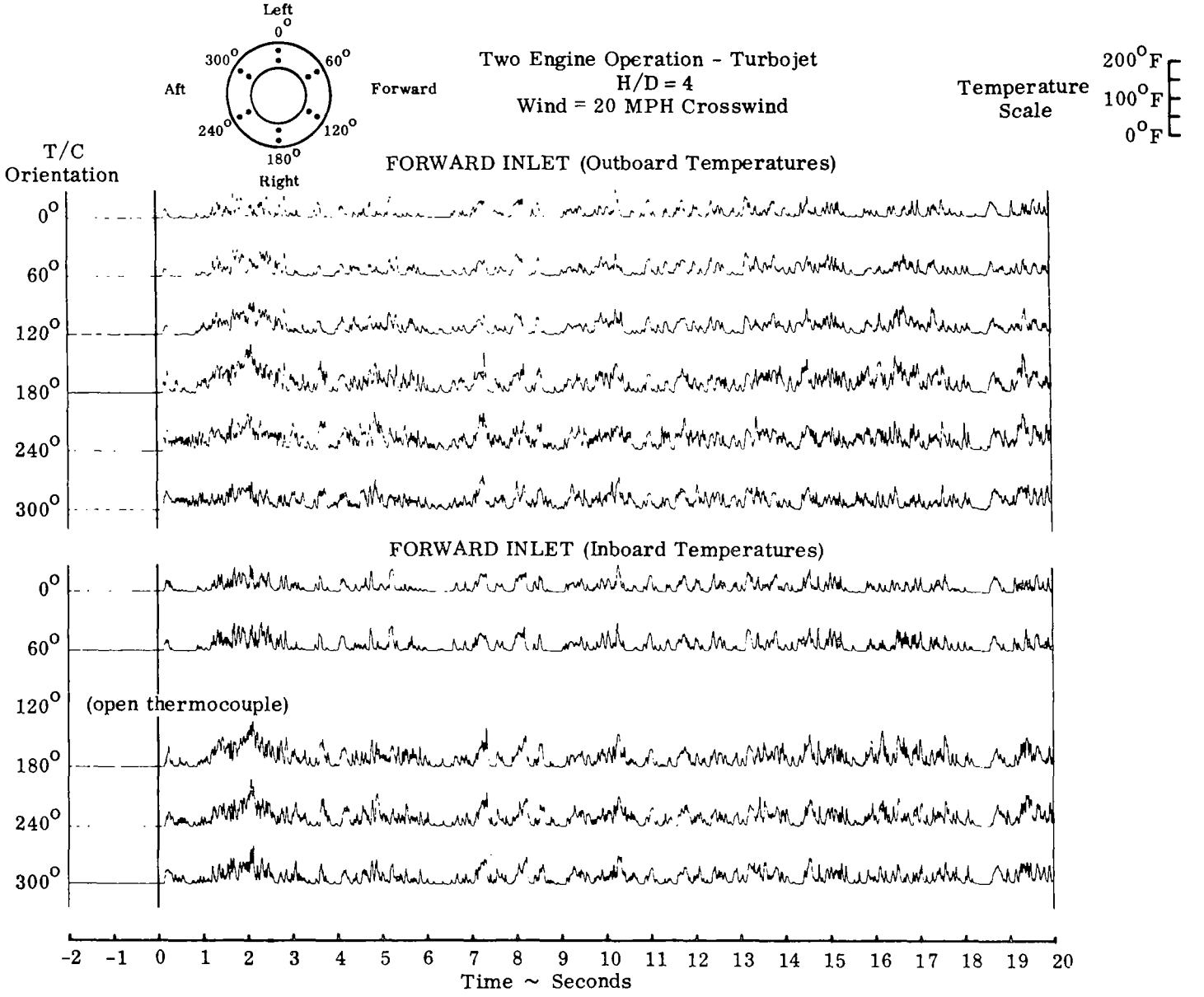

FIGURE 17. REFERENCE CONFIGURATION INLET TEMPERATURE HISTORY - 20 MPH CROSSWIND

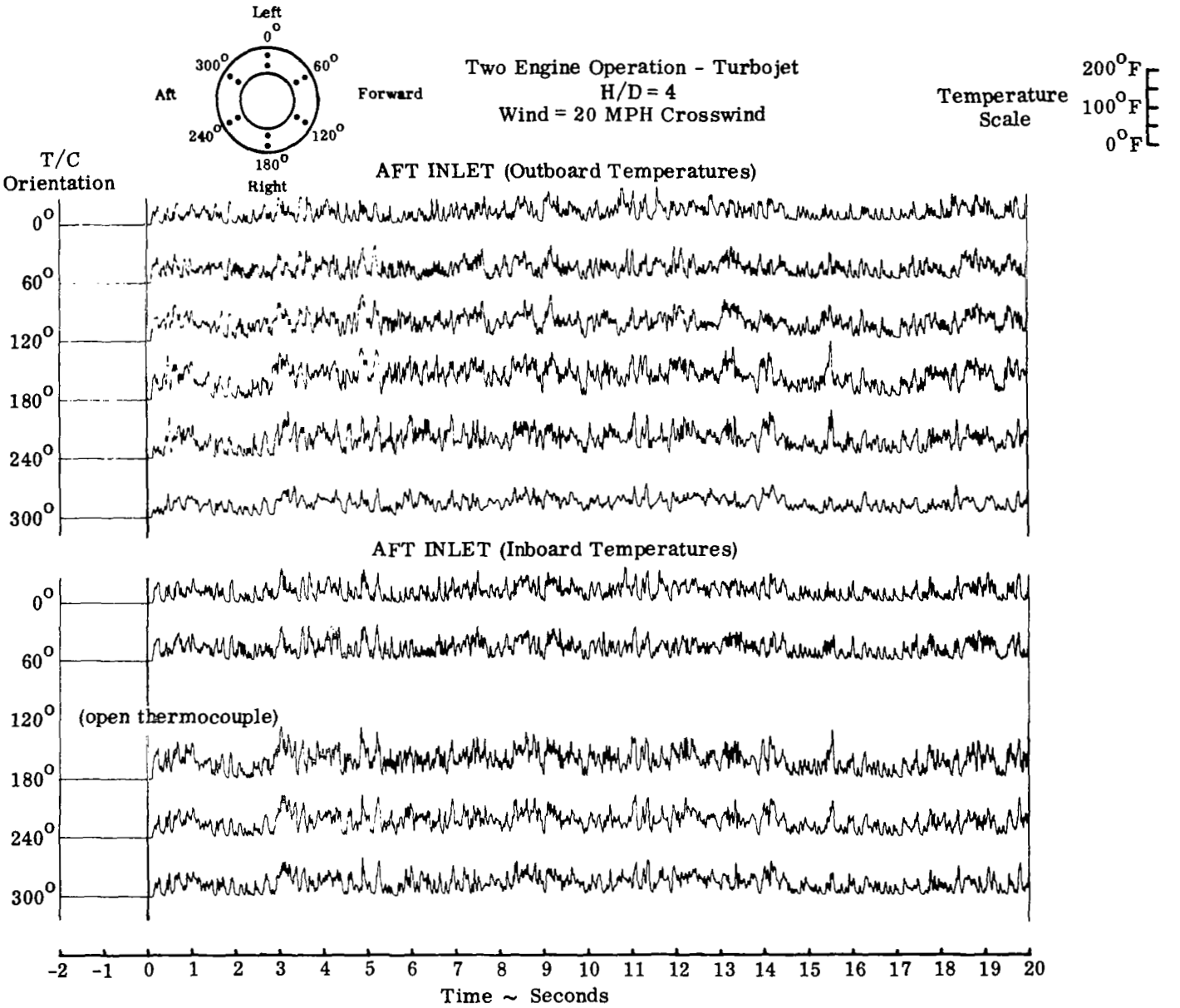

FIGURE 17 (cont'd). REFERENCE CONFIGURATION INLET TEMPERATURE HISTORY - 20 MPH CROSSWIND

Two Engine Operation
H/D = 4
Wind < 3 MPH

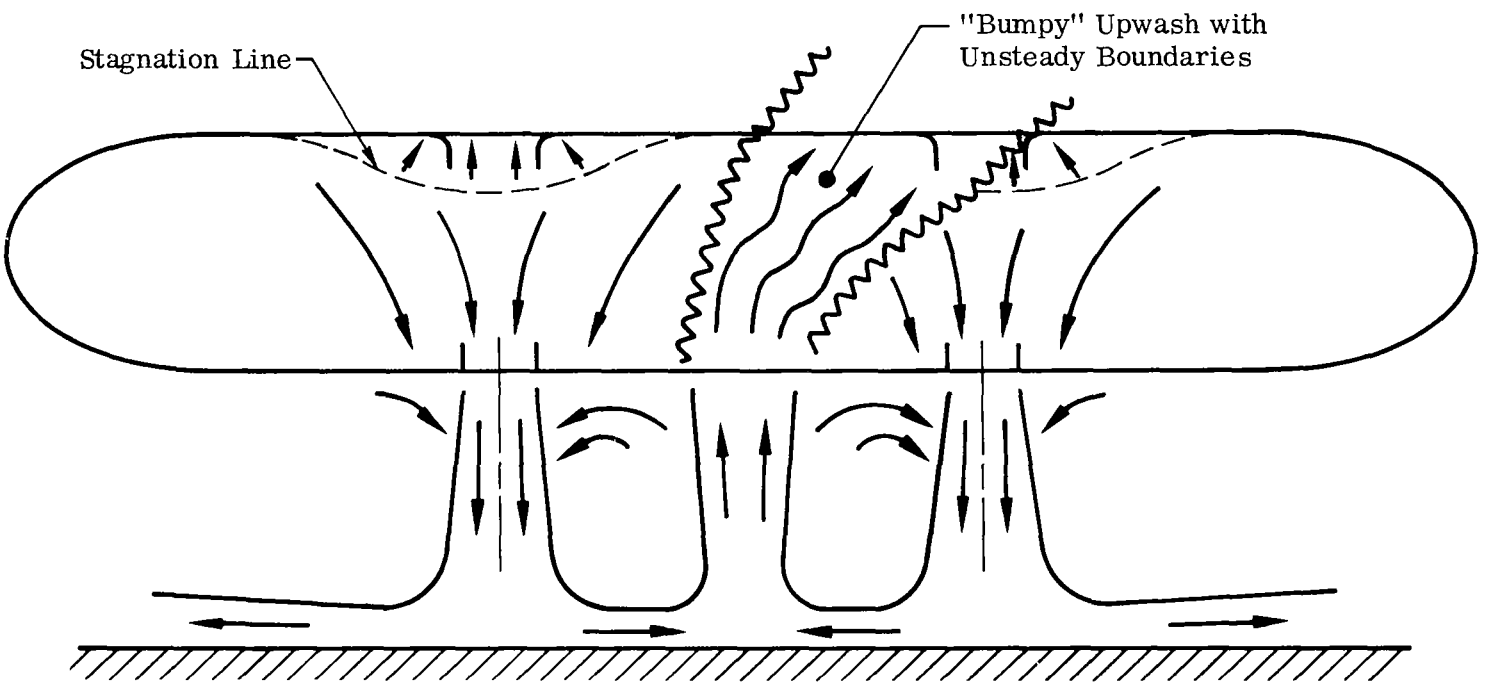

FIGURE 18. REFERENCE CONFIGURATION FLOW FIELD SCHEMATIC

Two Engine Operation - Turbojet
H/D = 4
Wind < 3 MPH

FORWARD INLET

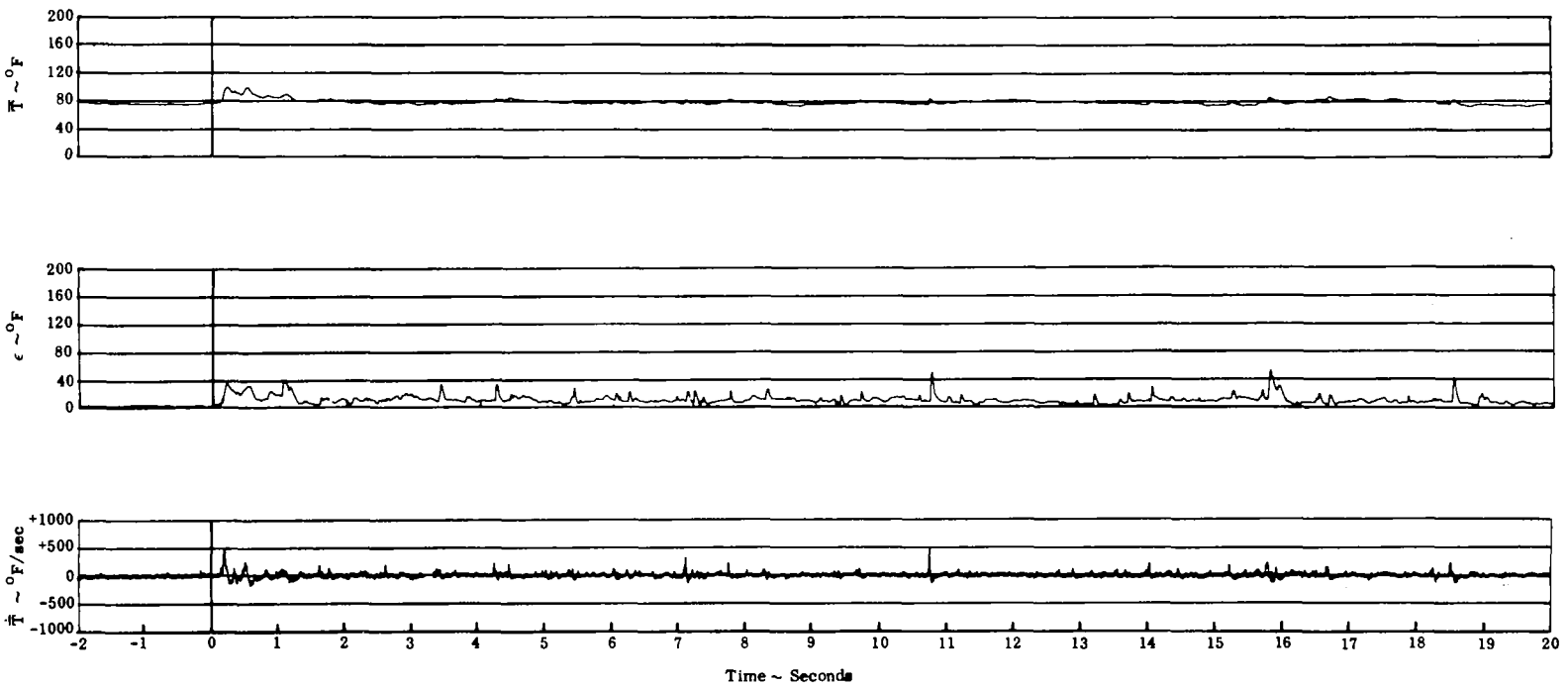

FIGURE 19. REFERENCE CONFIGURATION INGESTION HISTORY - LOW WIND

Two Engine Operation - Turbojet
H/D = 4
Wind < 3 MPH

AFT INLET

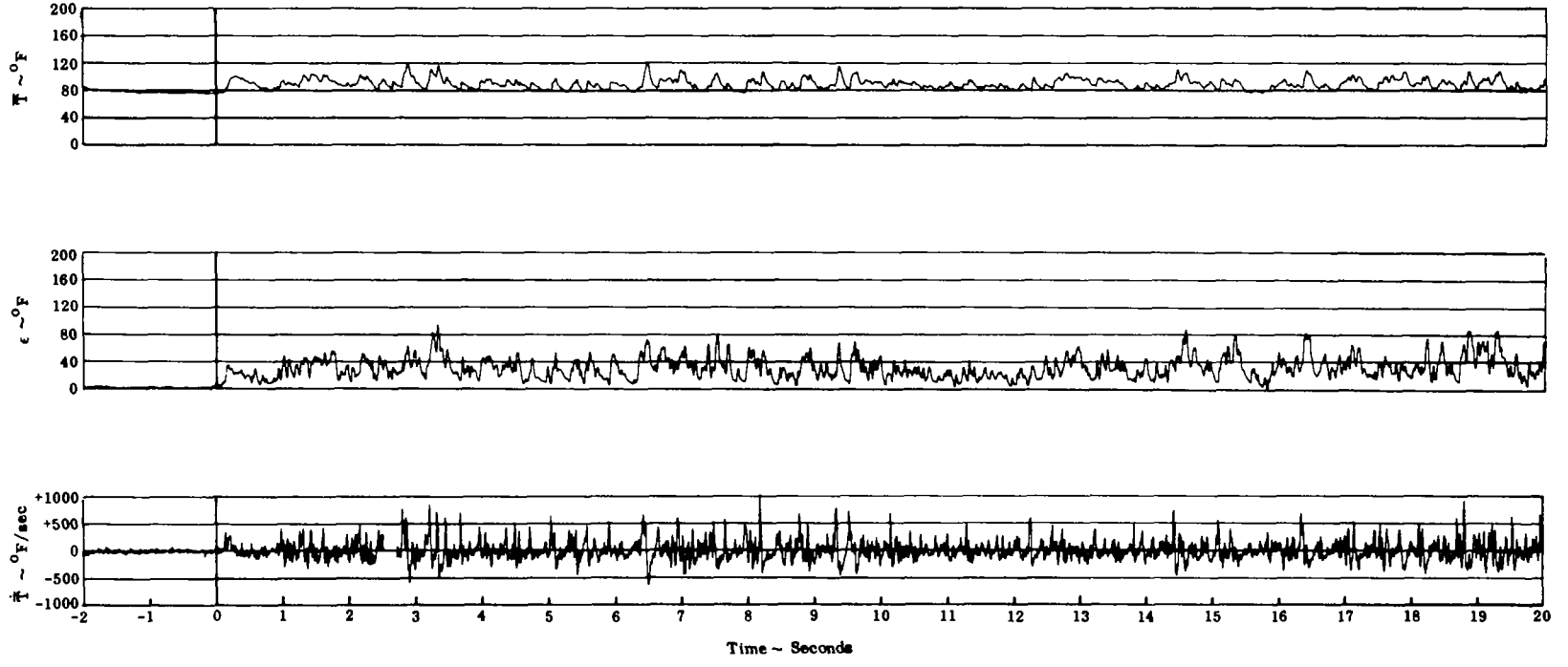

FIGURE 19 (cont'd). REFERENCE CONFIGURATION INGESTION HISTORY - LOW WIND

Two Engine Operation - Turbojet
H/D = 4
Wind = 20 MPH Headwind

FORWARD INLET

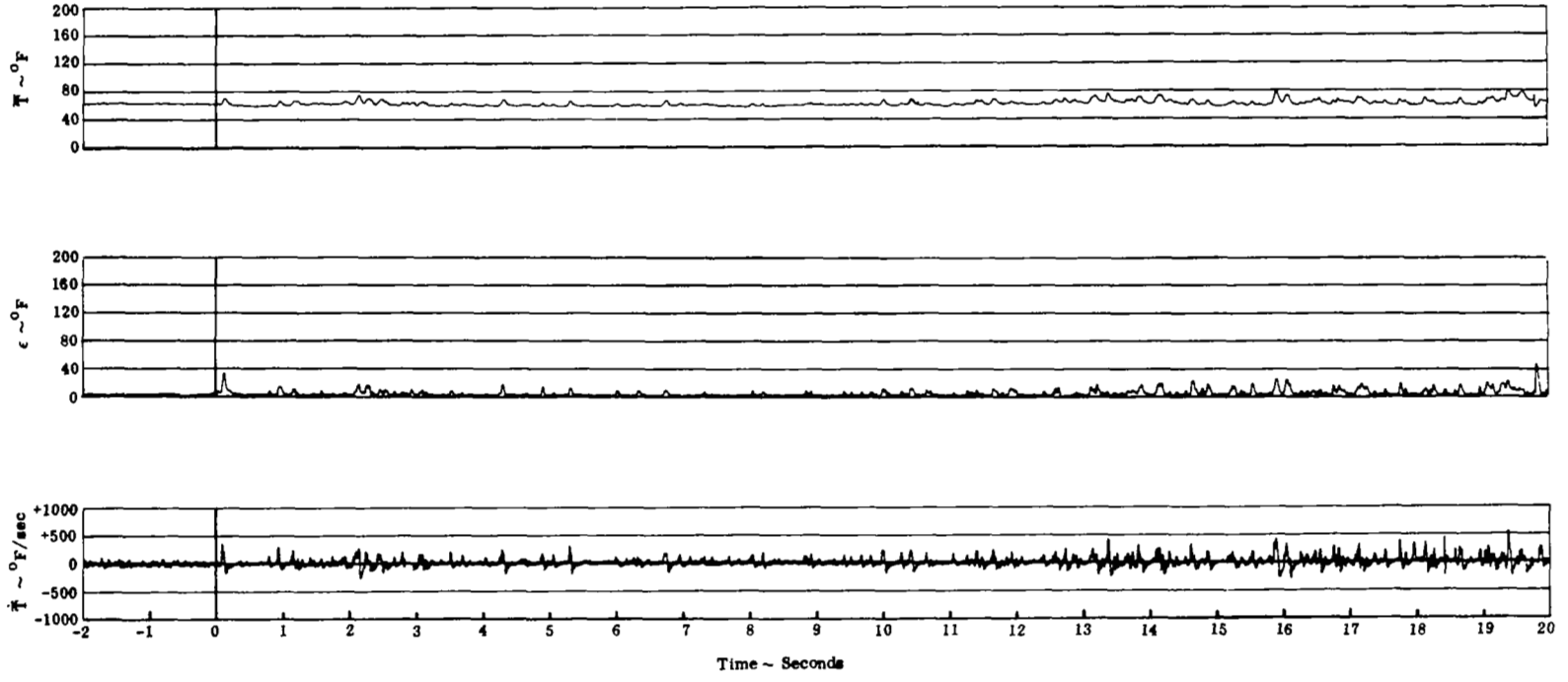

FIGURE 20. REFERENCE CONFIGURATION INGESTION HISTORY - 20 MPH HEADWIND

Two Engine Operation - Turbojet
H/D = 4
Wind = 20 MPH Headwind

AFT INLET

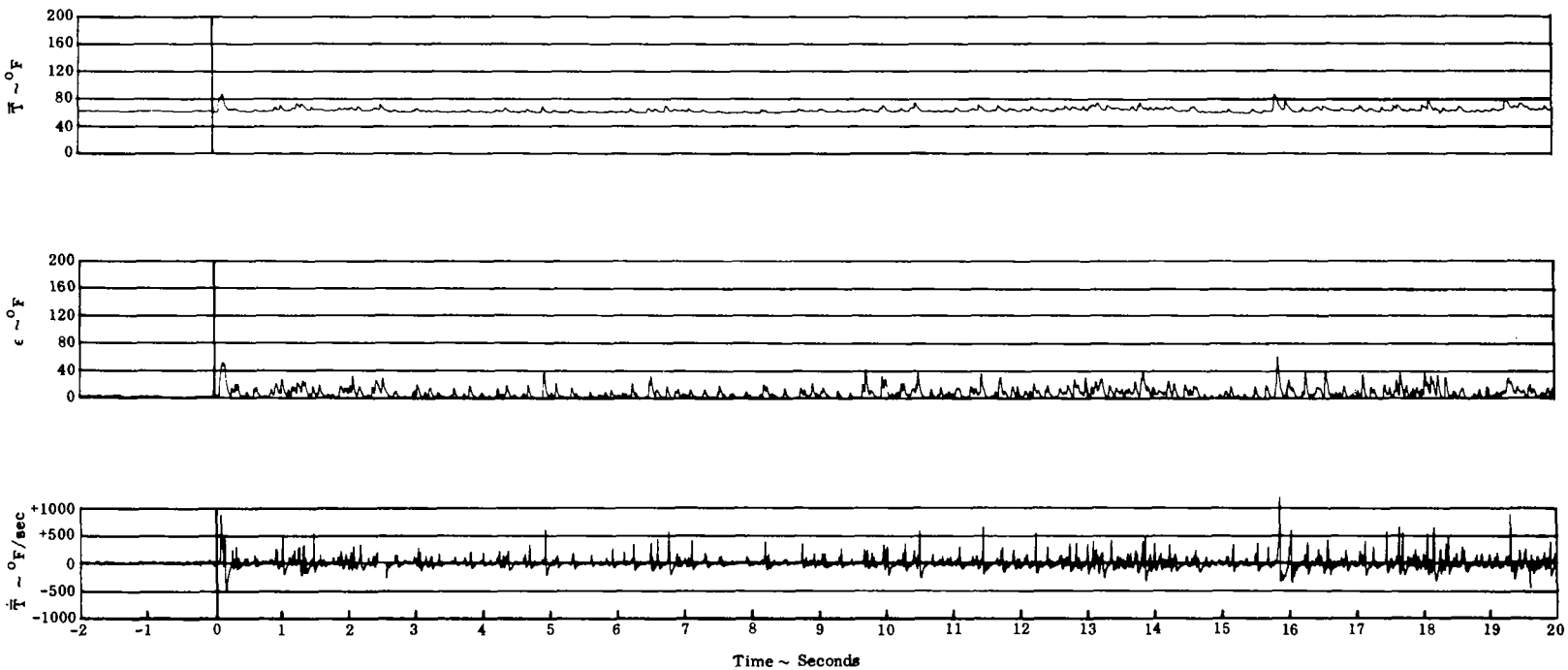

FIGURE 20 (cont'd). REFERENCE CONFIGURATION INGESTION HISTORY - 20 MPH HEADWIND

Two Engine Operation - Turbojet
H/D = 4
Wind = 20 MPH Crosswind

FORWARD INLET

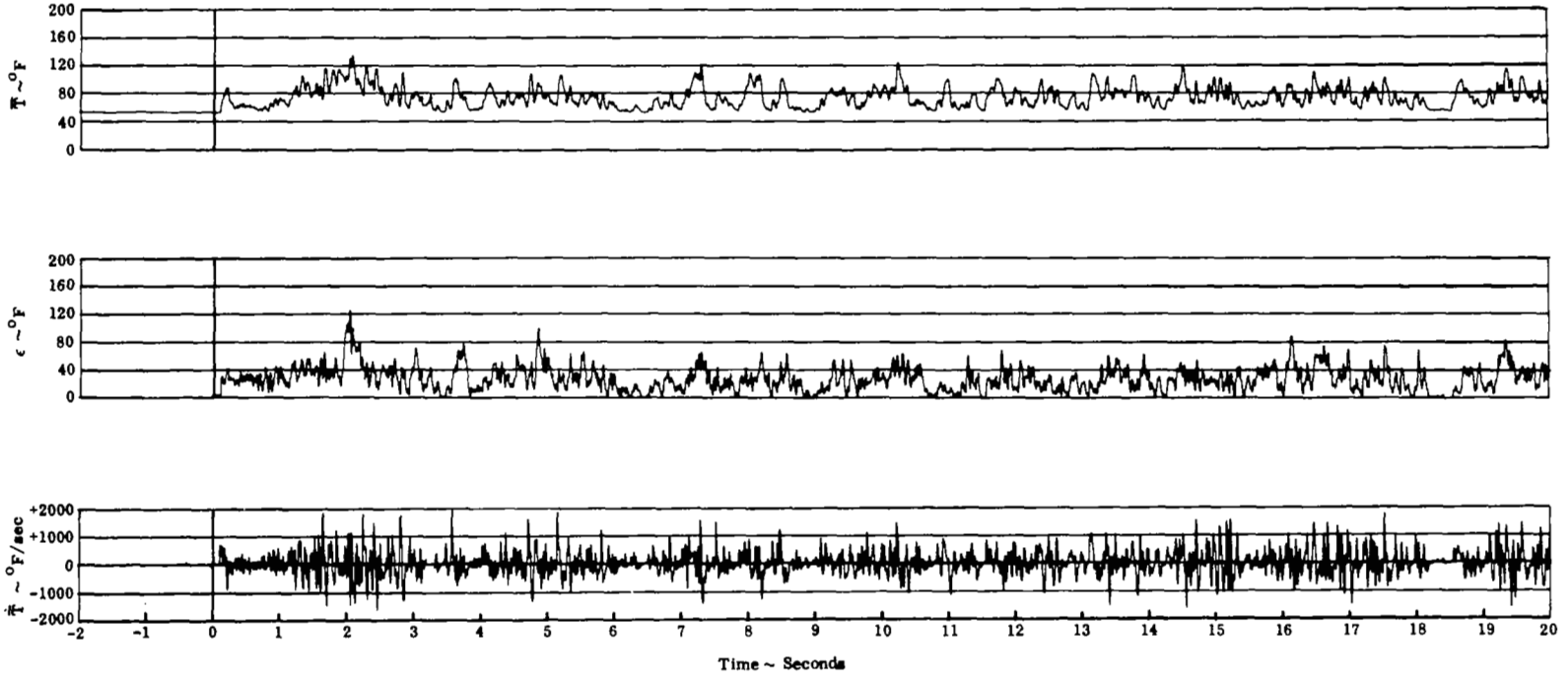

FIGURE 21. REFERENCE CONFIGURATION INGESTION HISTORY - 20 MPH CROSSWIND

Two Engine Operation - Turbojet
H/D = 4, S/D = 7.35
Wind = 20 MPH Crosswind

AFT INLET

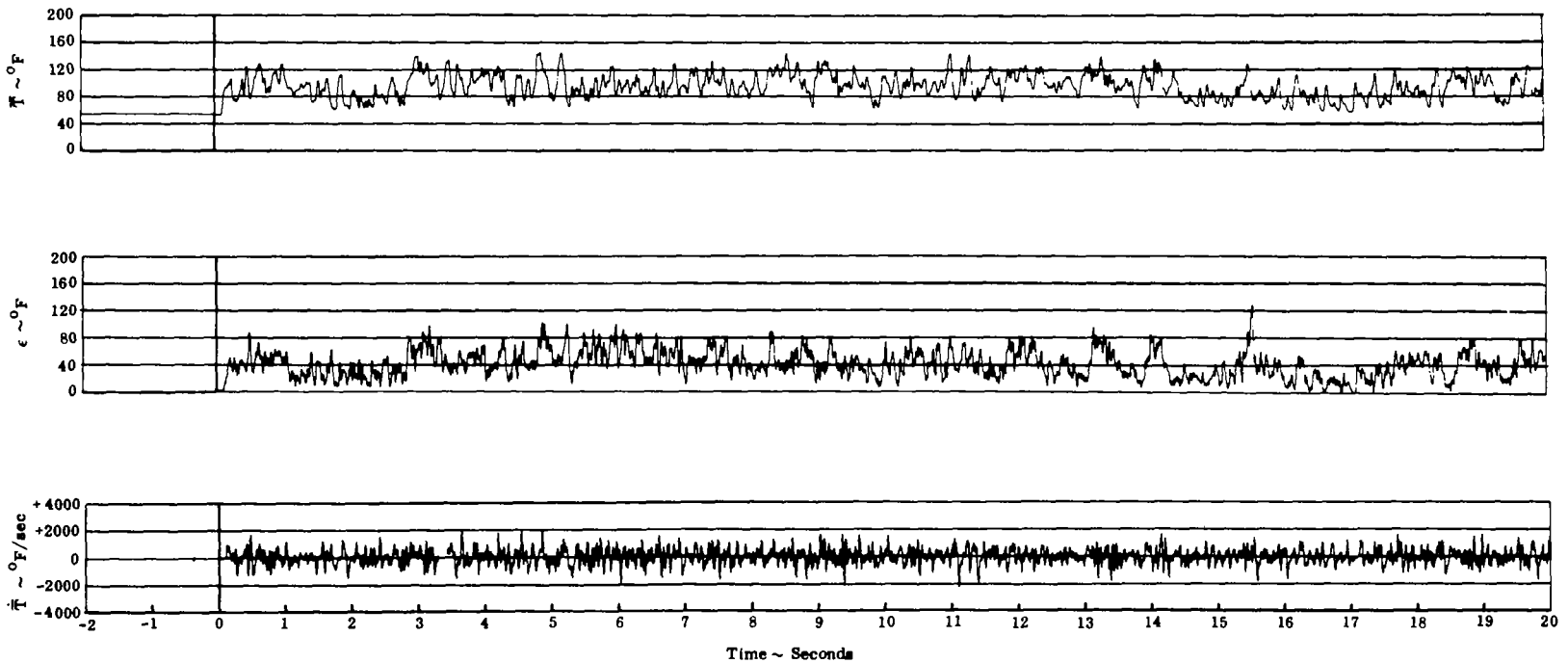

FIGURE 21 (cont'd). REFERENCE CONFIGURATION INGESTION HISTORY - 20 MPH CROSSWIND

Two Engine Operation
Turbojet
Wind < 3 MPH

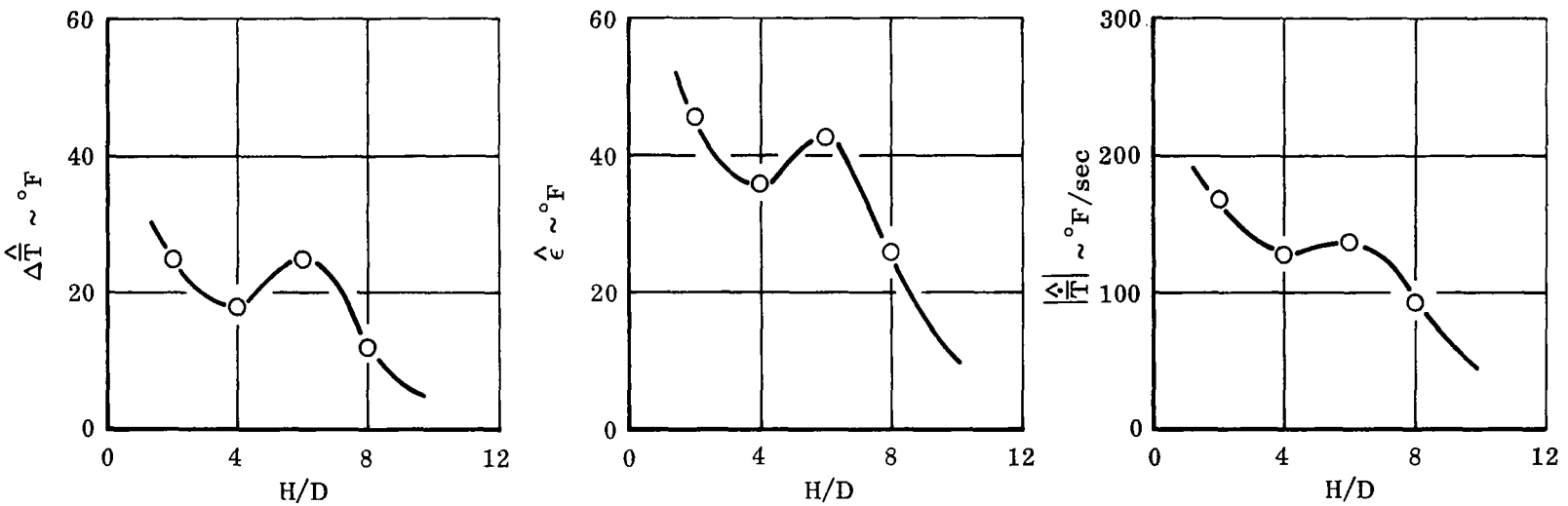

FIGURE 22. EFFECT OF H/D ON TIME-AVERAGE INGESTION CHARACTERISTICS FOR REFERENCE CONFIGURATION

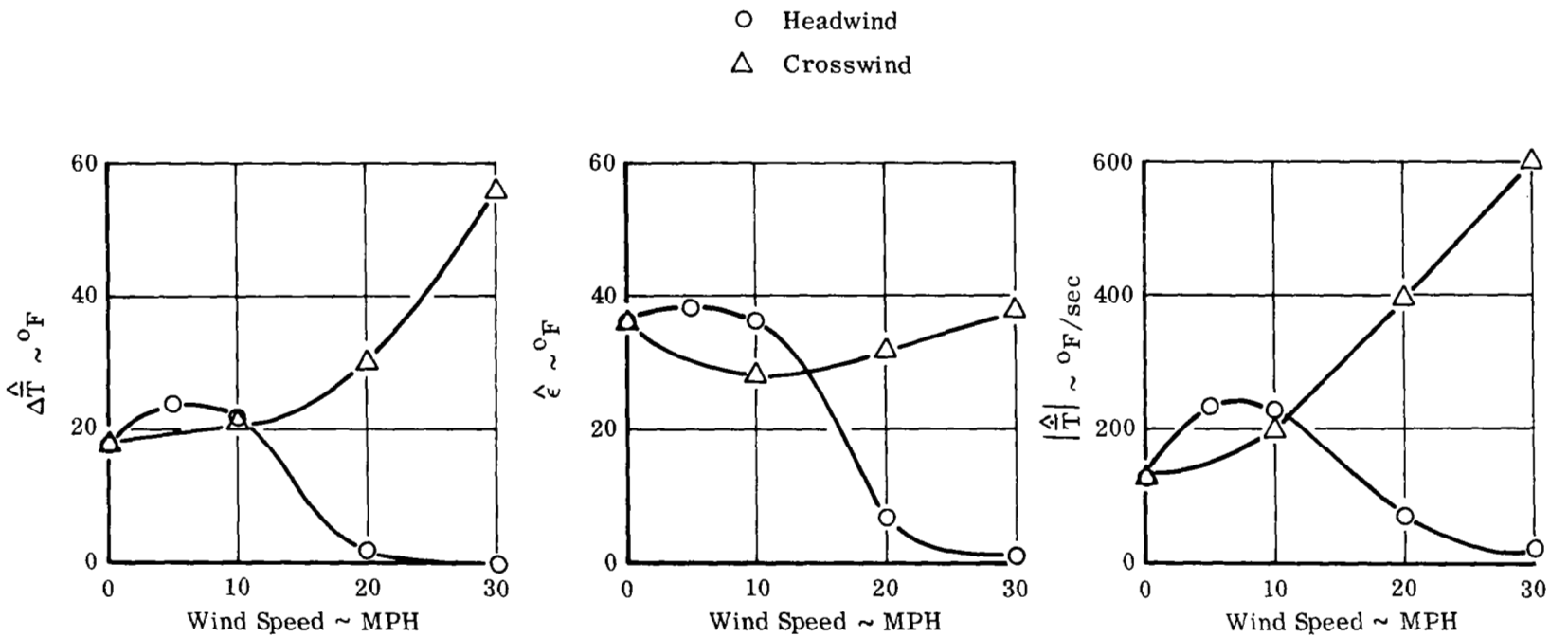

FIGURE 23. EFFECT OF WIND ON TIME-AVERAGE INGESTION CHARACTERISTICS FOR REFERENCE CONFIGURATION

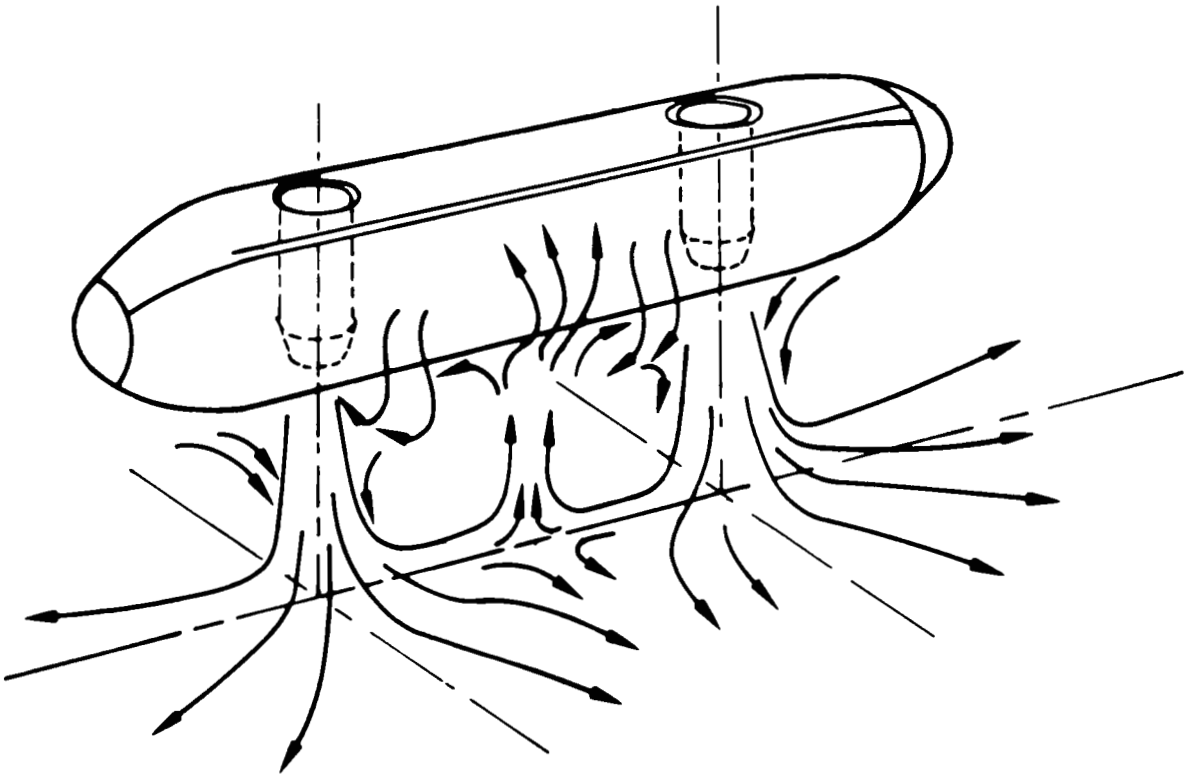

FIGURE 24. REFERENCE CONFIGURATION FLOW FIELD STRUCTURE

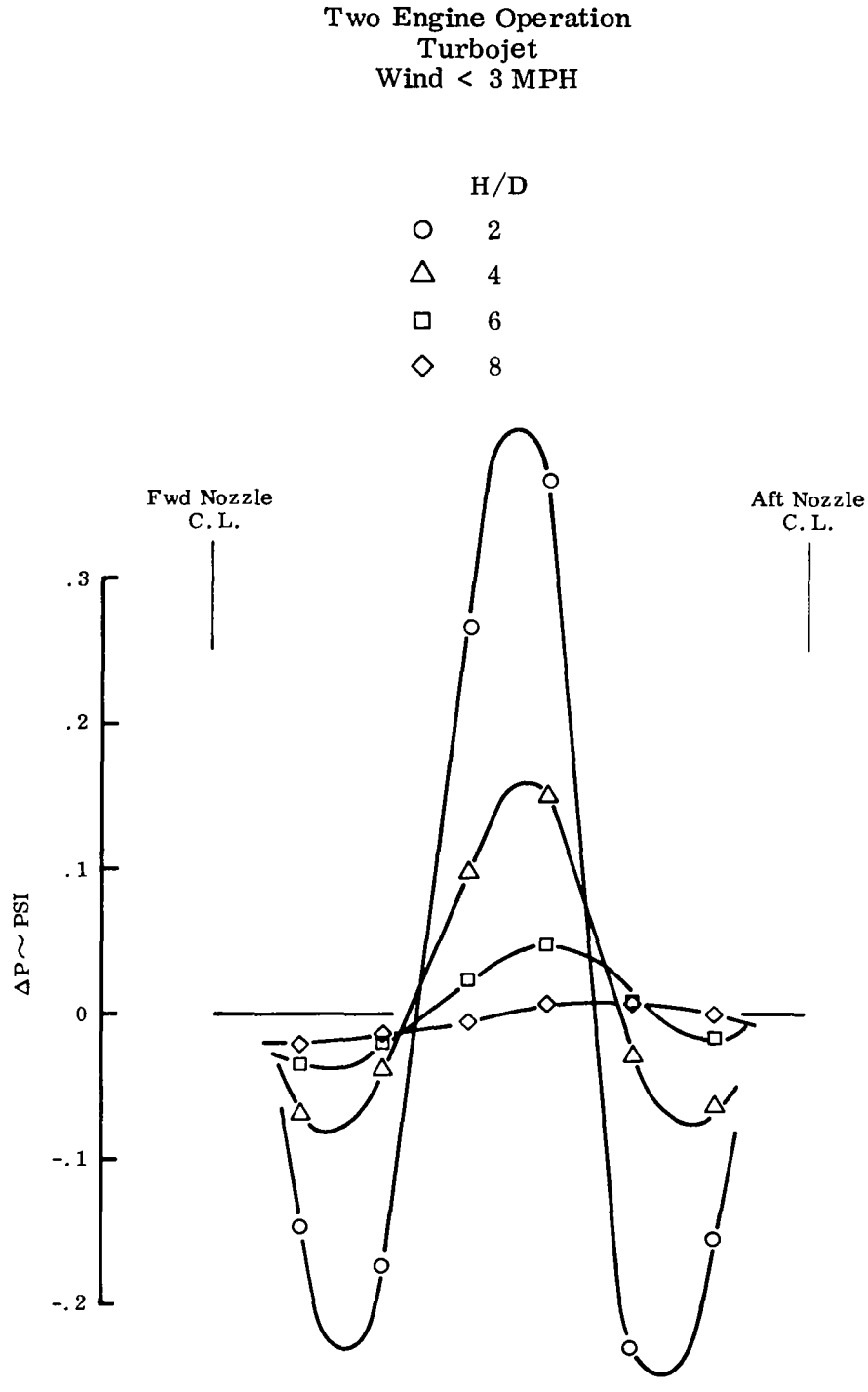

FIGURE 25. EFFECT OF H/D ON POD PRESSURE DISTRIBUTION FOR REFERENCE CONFIGURATION

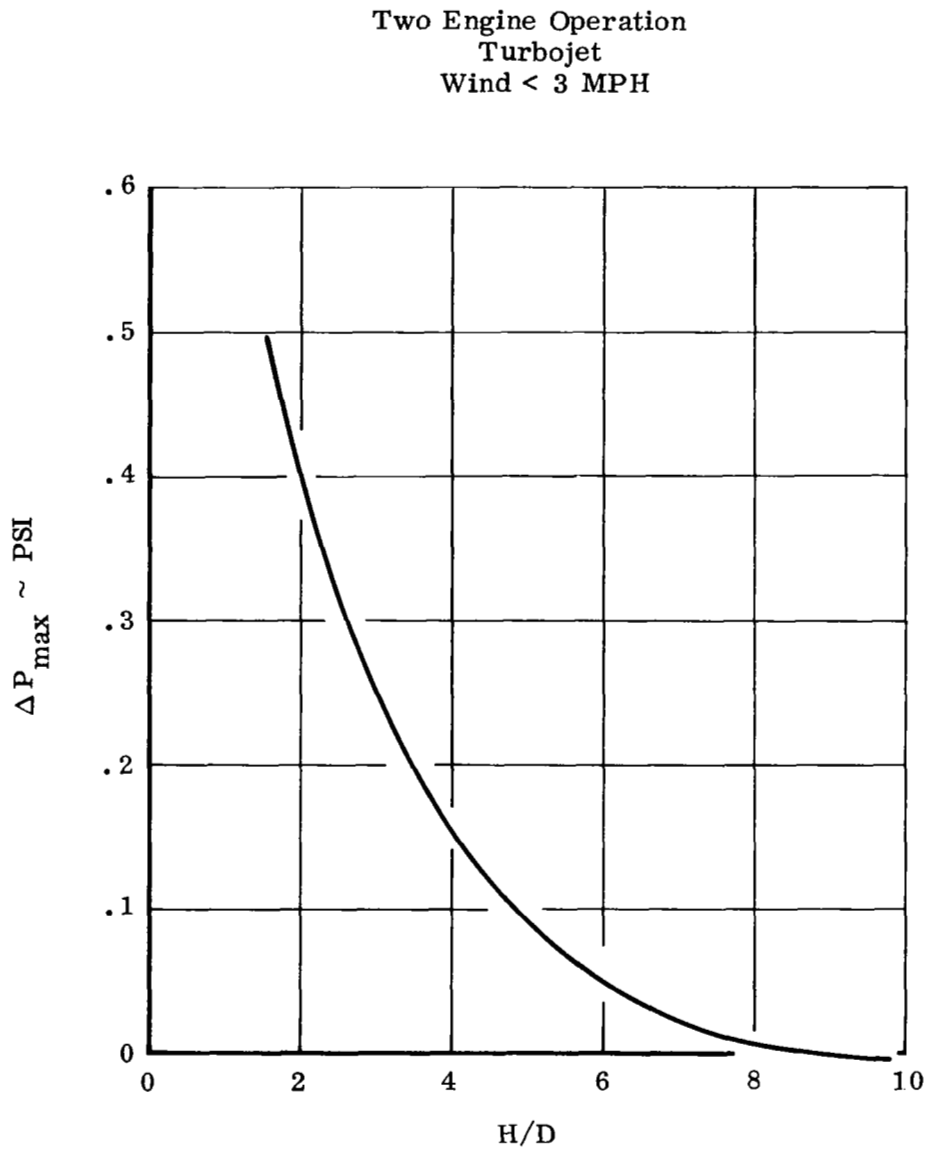

FIGURE 26. EFFECT OF H/D ON POD PEAK PRESSURE FOR REFERENCE CONFIGURATION

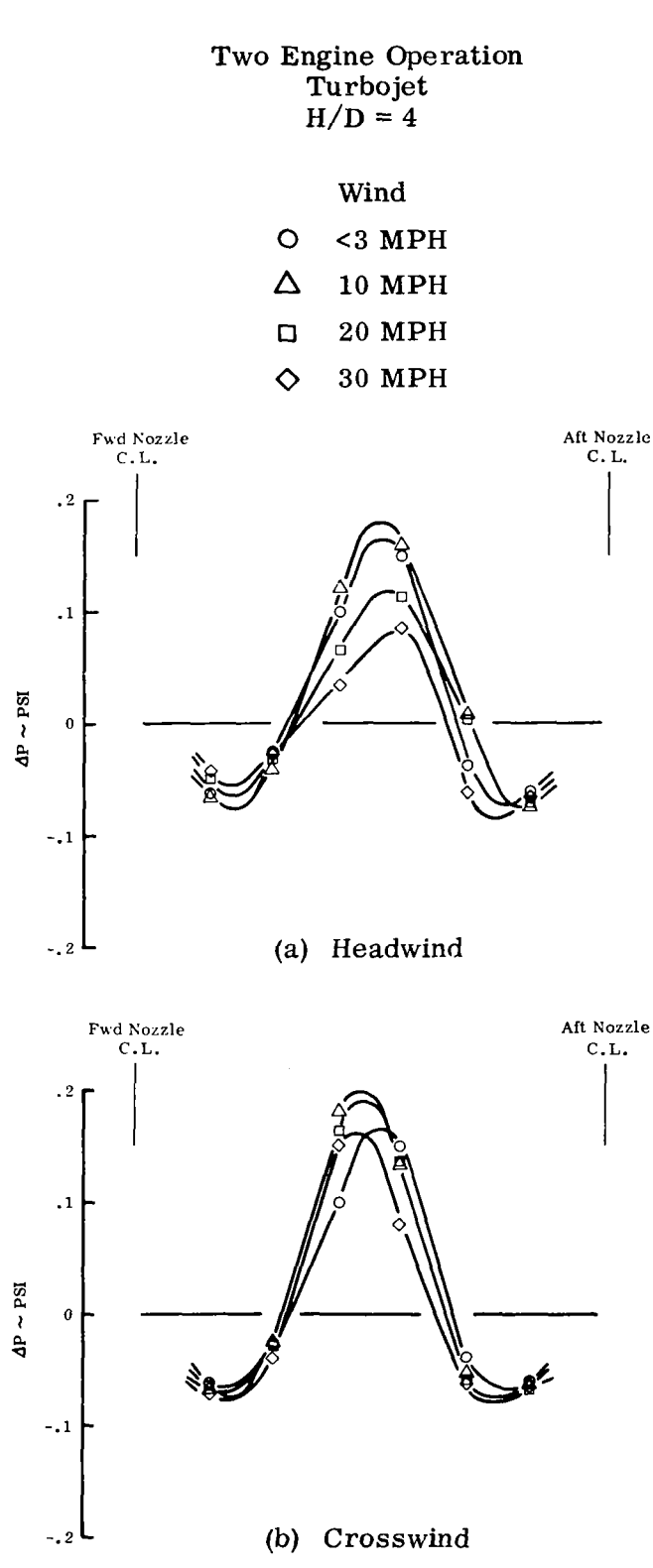

FIGURE 27. EFFECT OF WIND ON POD PRESSURE DISTRIBUTION FOR REFERENCE CONFIGURATION

Two Engine Operation
H/D = 4

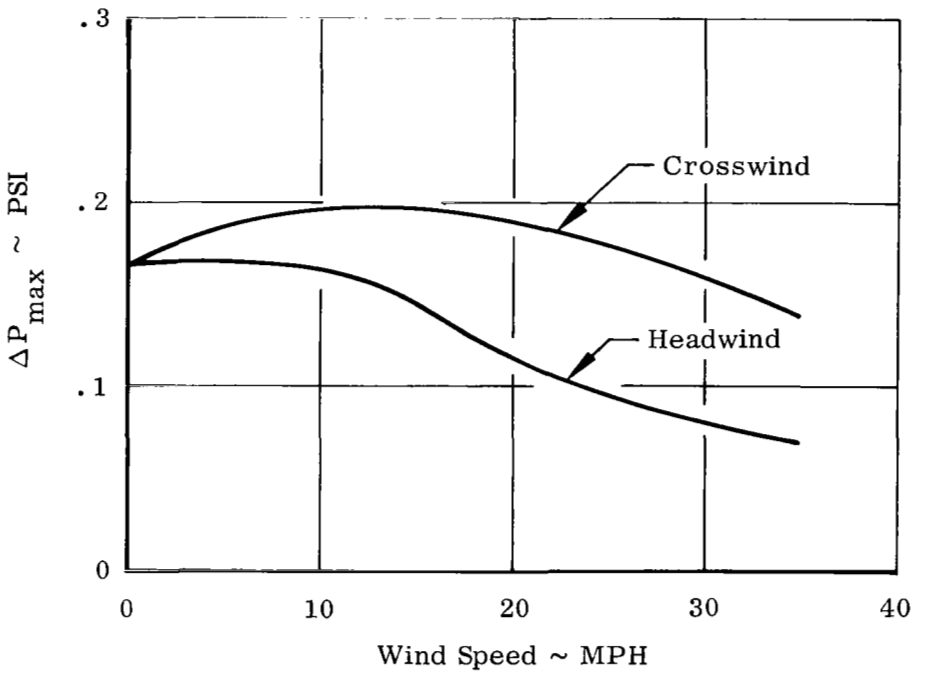

FIGURE 28. EFFECT OF WIND ON POD PEAK PRESSURE FOR REFERENCE CONFIGURATION

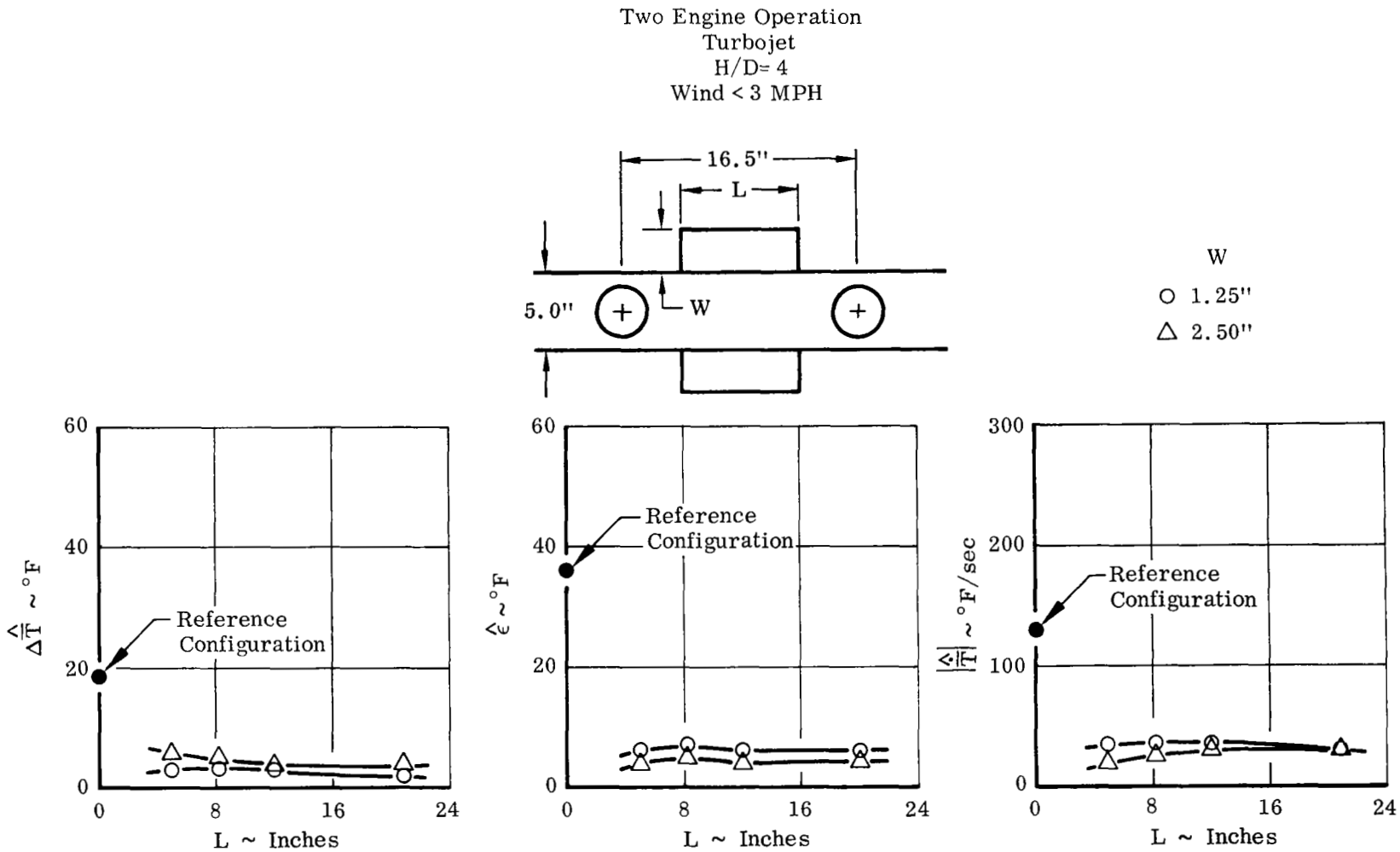

(a) Exit Plane Shield

FIGURE 29. EFFECT OF SHIELD SIZE AND LOCATION

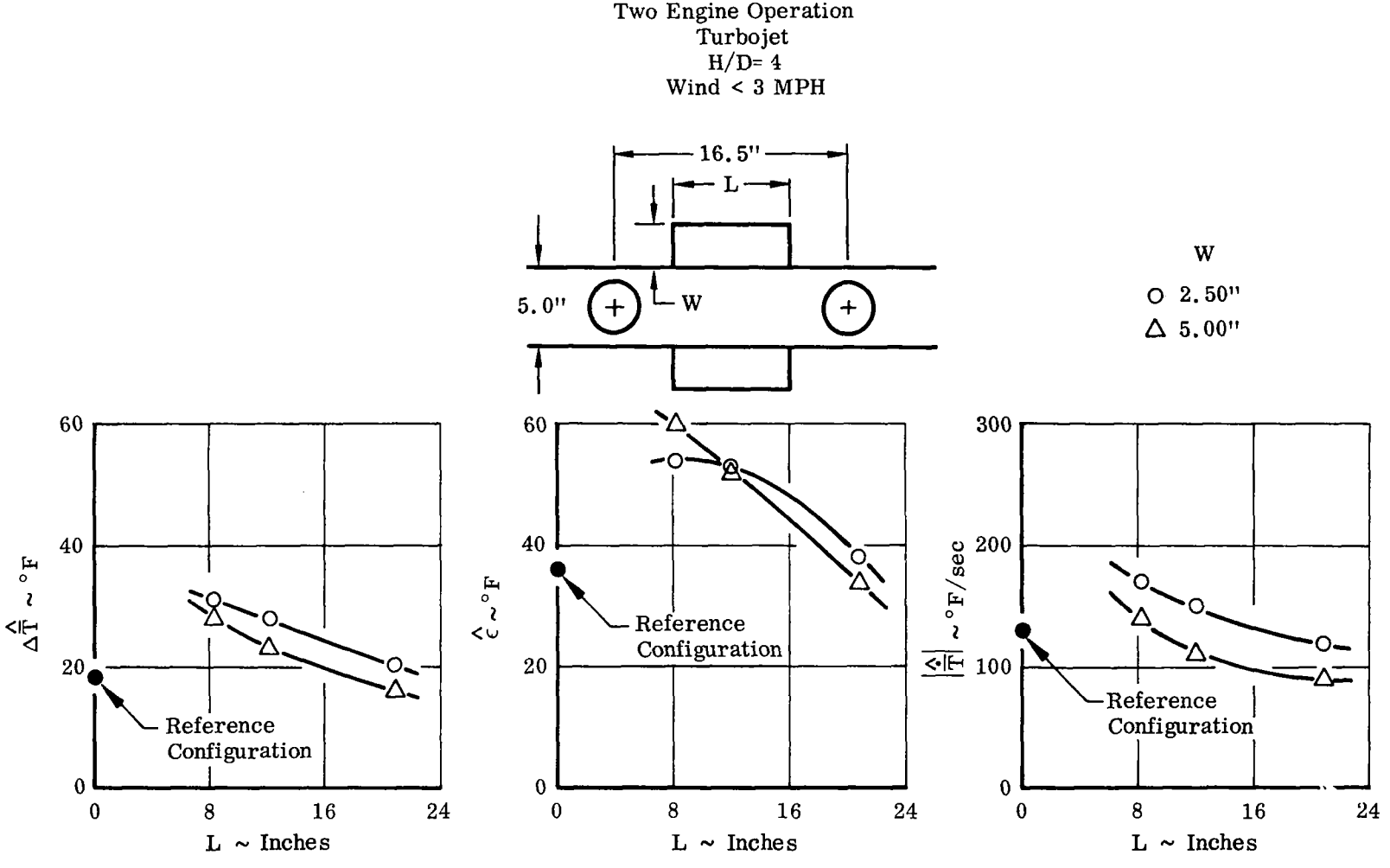

(b) Inlet Plane Shield

FIGURE 29 (cont'd). EFFECT OF SHIELD SIZE AND LOCATION

FIGURE 30. EXIT PLANE SHIELD (L = 5.0", W = 1.25")

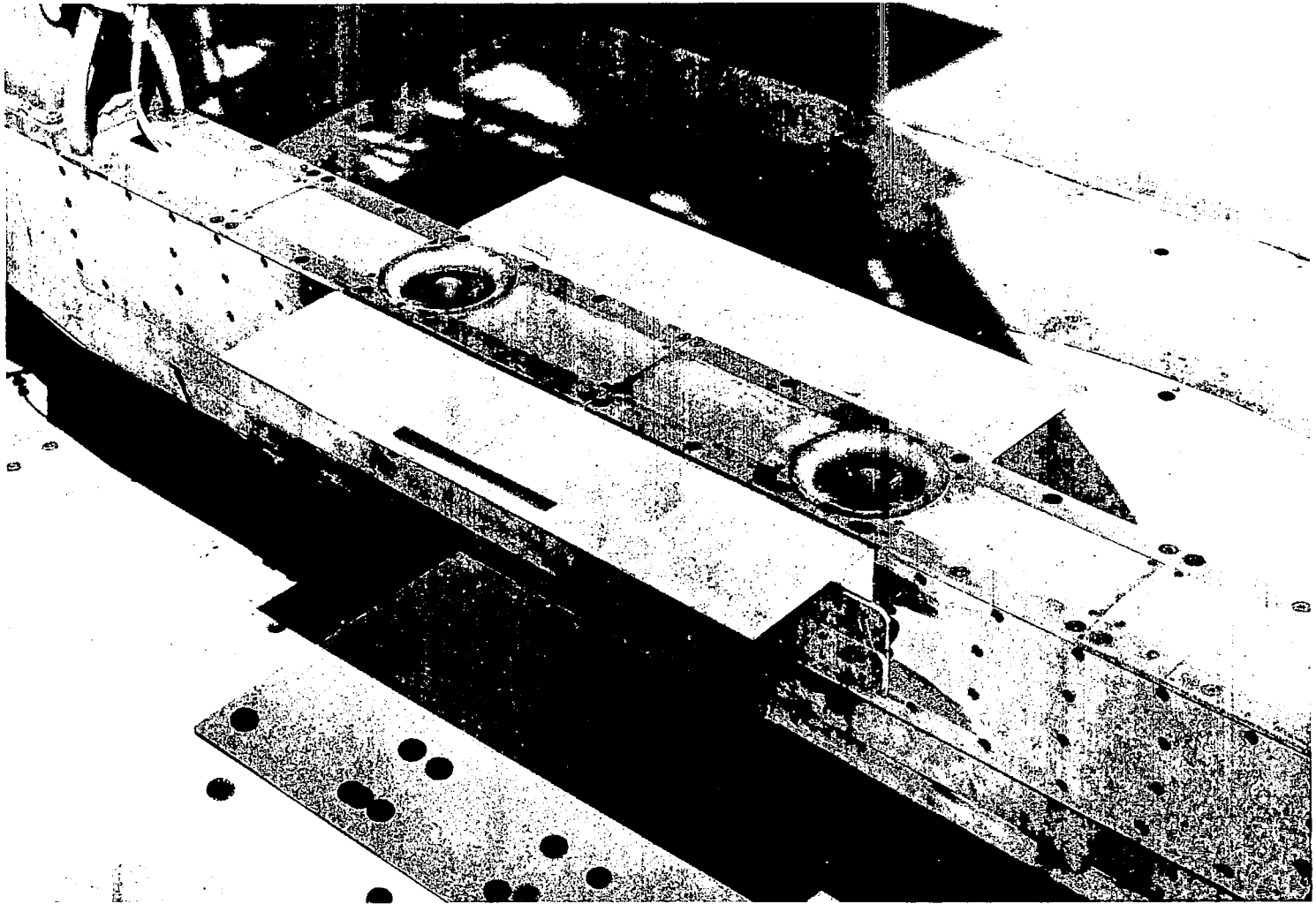

FIGURE 31. INLET PLANE SHIELD (L = 20.85", W = 5.0")

Two Engine Operation
Turbojet
Wind < 3 MPH

○ Reference Configuration
△ Shield Configuration
(L = 12.15", W = 2.5")

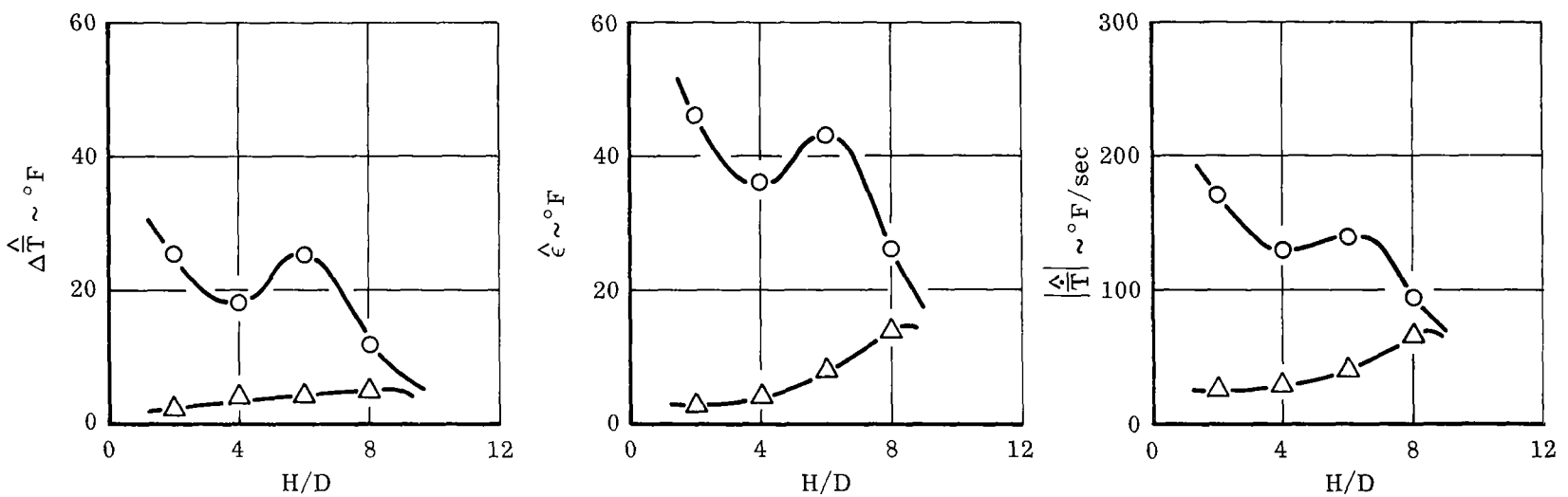

FIGURE 32. EFFECT OF H/D ON SHIELD EFFECTIVENESS

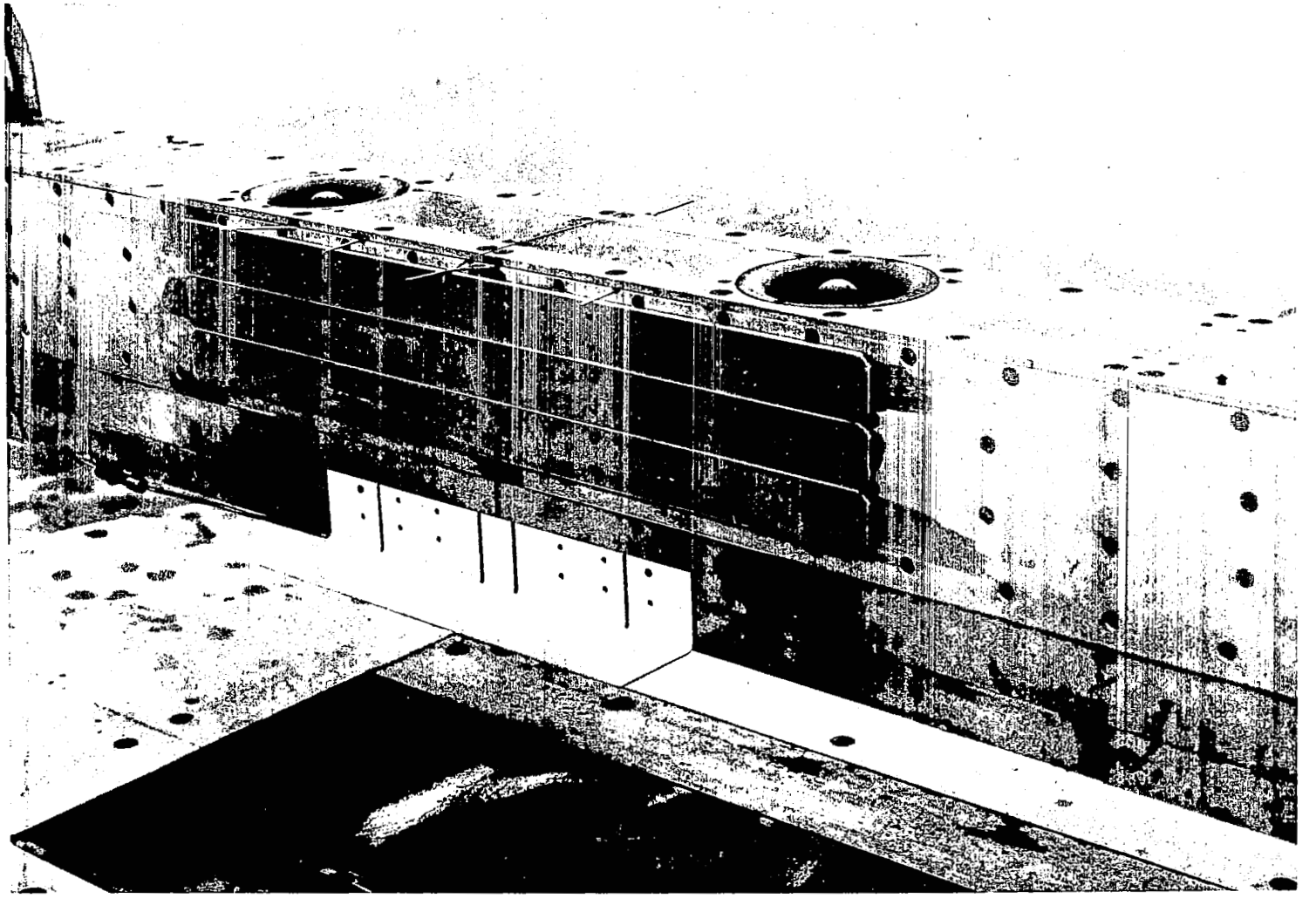

FIGURE 33. EXIT PLANE SHIELD (L = 12.15", W = 2.5")

Two Engine Operation
Turbojet
H/D = 4

O Reference Configuration

△ Shield Configuration
(L = 12.15", W = 2.5")

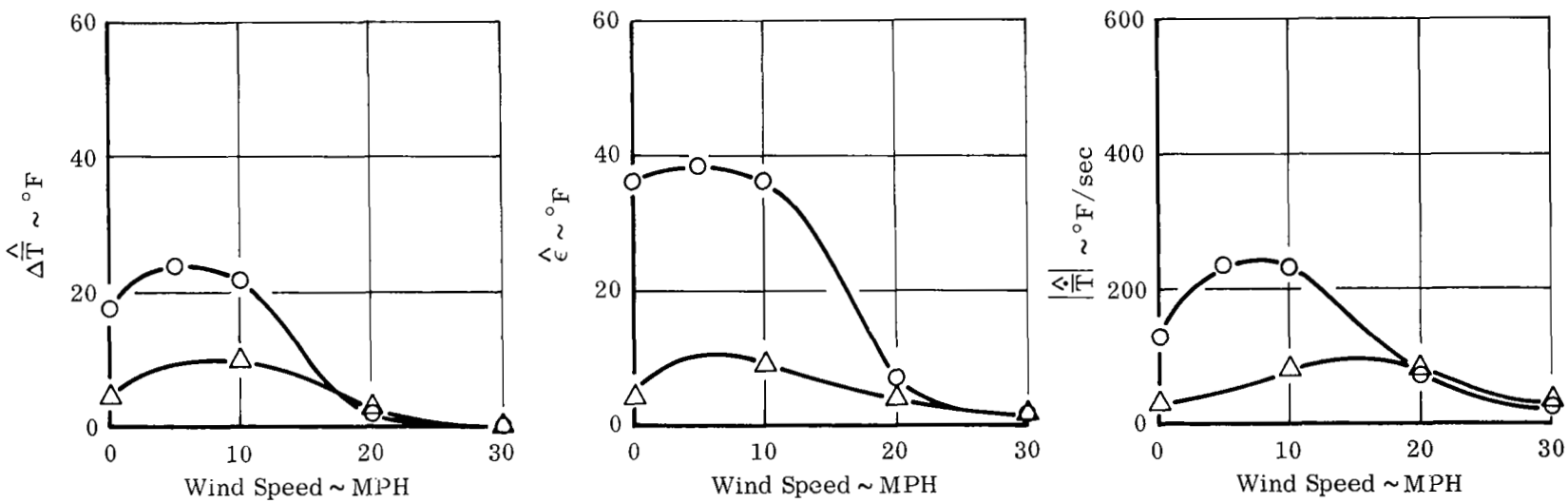

(a) Headwind

FIGURE 34. EFFECT OF WIND ON SHIELD EFFECTIVENESS

Two Engine Operation
Turbojet
H/D=4

○ Reference Configuration

△ Shield Configuration
(L = 12.15", W = 2.5")

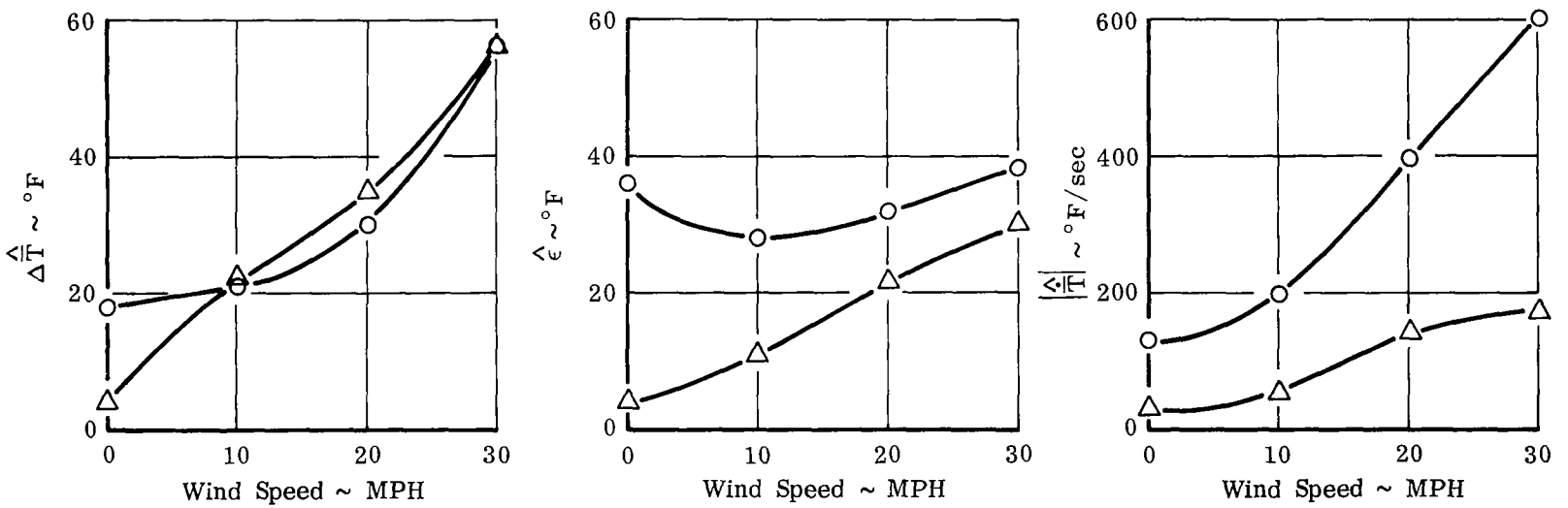

(b) Crosswind

FIGURE 34 (cont'd). EFFECT OF WIND ON SHIELD EFFECTIVENESS

Two Engine Operation
Turbojet
H/D = 4
Wind = 20 MPH Crosswind

AFT INLET

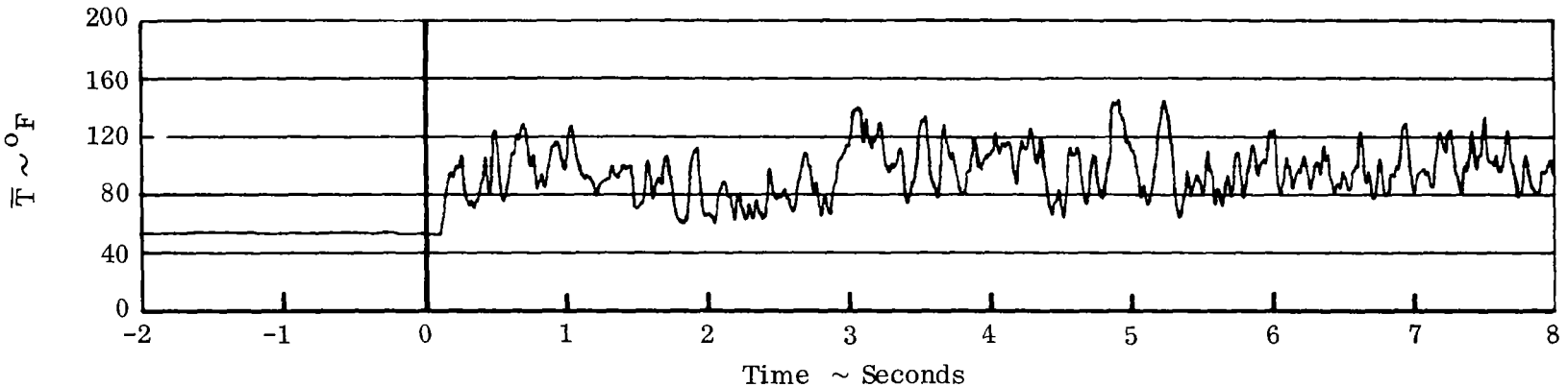

(a) Reference Configuration

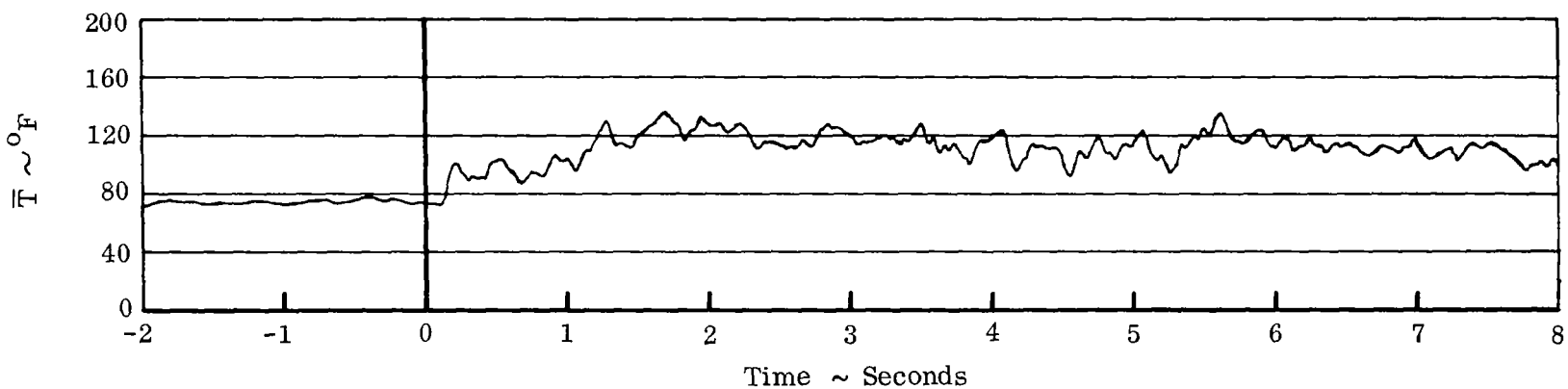

(b) Shield Configuration (L = 12.15", W = 2.5")

FIGURE 35. INGESTION CHARACTERISTICS HISTORY - CROSSWIND

Two Engine Operation
H/D = 4
Wind < 3 MPH

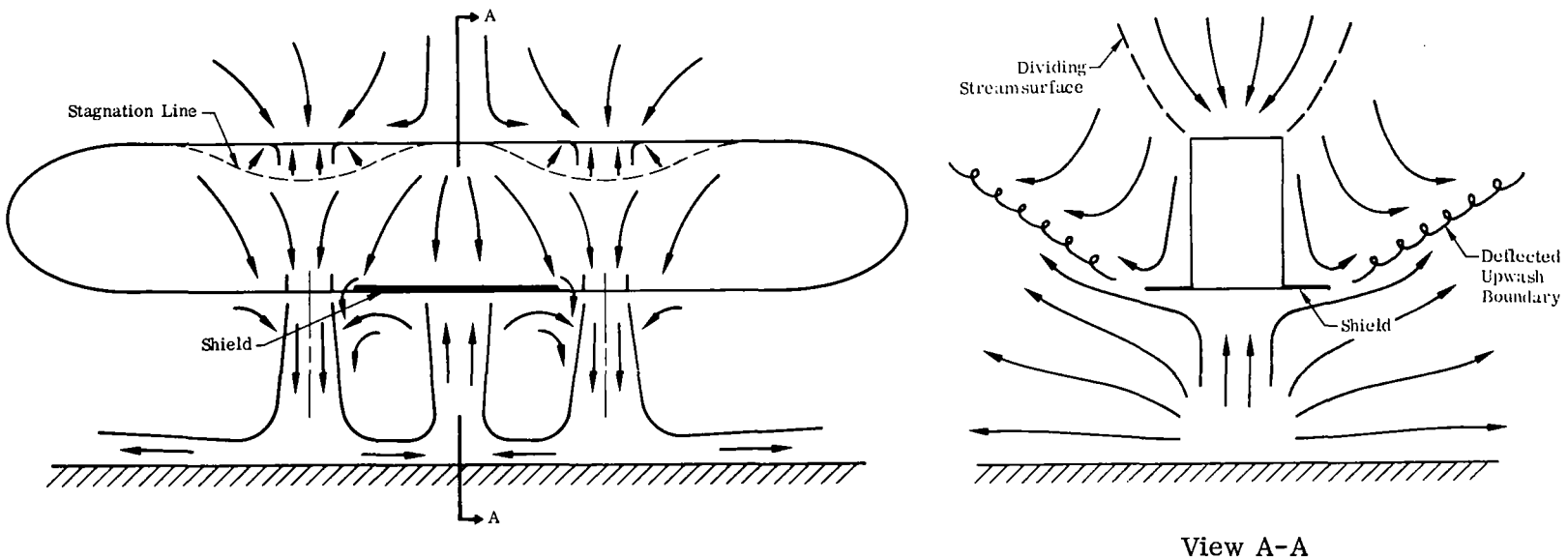

View A-A

FIGURE 36. FLOW FIELD SCHEMATIC - EXIT PLANE SHIELD
(L = 12.15", W = 2.5")

Two Engine Operation
H/D = 4
Wind < 3 MPH

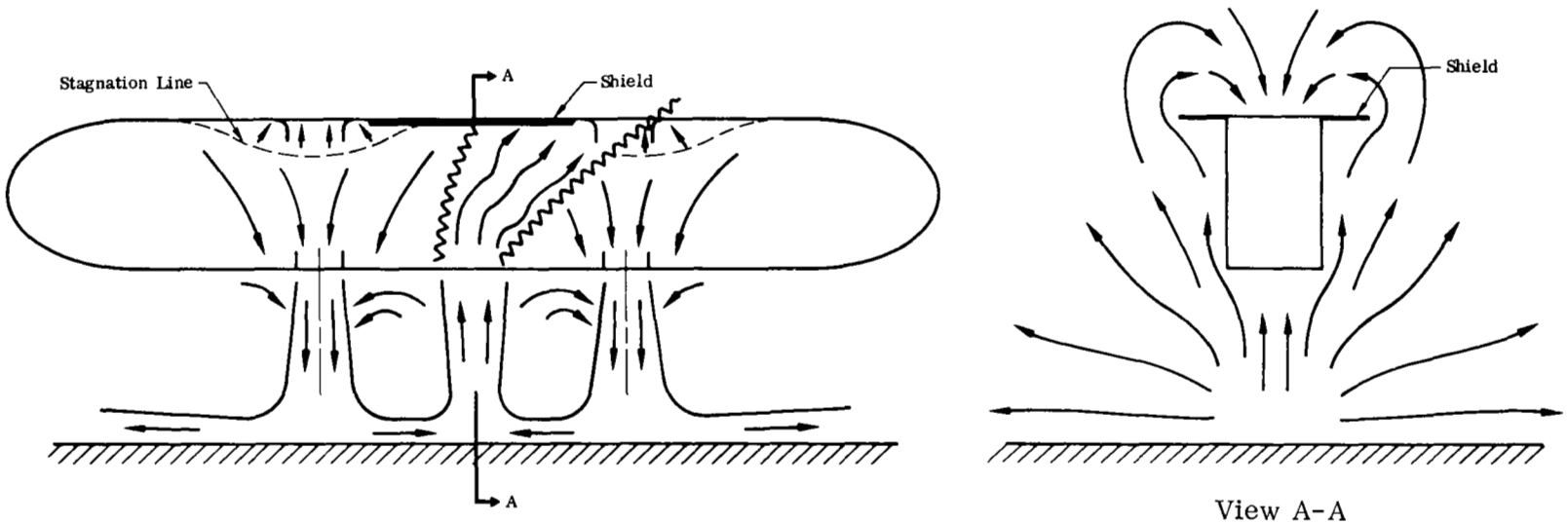

FIGURE 37. FLOW FIELD SCHEMATIC - INLET PLANE SHIELD
(L = 12.15", W = 2.5")

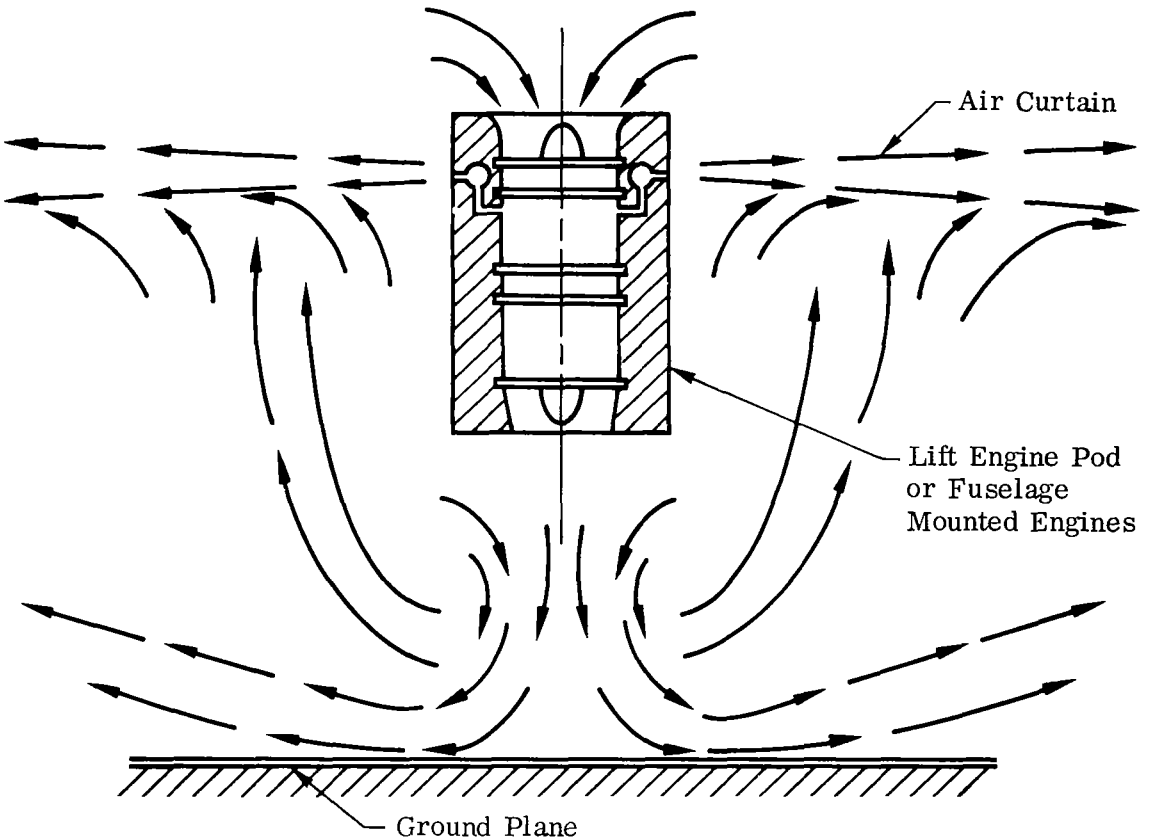

FIGURE 38. AIR CURTAIN CONCEPT

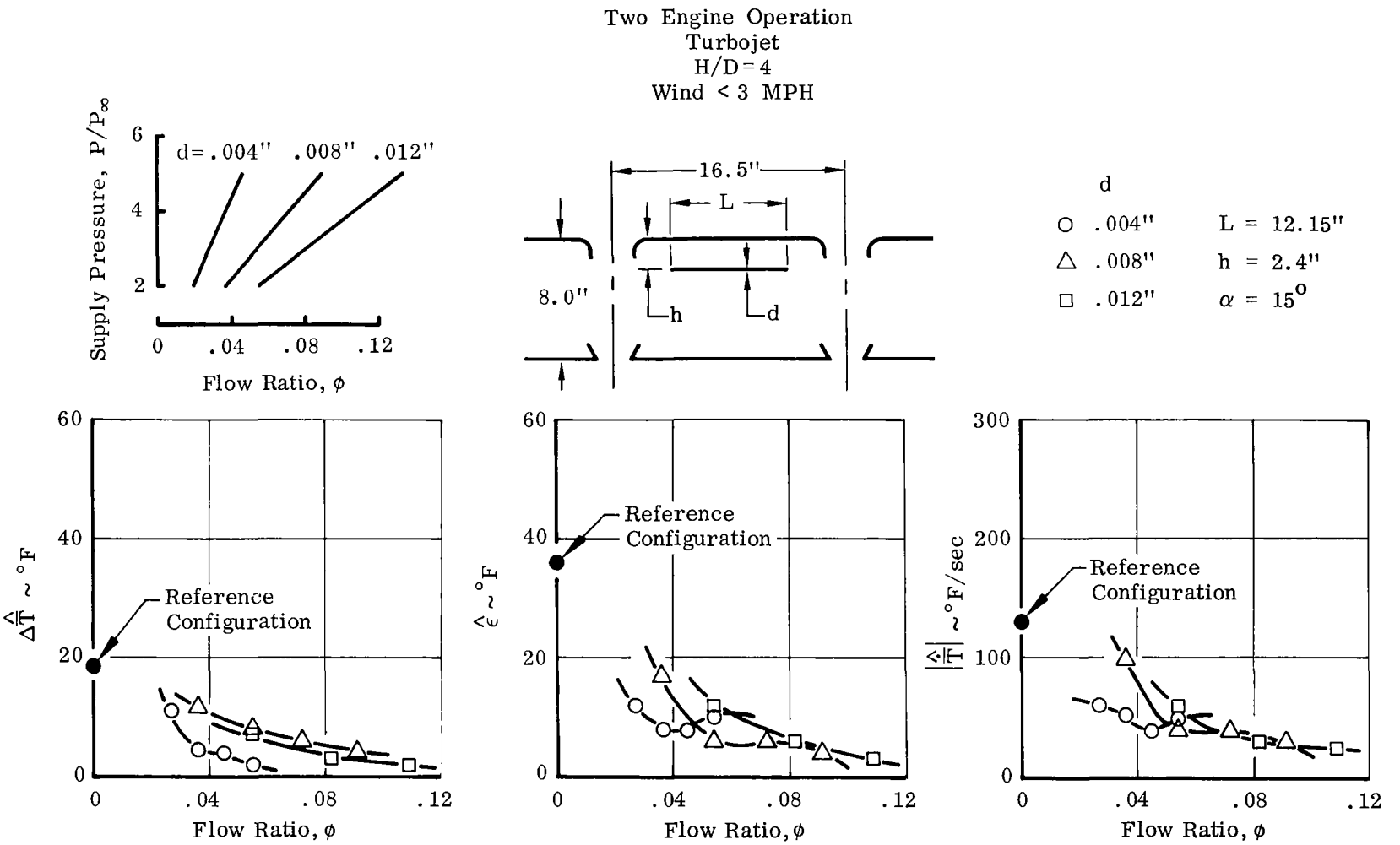

(a) Effect of Slot Width

FIGURE 39. EFFECT OF AIR CURTAIN DESIGN VARIABLES

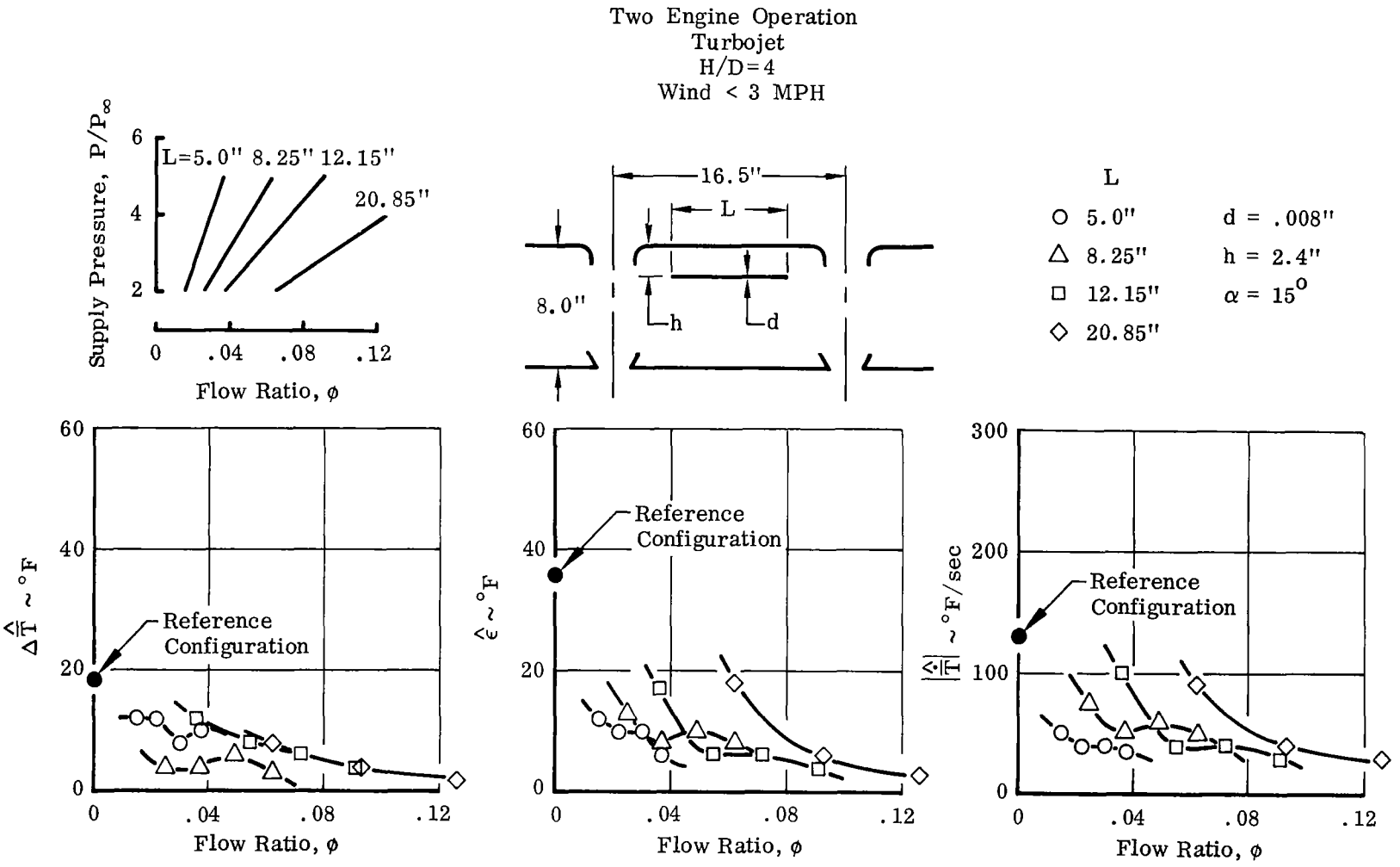

(b) Effect of Slot Length

FIGURE 39 (cont'd). EFFECT OF AIR CURTAIN DESIGN VARIABLES

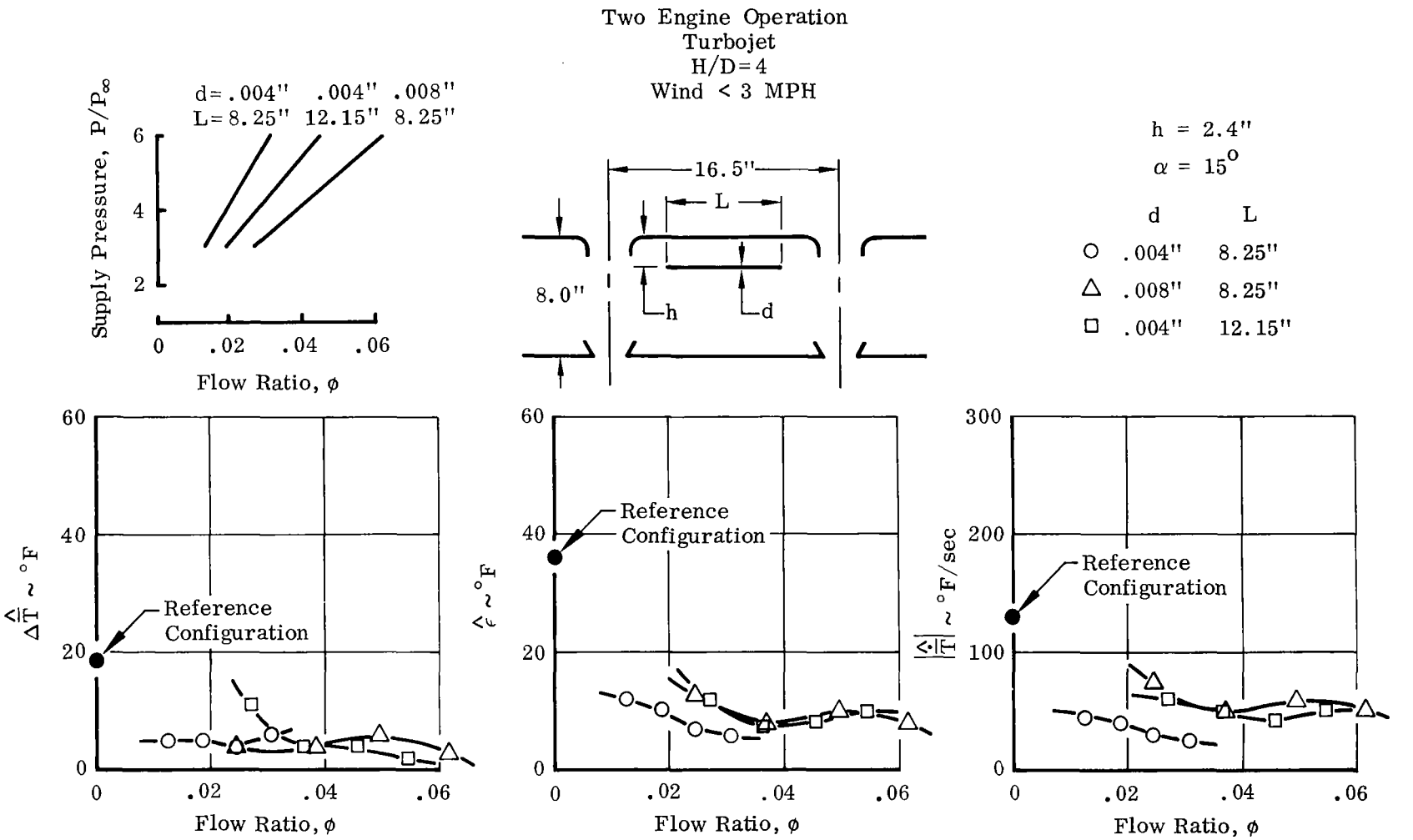

(c) Effect of Slot Width and Length

FIGURE 39 (cont'd). EFFECT OF AIR CURTAIN DESIGN VARIABLES

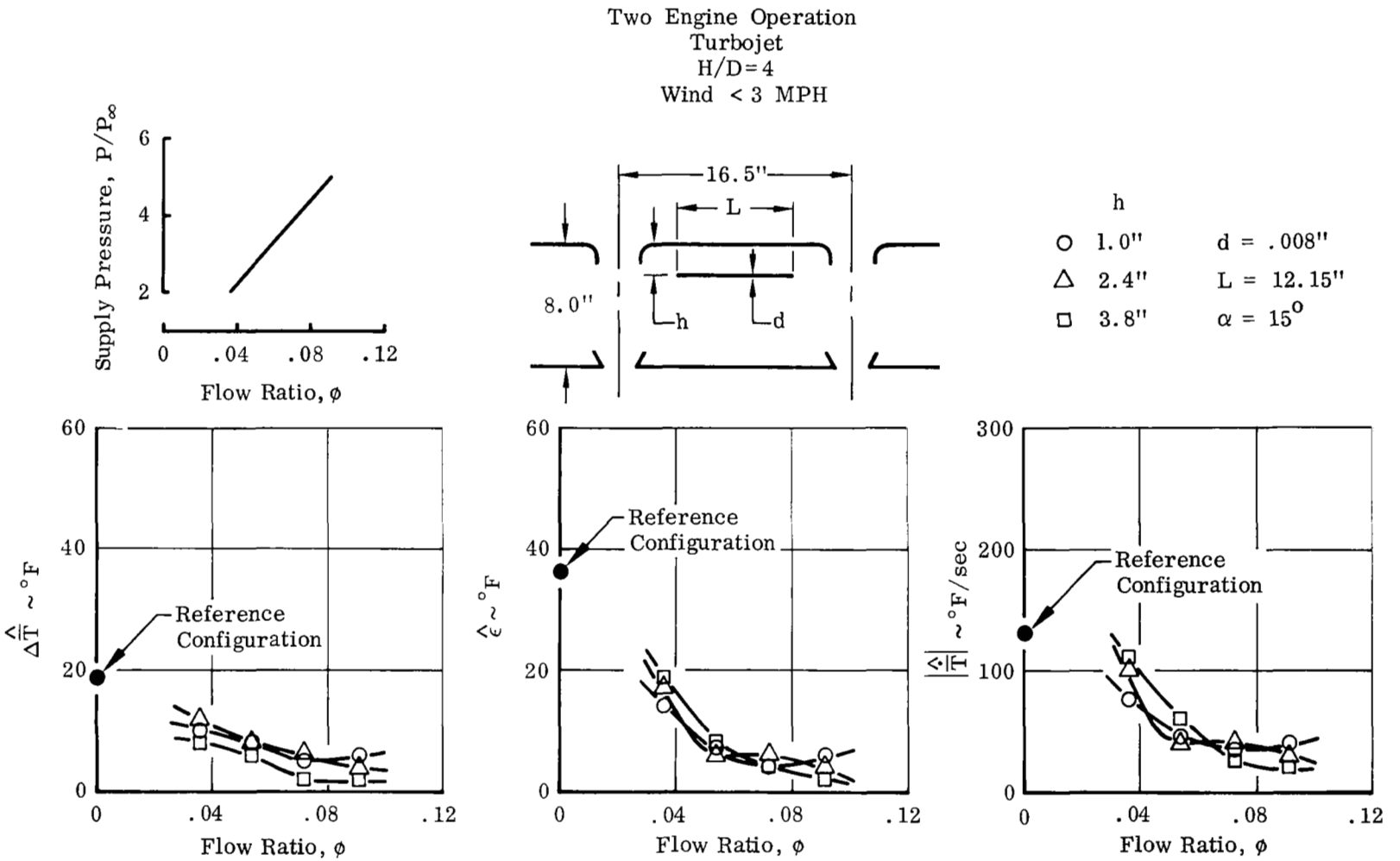

(d) Effect of Slot Location

FIGURE 39 (cont'd). EFFECT OF AIR CURTAIN DESIGN VARIABLES

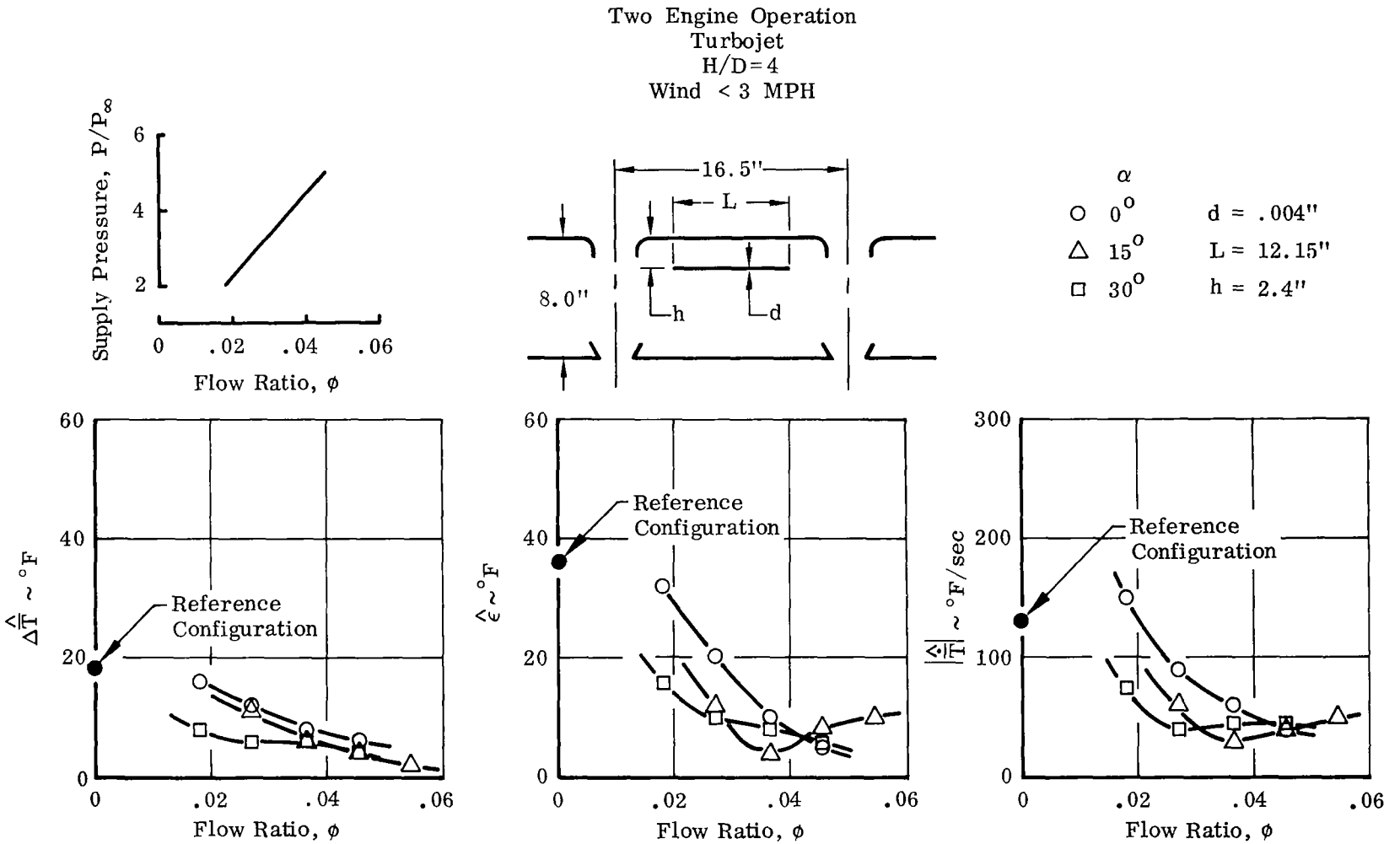

(e) Effect of Slot Angle

FIGURE 39 (cont'd). EFFECT OF AIR CURTAIN DESIGN VARIABLES

Two Engine Operation
Turbojet
Wind < 3 MPH

○ Reference Configuration

△ Air Shield Configuration:
d = .004" h = 2.4"
L = 12.15" $\alpha = 15^{o}$
$P/P_{\infty} = 4$ $\phi = .036$

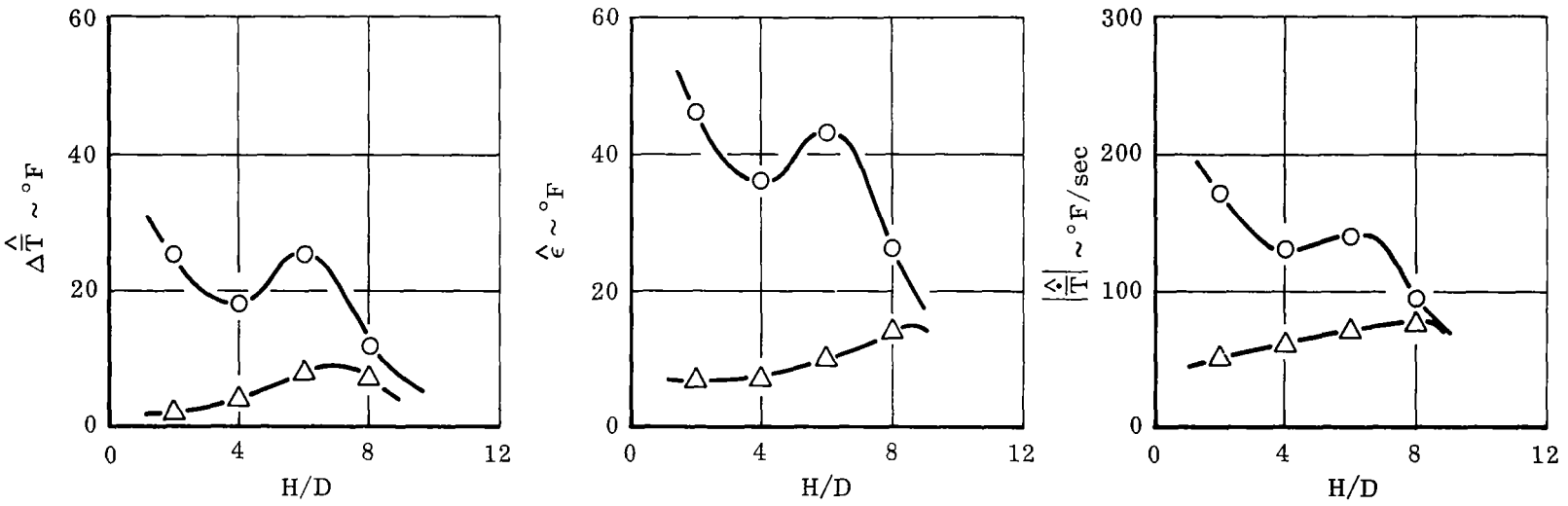

FIGURE 40. EFFECT OF H/D ON AIR CURTAIN EFFECTIVENESS

Two Engine Operation
Turbojet
H/D = 4

○ Reference Configuration

△ Air Shield Configuration:
d = .004" h = 2.4"
L = 12.15" α = 15°
P/P_∞ = 4 ϕ = .036

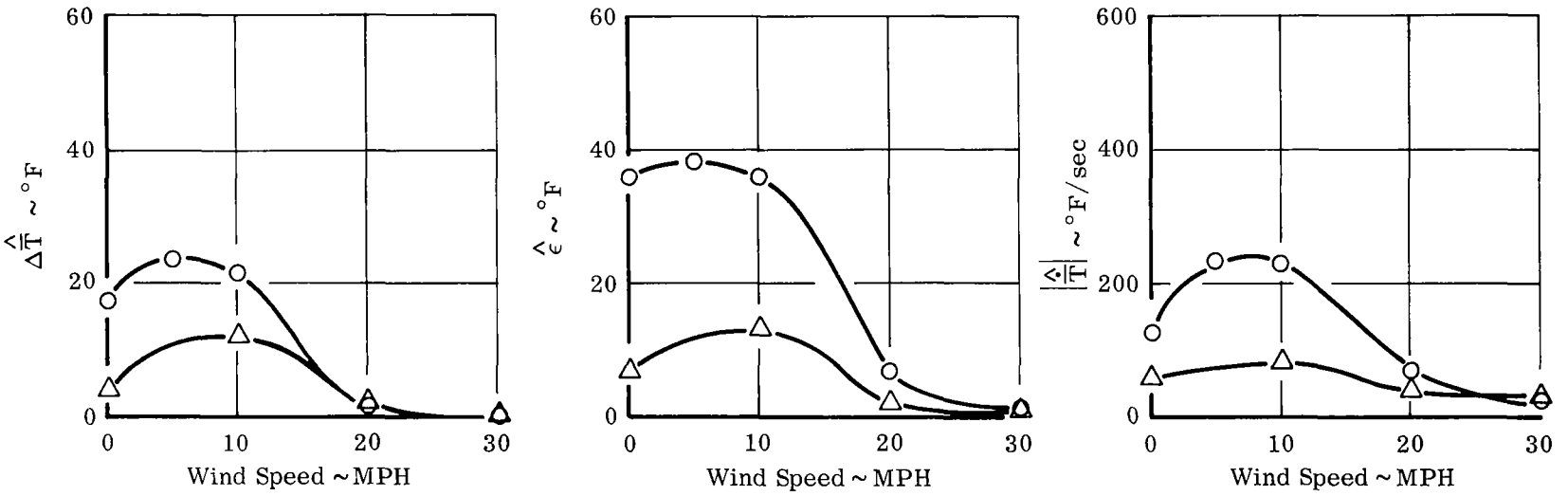

(a) Headwind

FIGURE 41. EFFECT OF WIND ON AIR CURTAIN EFFECTIVENESS

Two Engine Operation
Turbojet
H/D=4

○ Reference Configuration

△ Air Shield Configuration:

d = .004" h = 2.4"

L = 12.15" α = 15°

P/P_∞ = 4 ϕ = .036

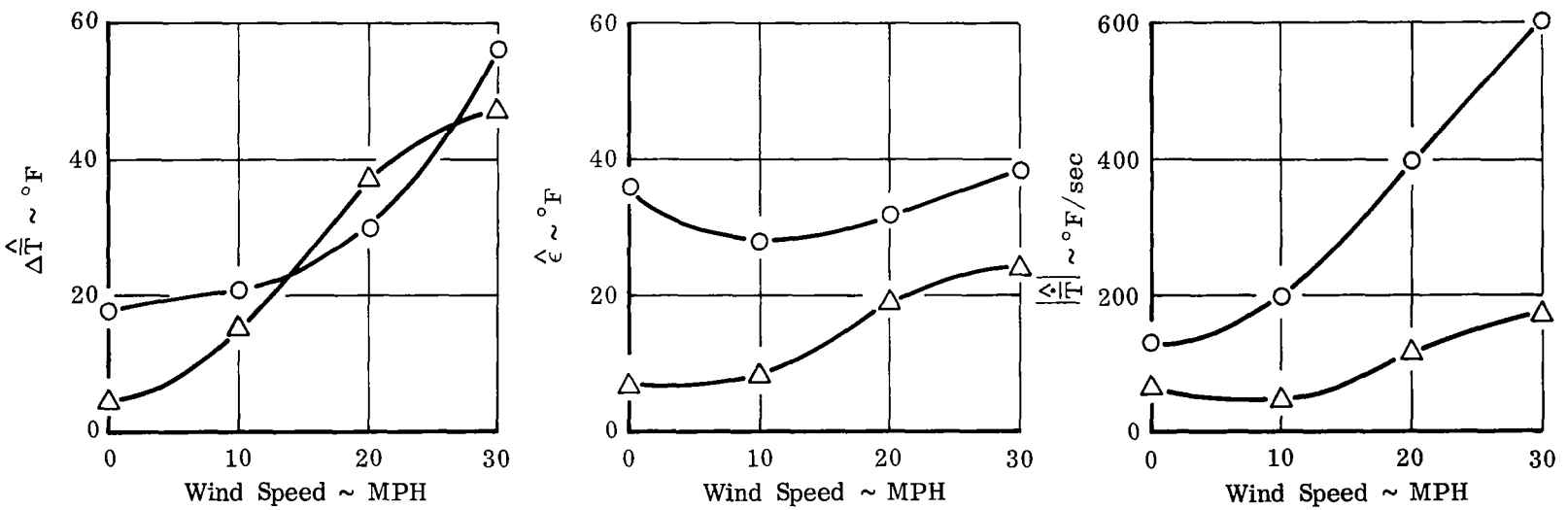

(b) Crosswind

FIGURE 41 (cont'd). EFFECT OF WIND ON AIR CURTAIN EFFECTIVENESS

Two Engine Operation
Turbojet
H/D = 4
Wind = 20 MPH Crosswind

AFT INLET

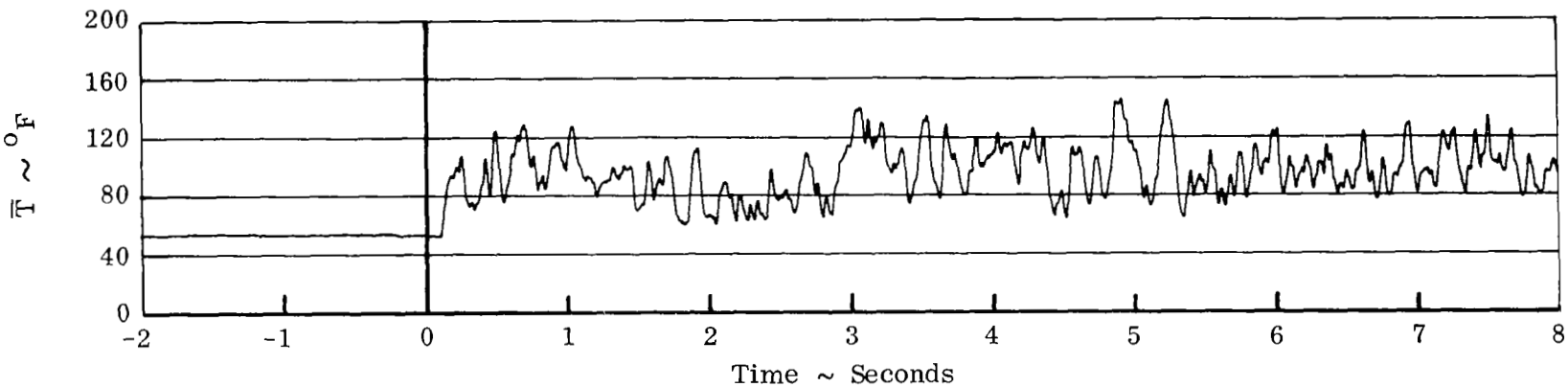

(a) Reference Configuration

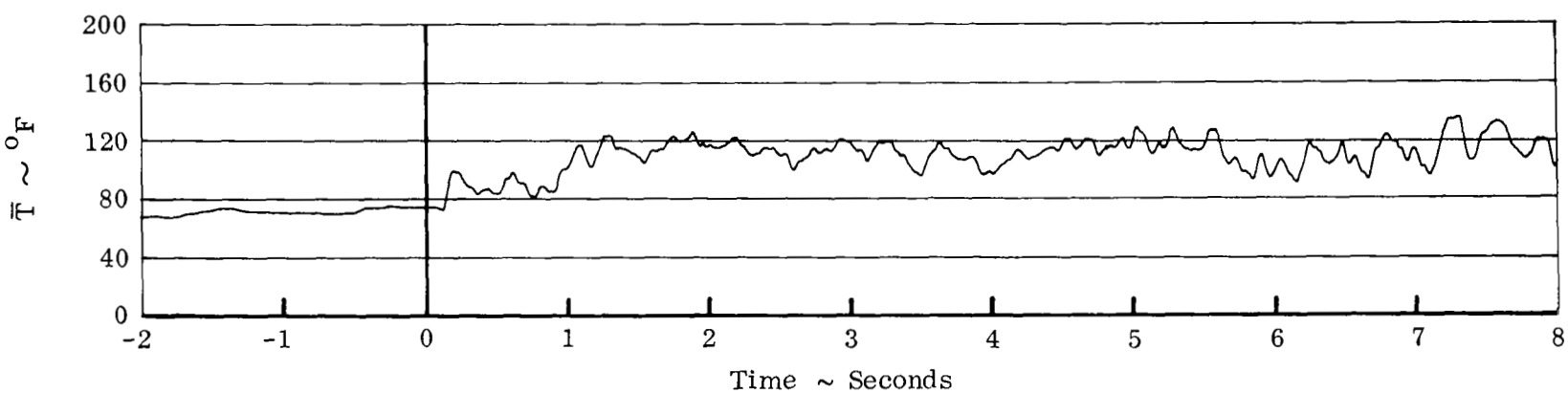

(b) Air Curtain Configuration (d = .004", L = 12.15", h = 2.4", $\alpha = 15^{o}$)

FIGURE 42. INGESTION CHARACTERISTICS HISTORY - CROSSWIND

Two Engine Operation
H/D = 4
Wind < 3 MPH

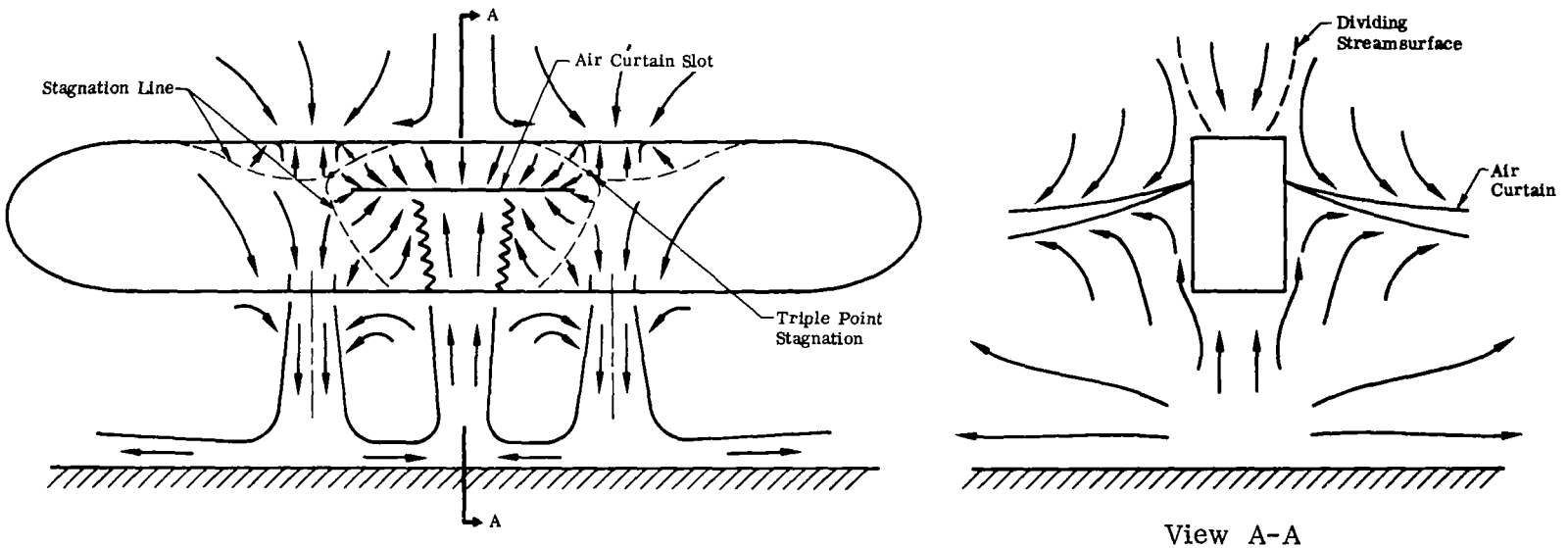

FIGURE 43. FLOW FIELD SCHEMATIC - AIR CURTAIN
(d = .004", L = 12.15", h = 2.4", $\alpha = 15^{o}$)

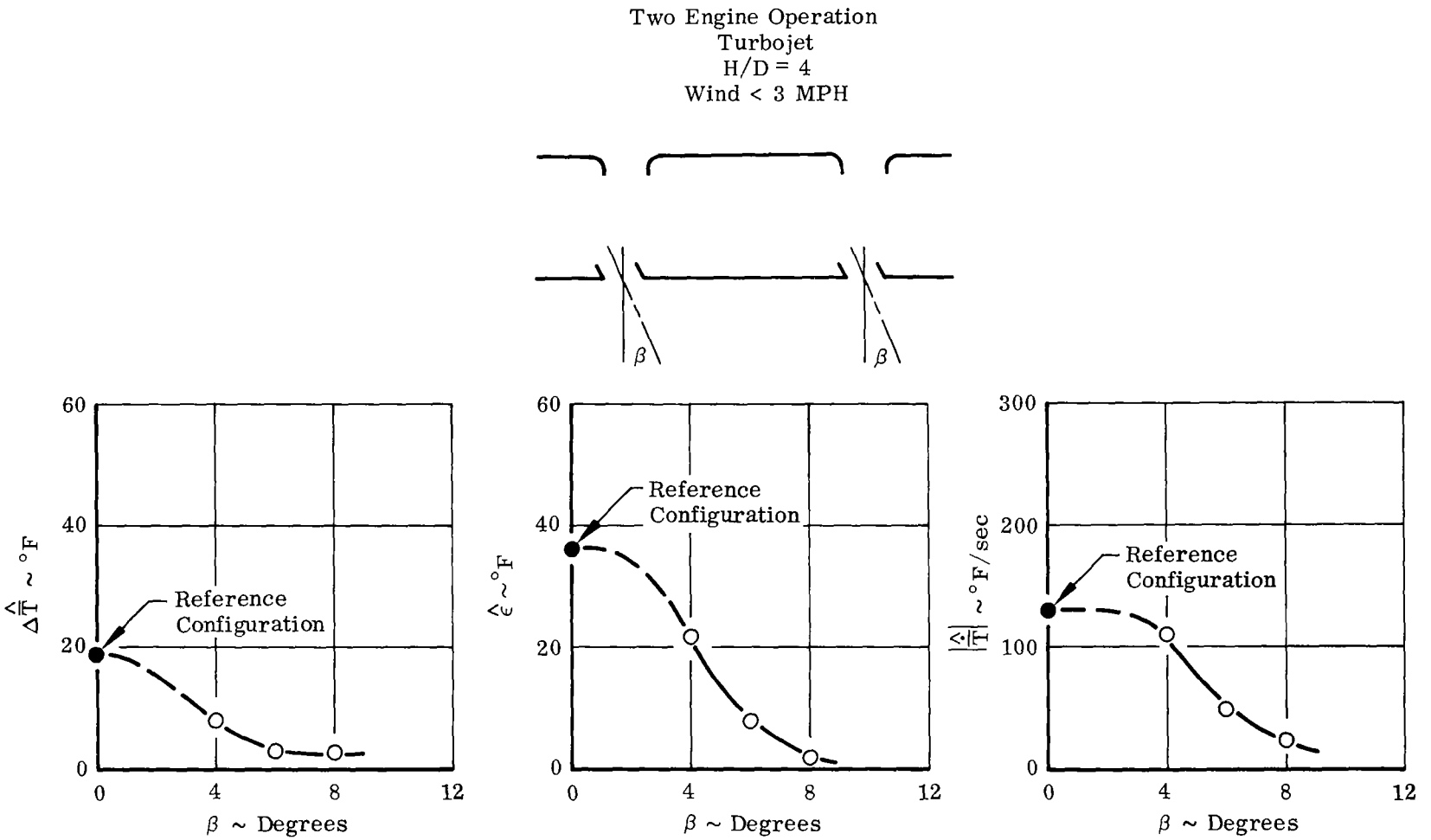

(a) Canted Aft

FIGURE 44. EFFECT OF NOZZLE CANT ANGLE

Two Engine Operation
Turbojet
H/D=4
Wind < 3 MPH

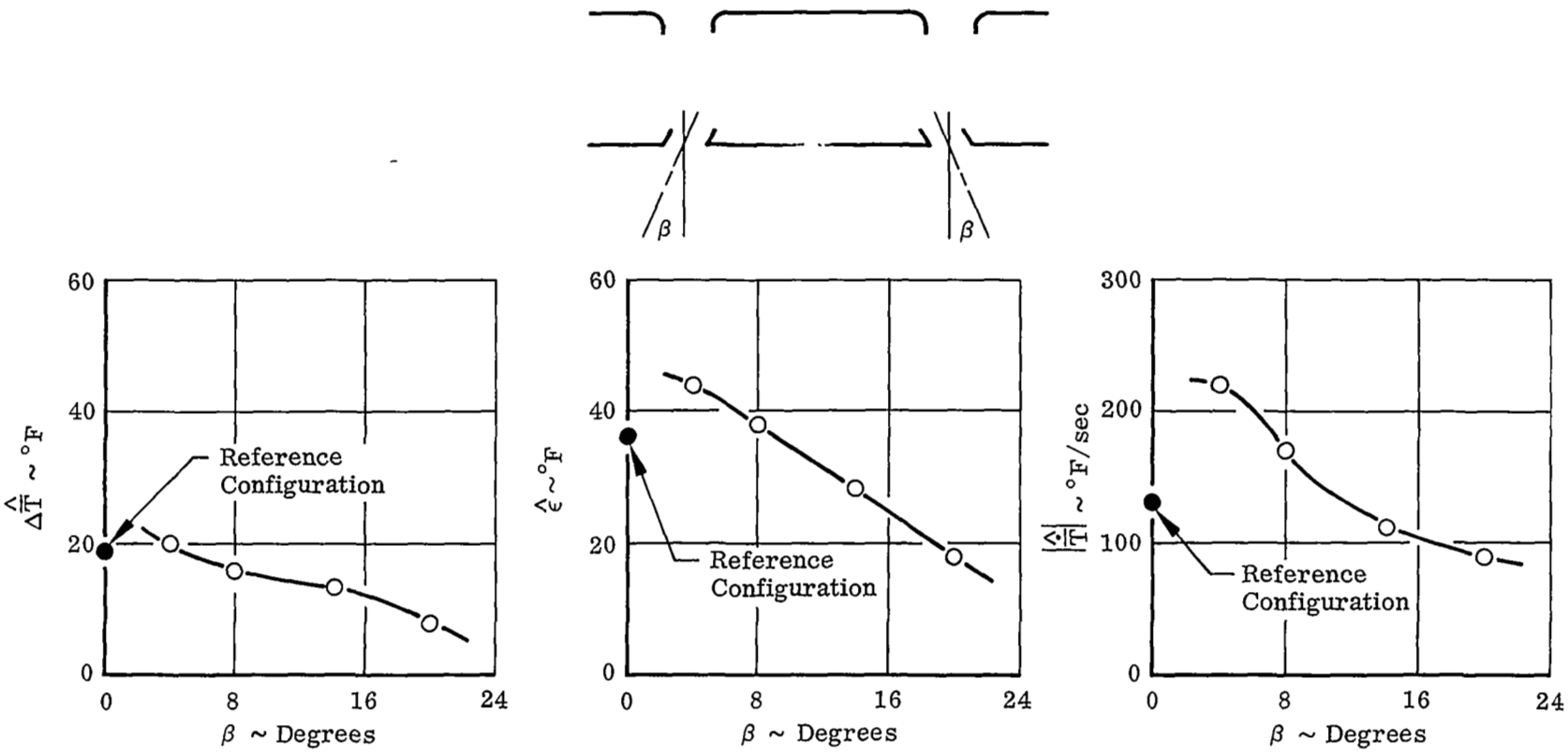

(b) Canted Outward

FIGURE 44 (cont'd). EFFECT OF NOZZLE CANT ANGLE

Two Engine Operation
Turbojet
H/D = 4
Wind < 3 MPH

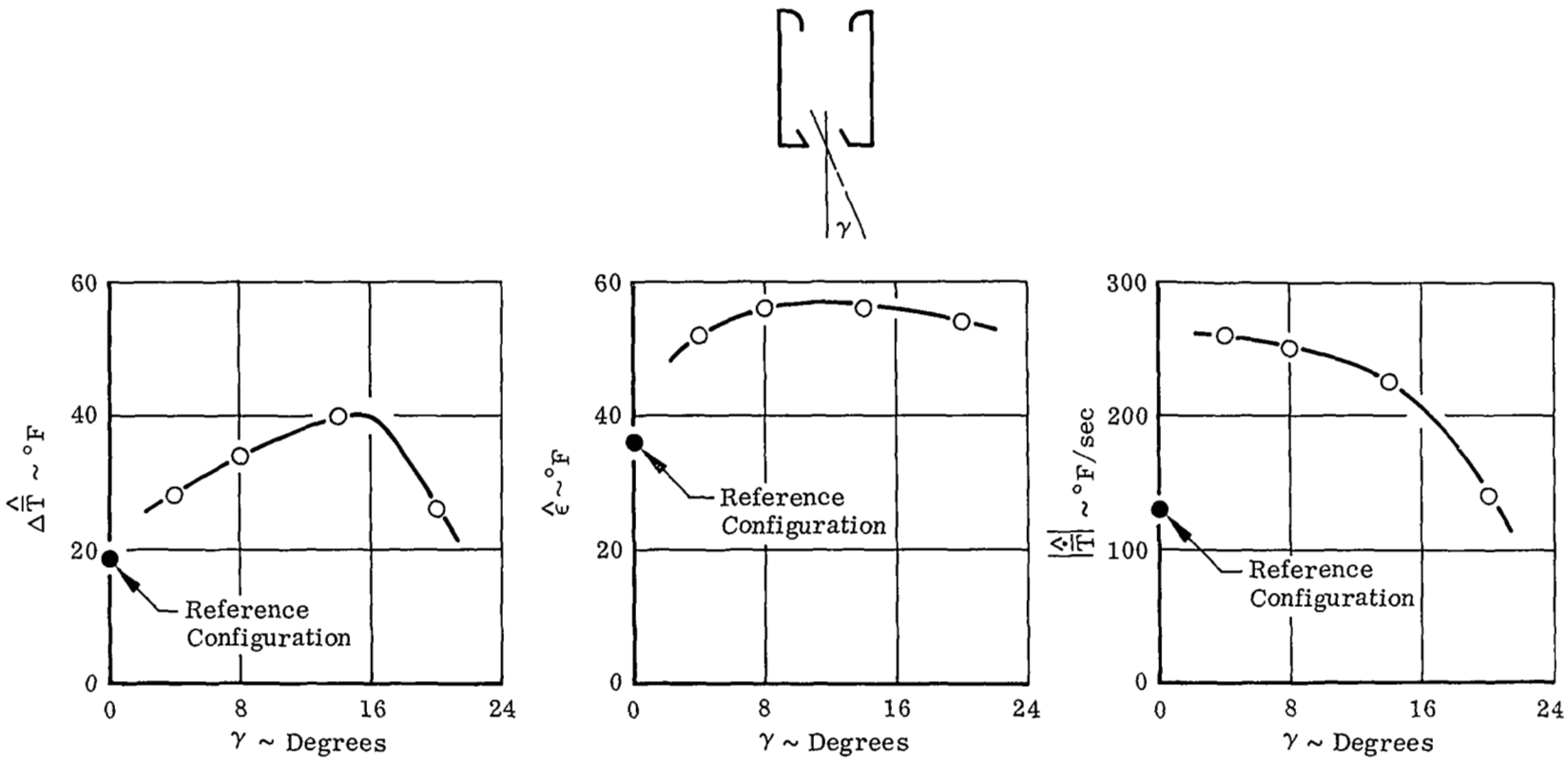

(c) Rolled

FIGURE 44 (cont'd). EFFECT OF NOZZLE CANT ANGLE

Two Engine Operation
Turbojet
Wind < 3 MPH

○ Reference Configuration
△ Nozzles Canted Aft 8°

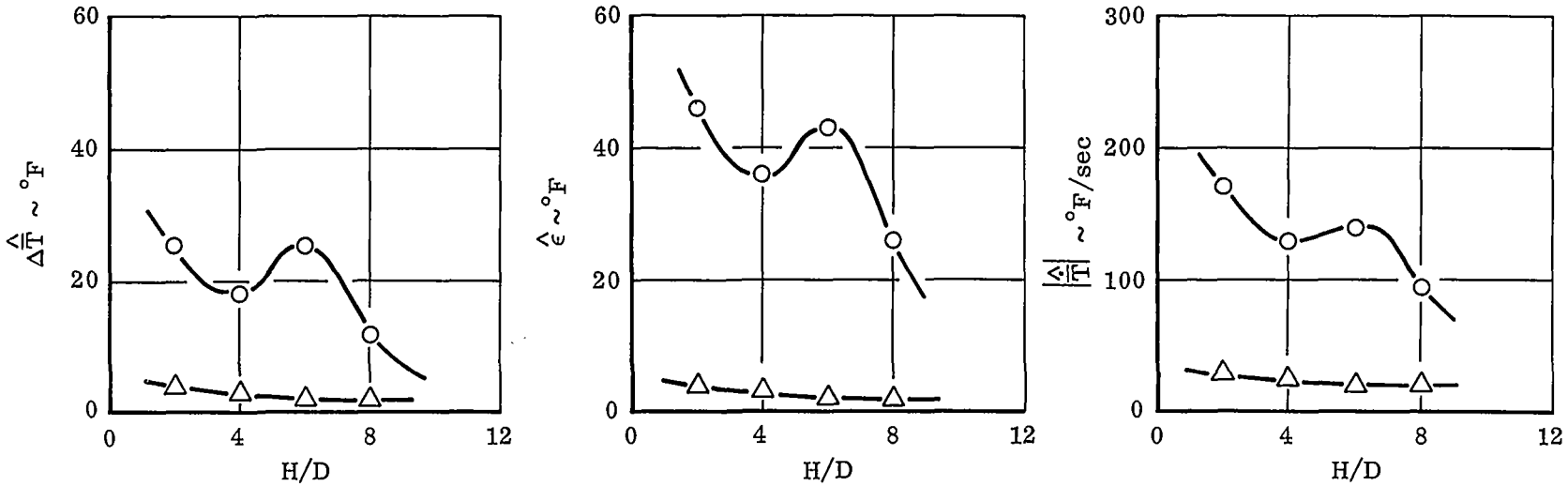

FIGURE 45. EFFECT OF H/D ON NOZZLE CANT EFFECTIVENESS

Two Engine Operation
Turbojet
H/D = 4

O Reference Configuration
△ Nozzles Canted Aft 8°

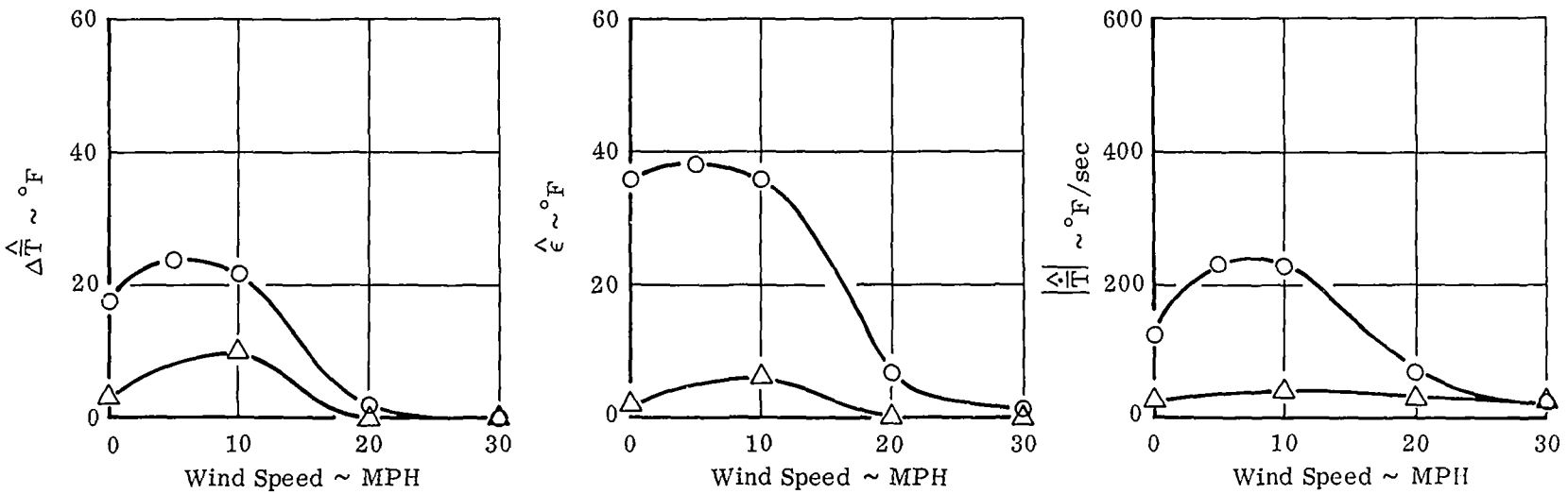

(a) Headwind

FIGURE 46. EFFECT OF WIND ON NOZZLE CANT ANGLE EFFECTIVENESS

Two Engine Operation
Turbojet
H/D = 4

○ Reference Configuration

△ Nozzles Canted Aft 8°

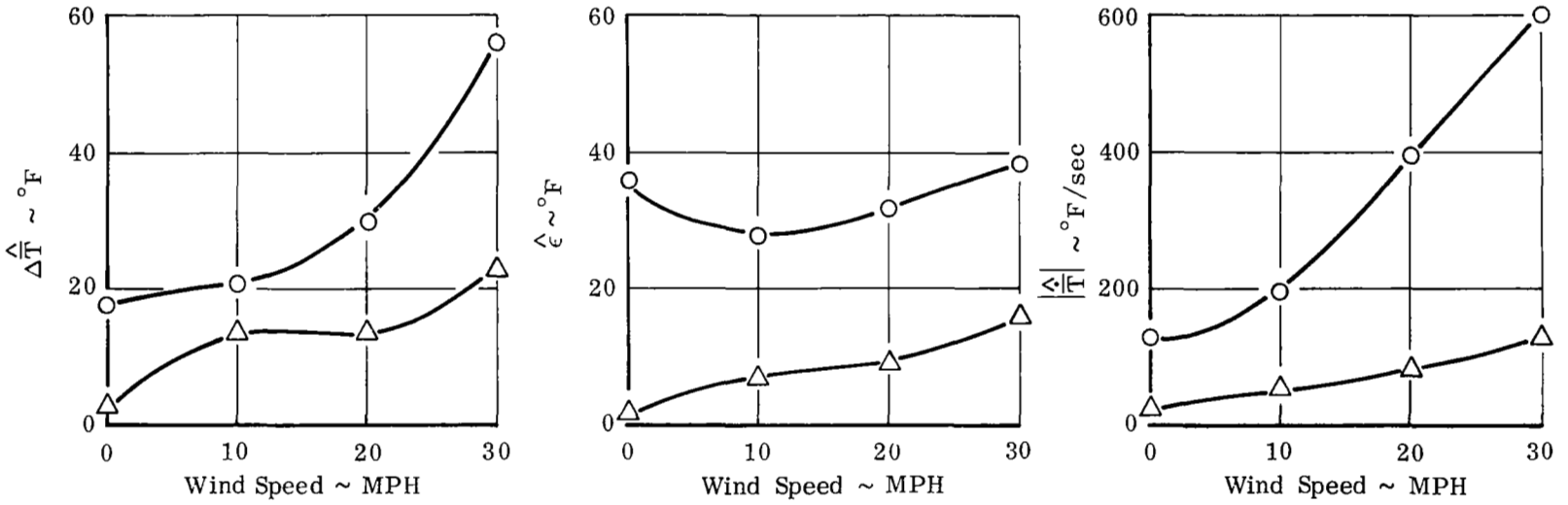

(b) Crosswind

FIGURE 46 (cont'd). EFFECT OF WIND ON NOZZLE CANT ANGLE EFFECTIVENESS

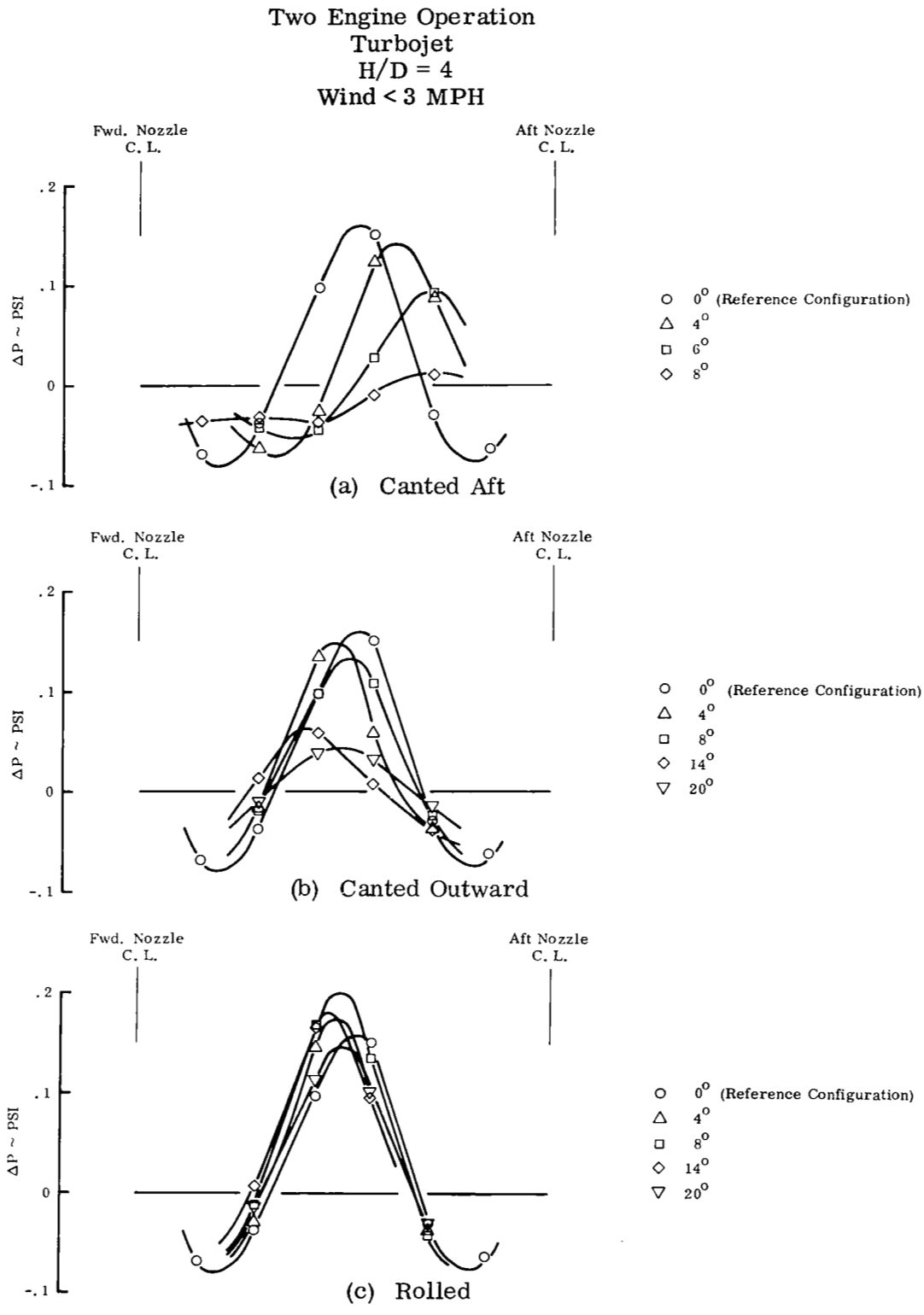

FIGURE 47. EFFECT OF NOZZLE CANT ANGLE ON POD PRESSURE DISTRIBUTION

Two Engine Operation
Turbojet
Wind < 3 MPH

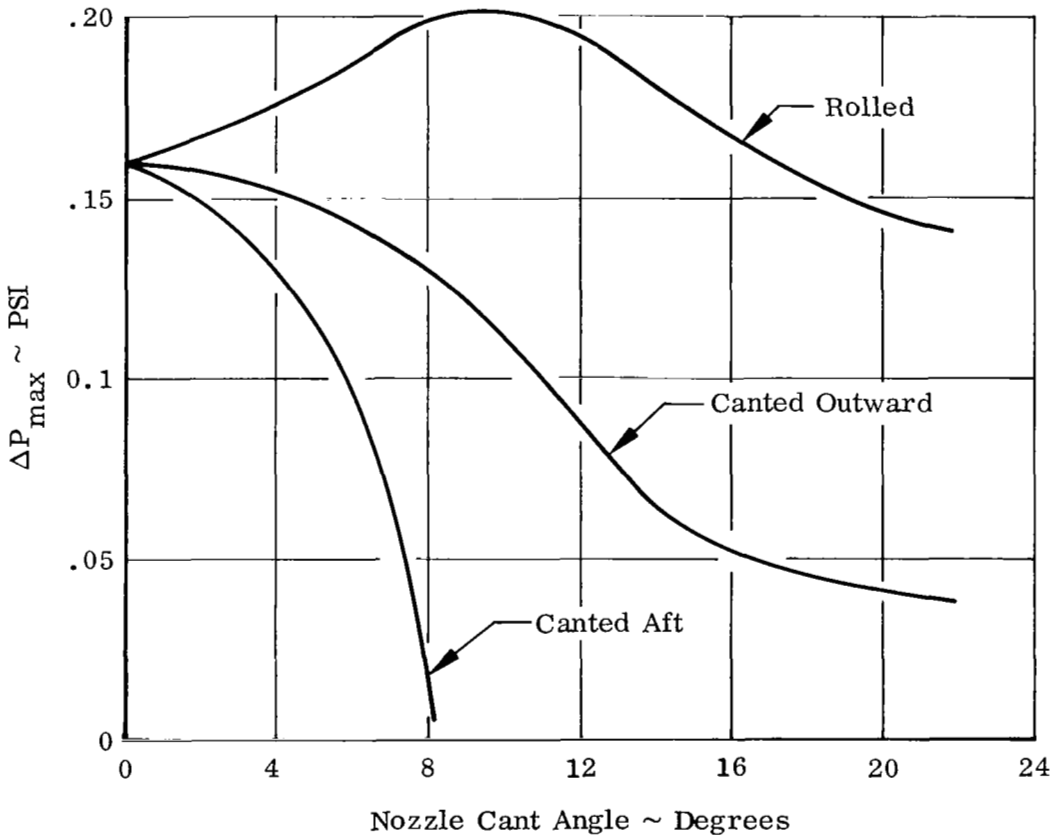

FIGURE 48. EFFECT OF NOZZLE CANT ANGLE ON POD PEAK PRESSURE

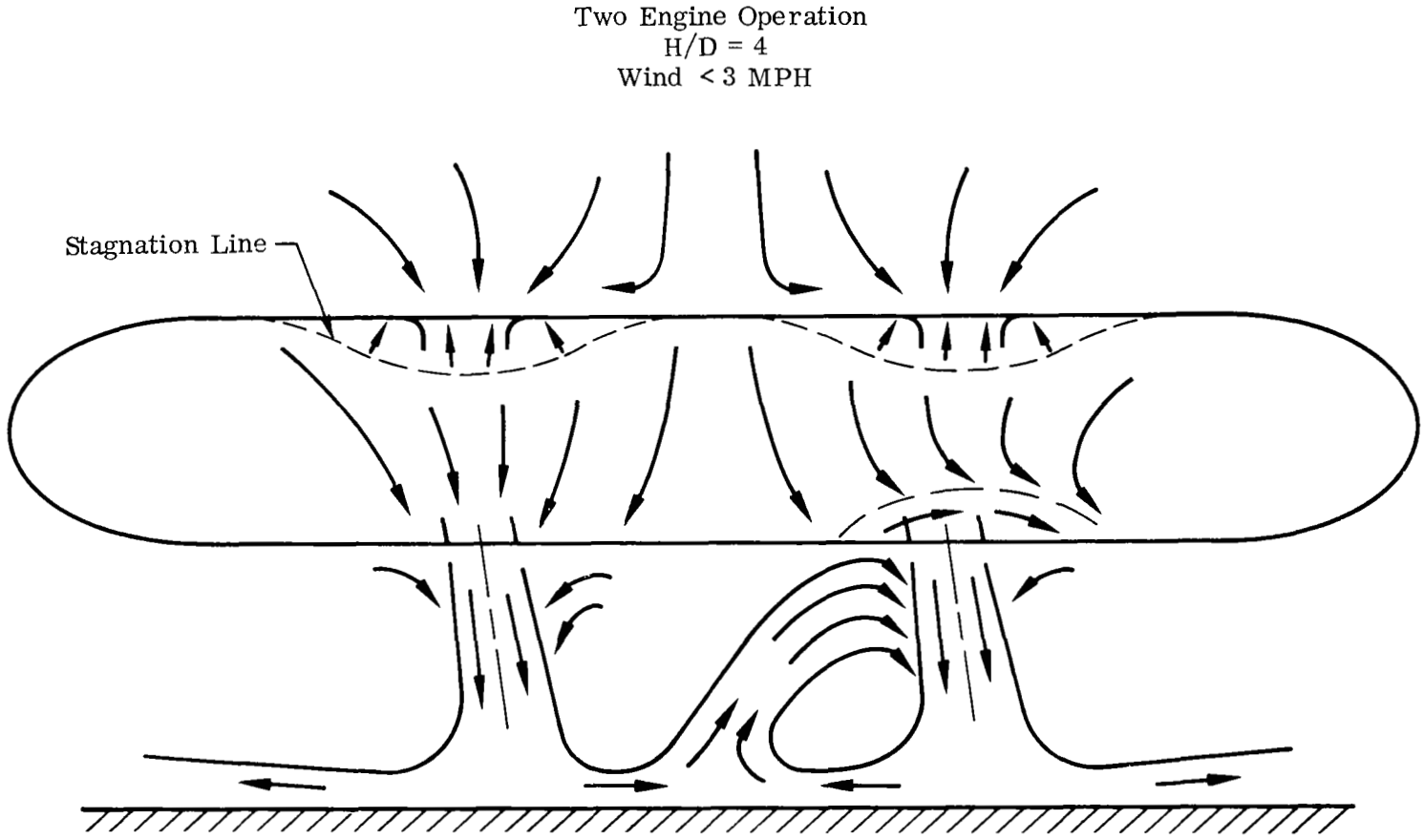

FIGURE 49. FLOW FIELD SCHEMATIC - NOZZLES CANTED AFT 8^{O}

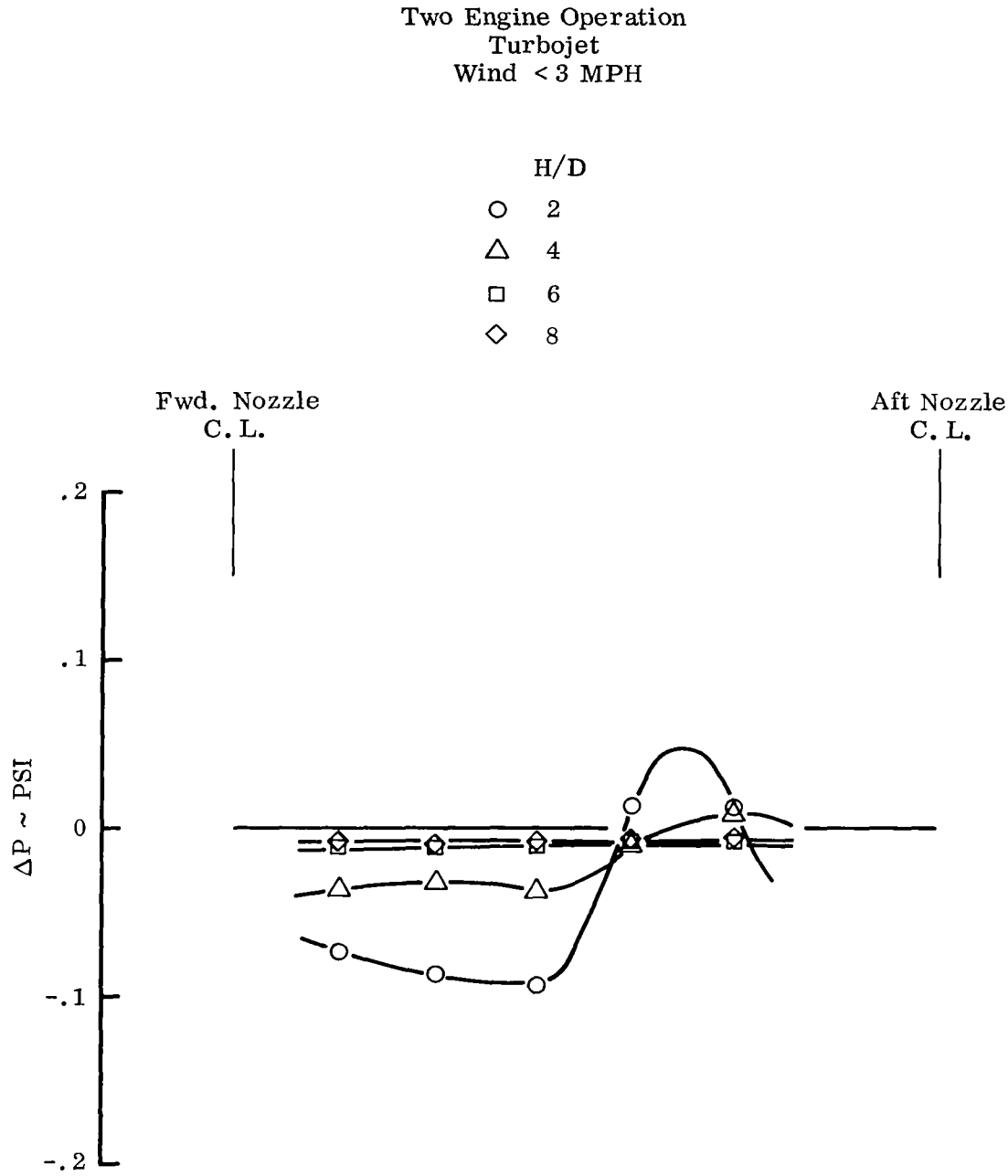

FIGURE 50. EFFECT OF H/D ON POD PRESSURE DISTRIBUTION - NOZZLES CANTED AFT 8°

Two Engine Operation
Turbojet
Wind < 3 MPH

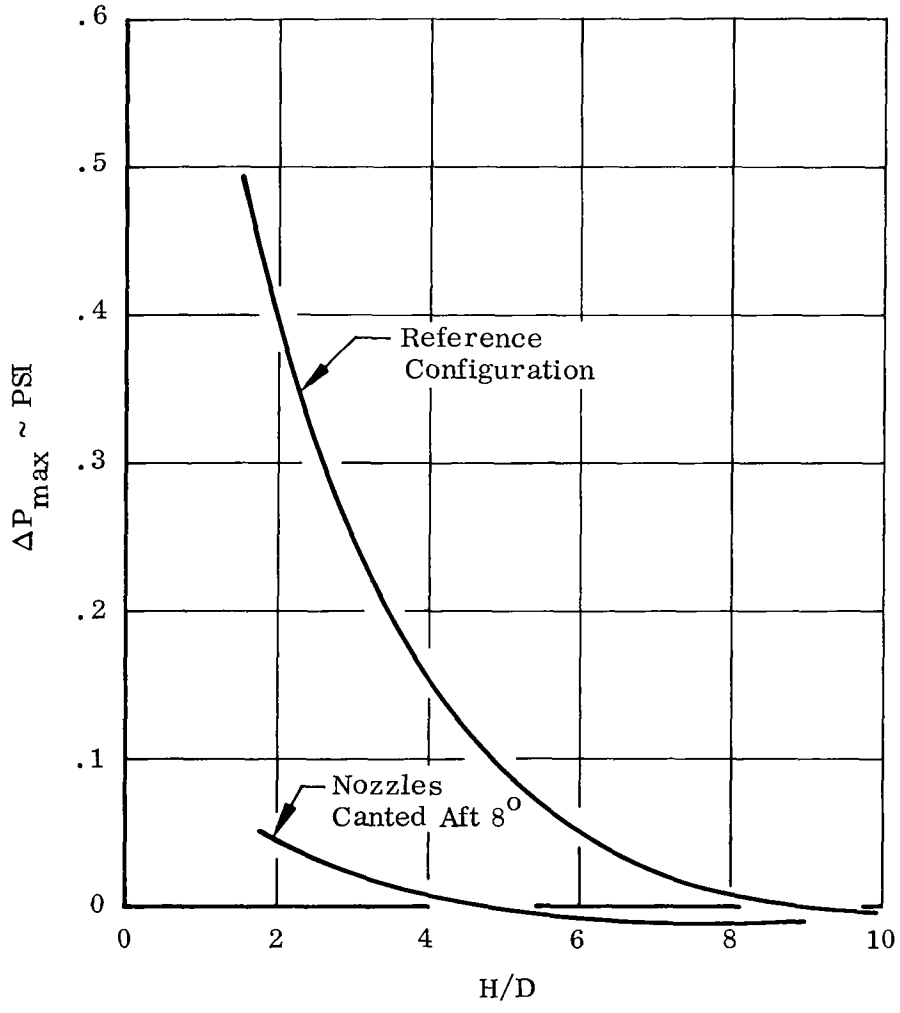

FIGURE 51. EFFECT OF H/D ON POD PRESSURE PEAK

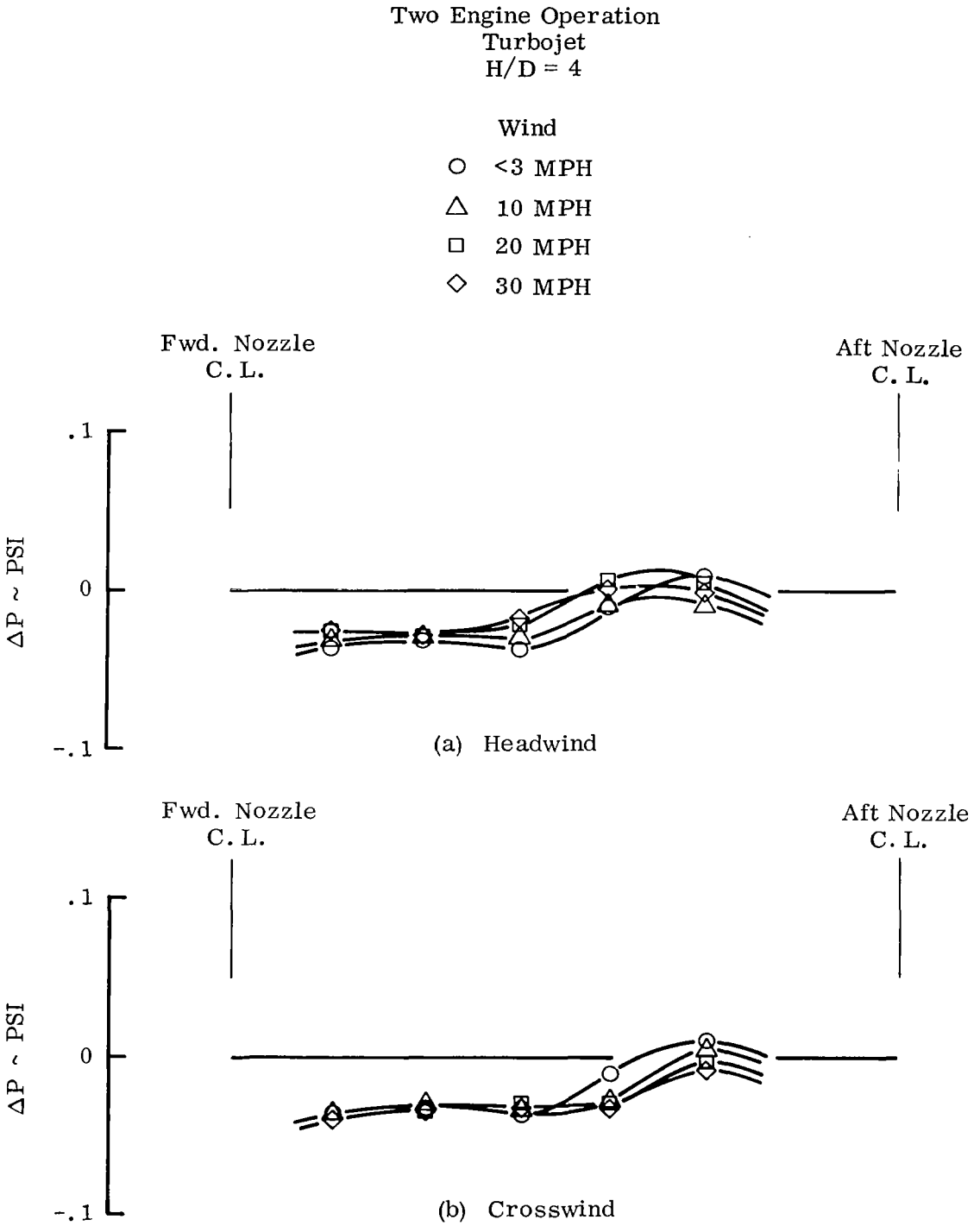

FIGURE 52. EFFECT OF WIND ON POD PRESSURE DISTRIBUTION - NOZZLES CANTED AFT 8°

Two Engine Operation
Turbojet
Wind <3 MPH

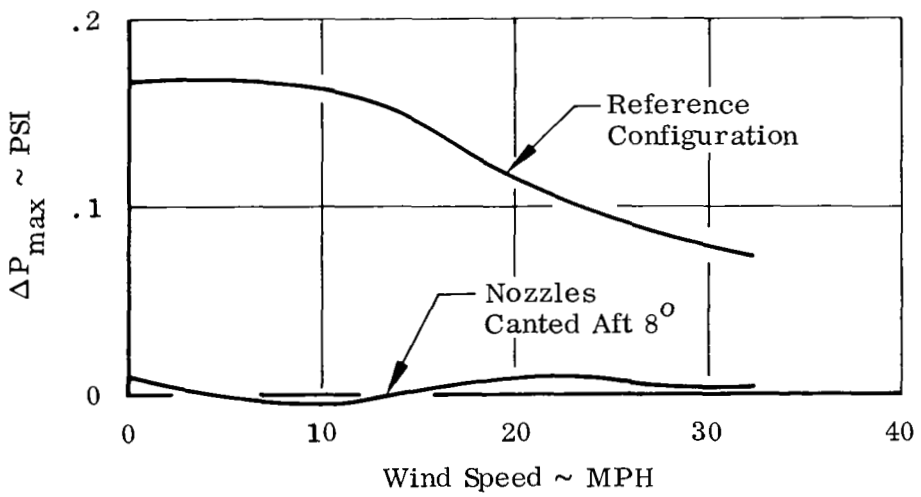

(a) Headwind

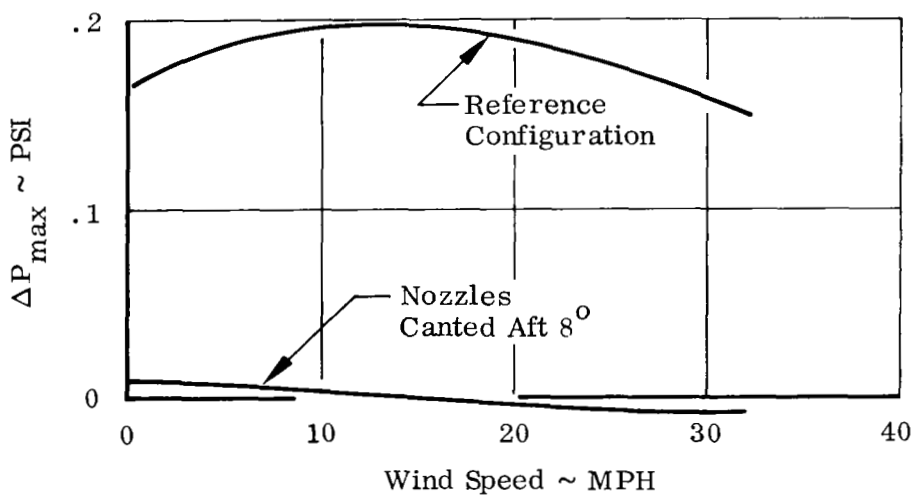

(b) Crosswind

FIGURE 53. EFFECT OF WIND ON POD PEAK PRESSURE

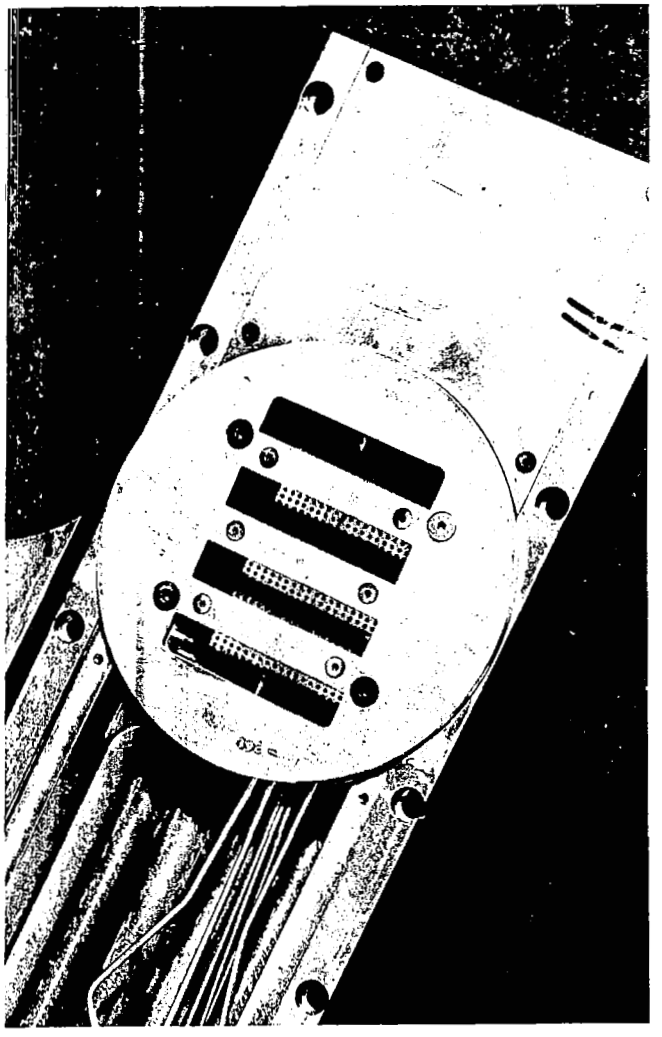

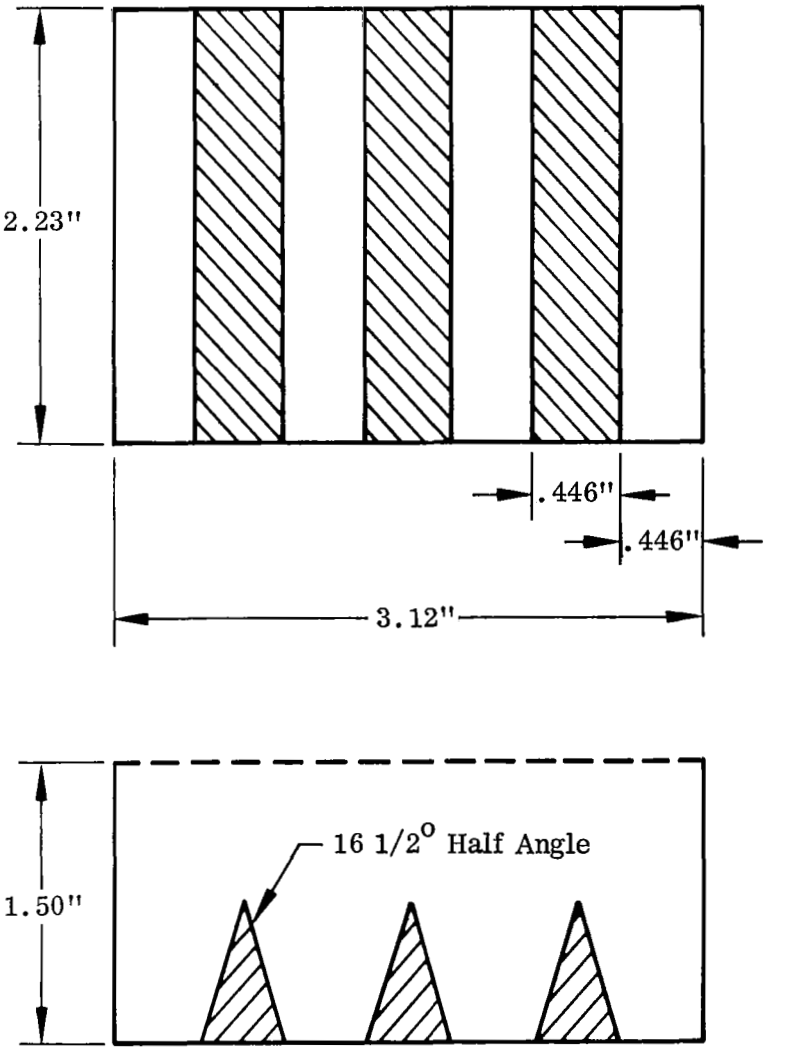

FIGURE 54. SUPPRESSION NOZZLE DETAIL

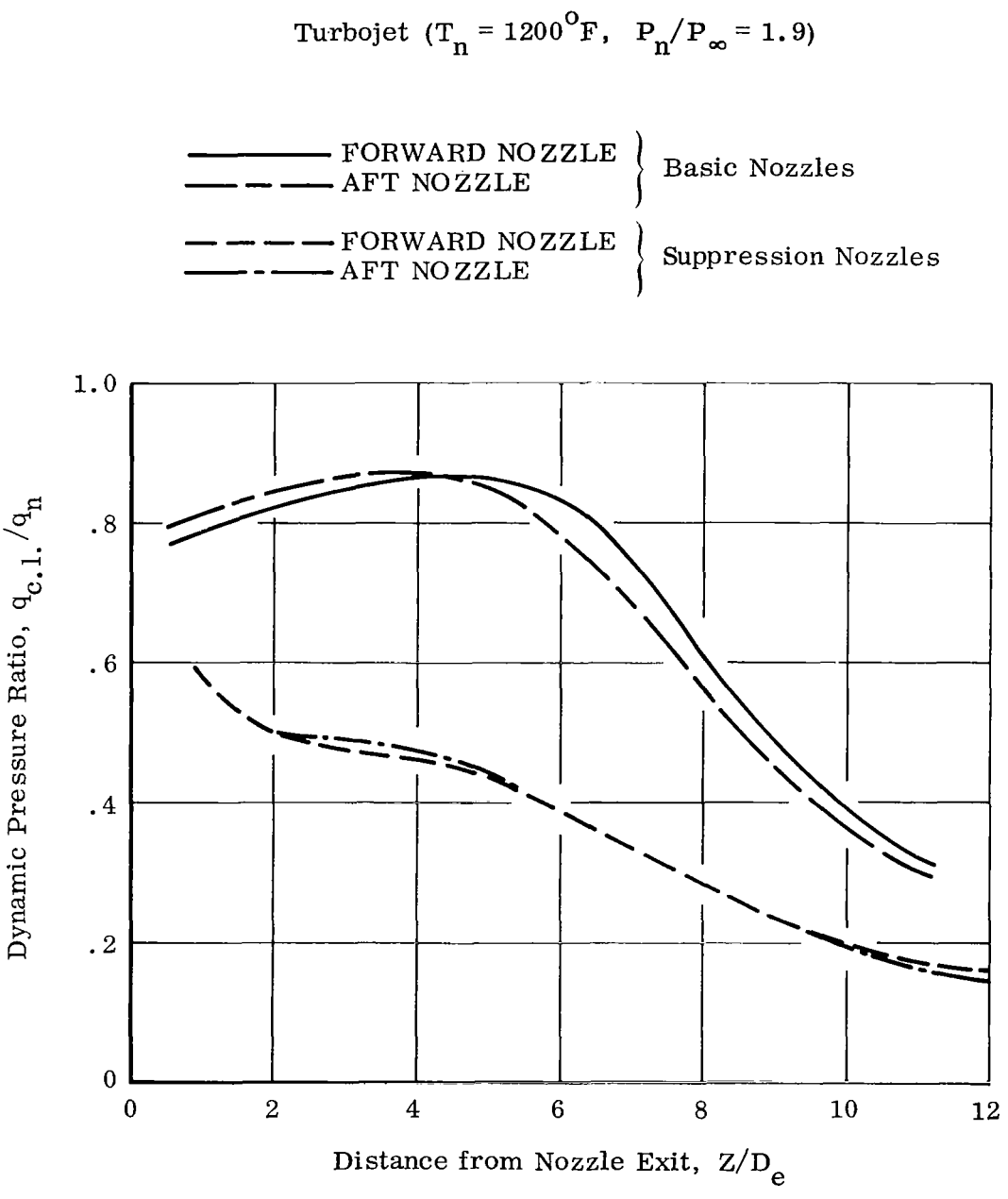

FIGURE 55. EXHAUST JET CENTERLINE DYNAMIC PRESSURE DECAY

Two Engine Operation
Turbojet
Wind < 3 MPH

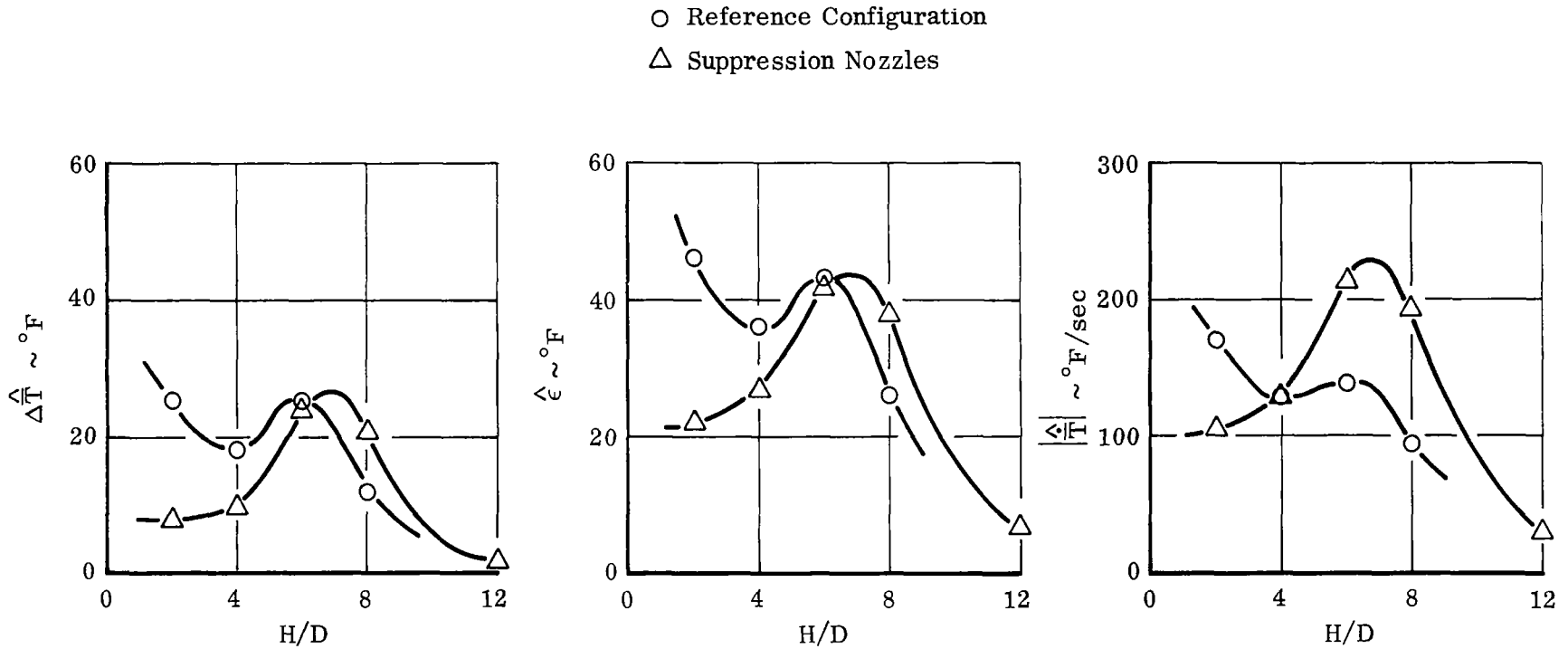

FIGURE 56. EFFECT OF H/D ON SUPPRESSION NOZZLE EFFECTIVENESS

Two Engine Operation
Turbojet
H/D = 4

○ Reference Configuration
△ Suppression Nozzles

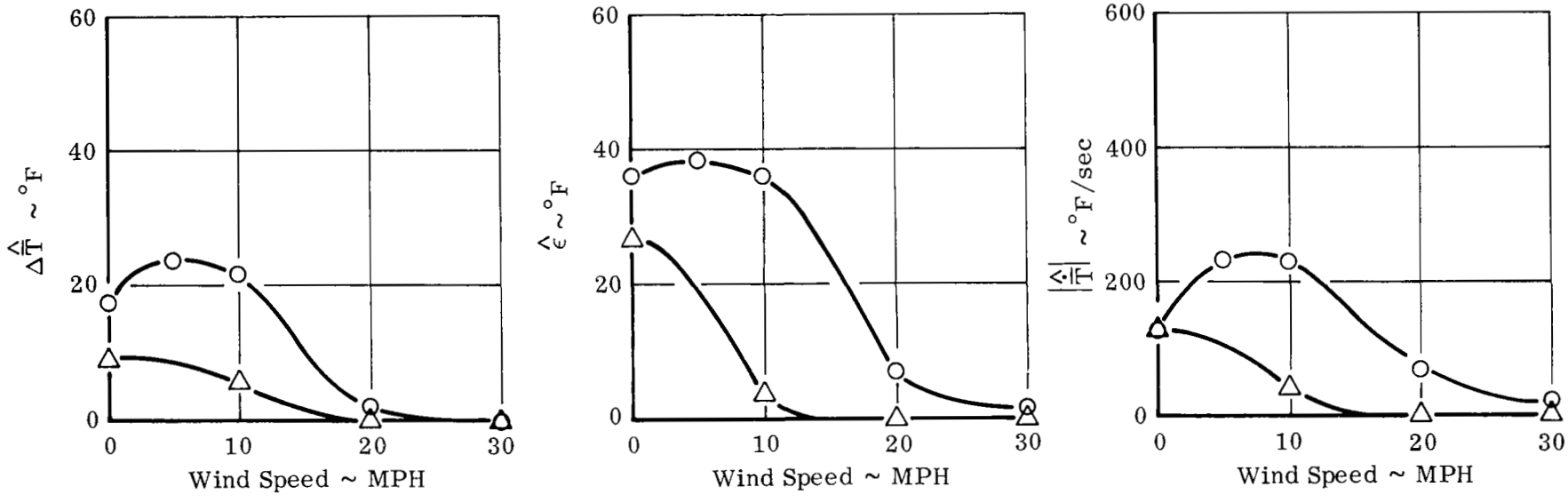

(a) Headwind

FIGURE 57. EFFECT OF WIND ON SUPPRESSION NOZZLE EFFECTIVENESS

Two Engine Operation
Turbojet
H/D = 4

○ Reference Configuration

△ Suppression Nozzles

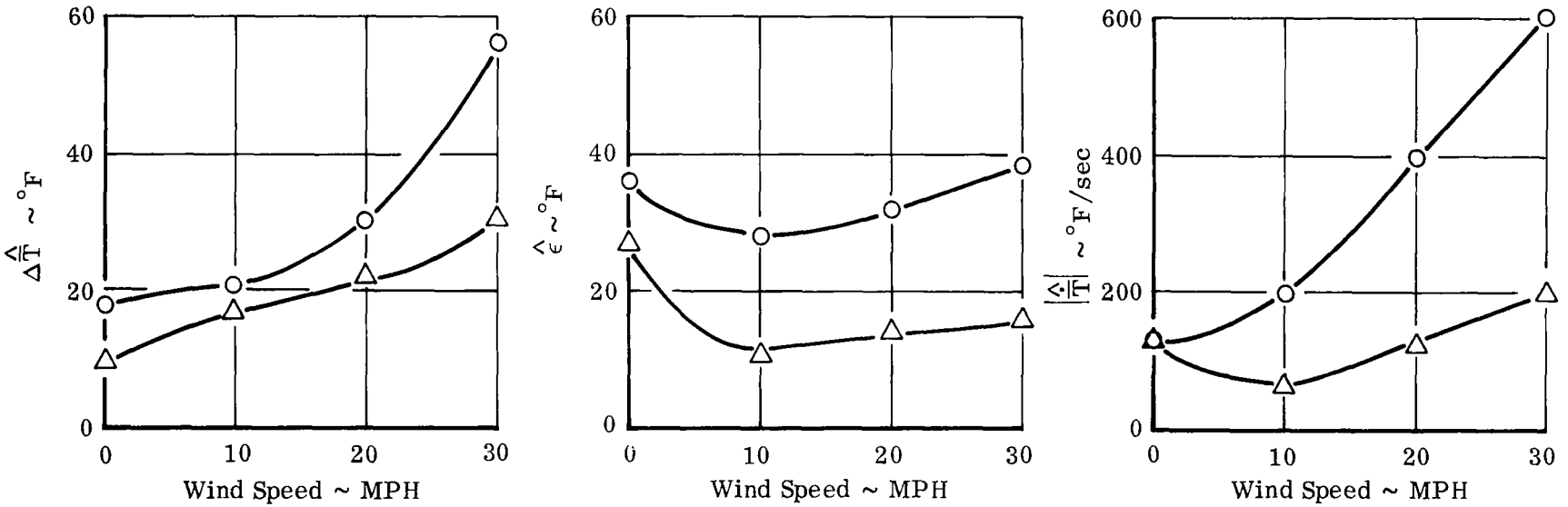

(b) Crosswind

FIGURE 57 (cont'd). EFFECT OF WIND ON SUPPRESSION NOZZLE EFFECTIVENESS

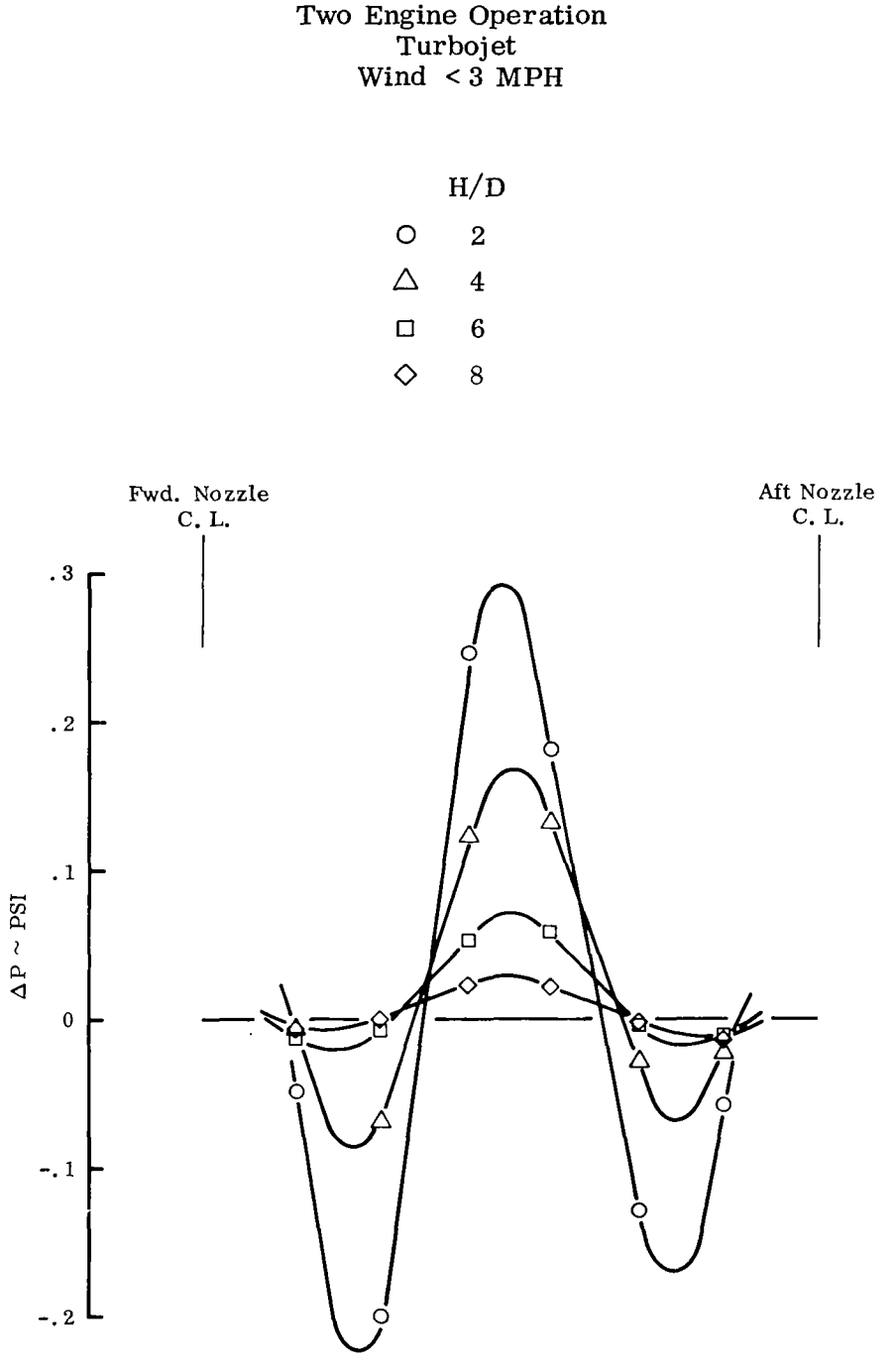

FIGURE 58. EFFECT OF H/D ON POD PRESSURE DISTRIBUTION - SUPPRESSION NOZZLES

Two Engine Operation
Turbojet
Wind < 3 MPH

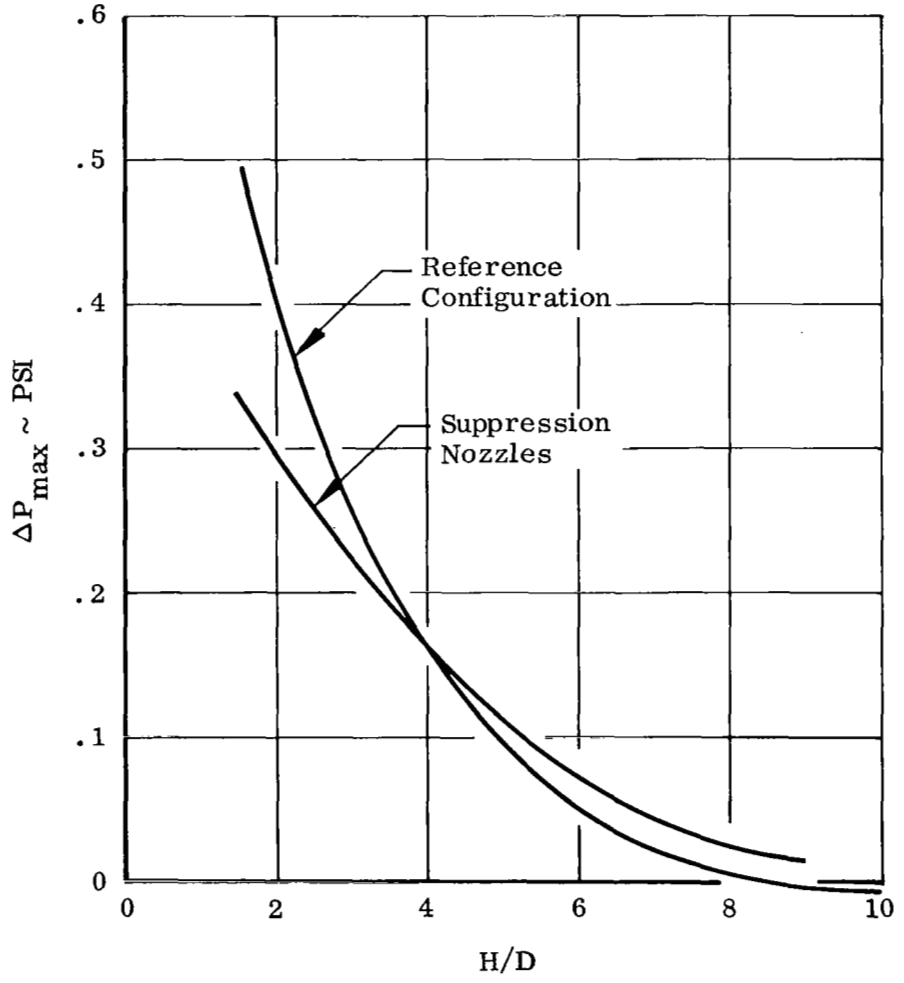

FIGURE 59. EFFECT OF H/D ON POD PRESSURE PEAK

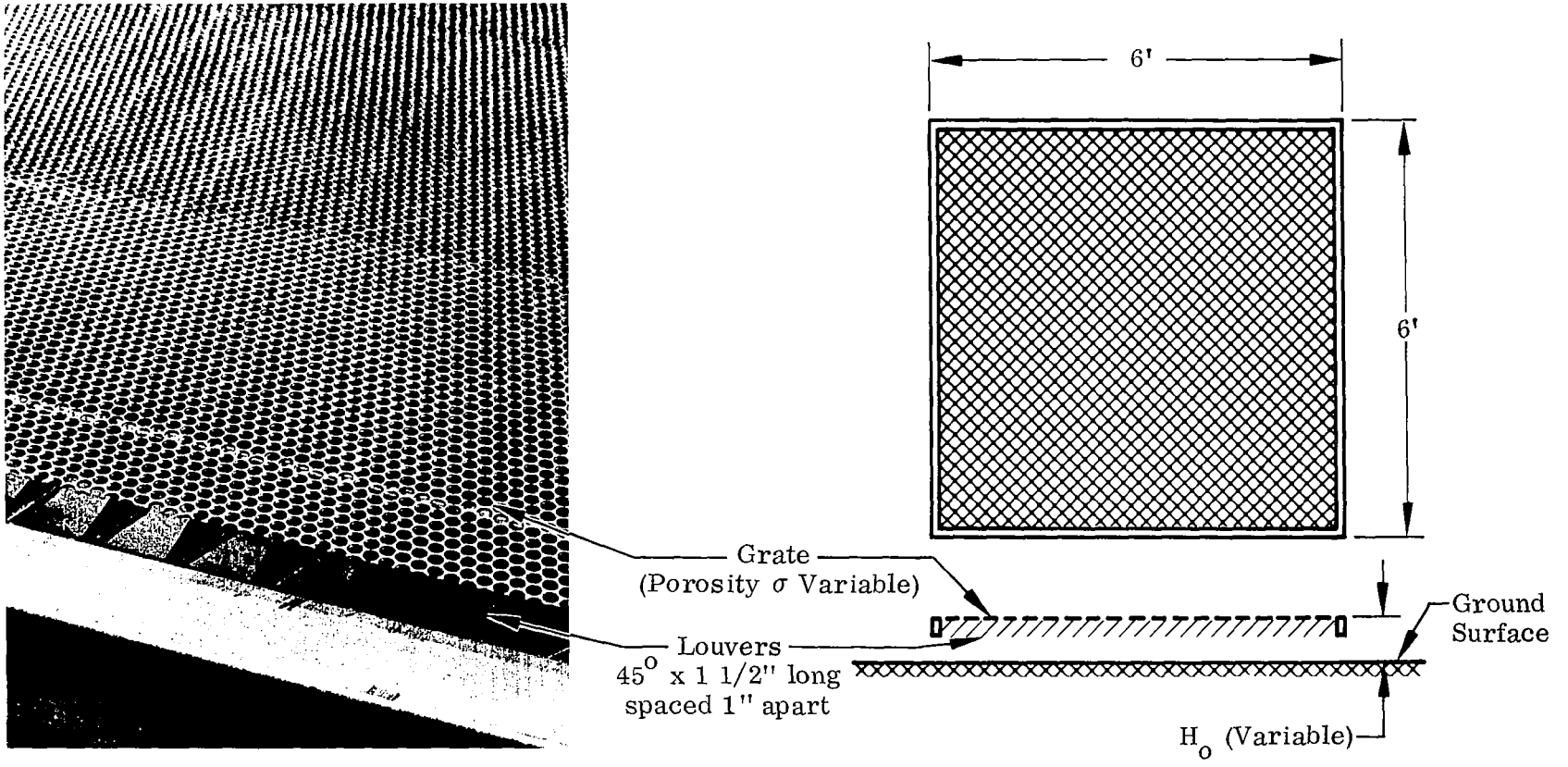

FIGURE 60. GROUND PLANE PLATFORM DETAIL - GRATE PLUS LOUVERS

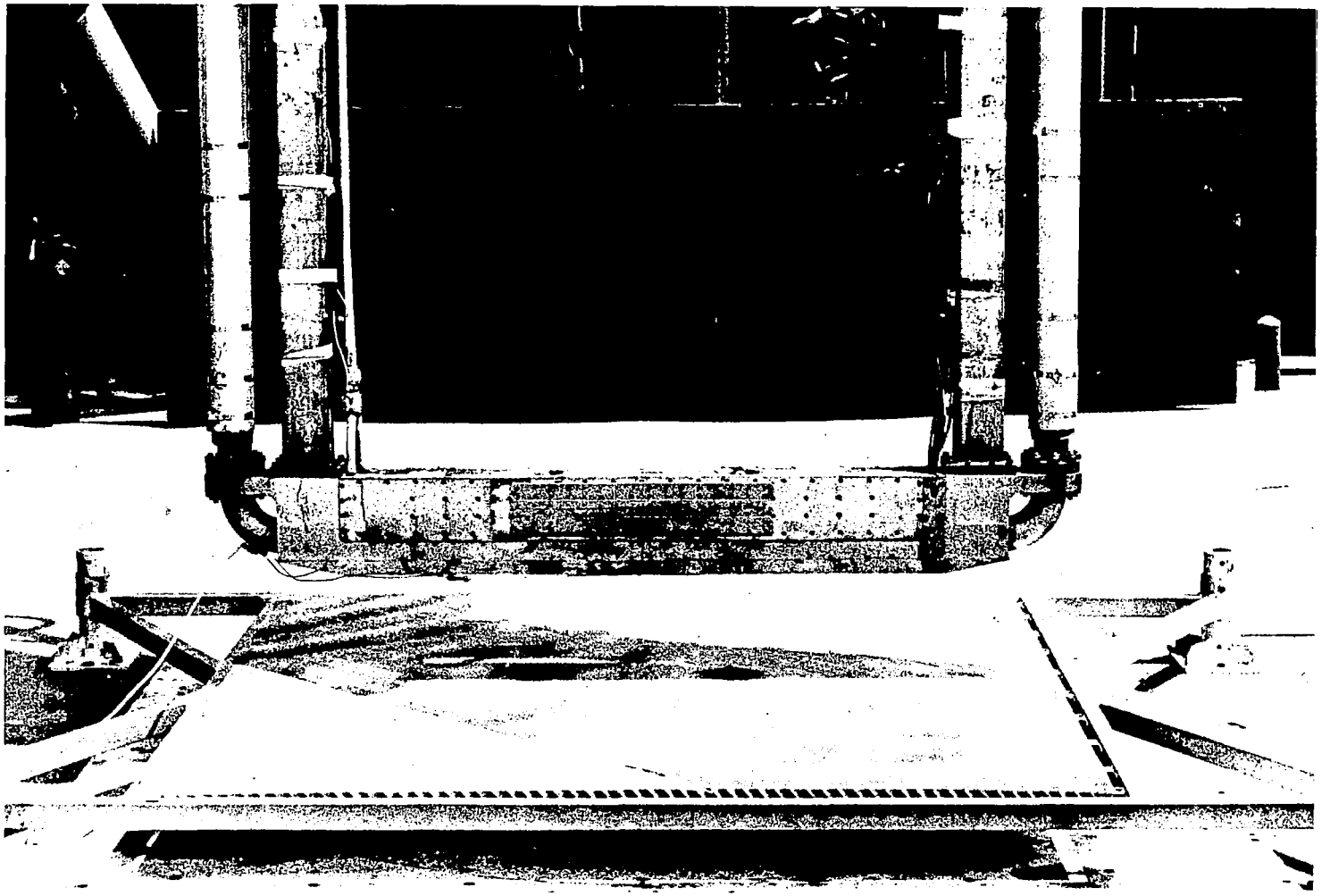

FIGURE 61. GROUND PLANE PLATFORM - GRATE PLUS LOUVERS

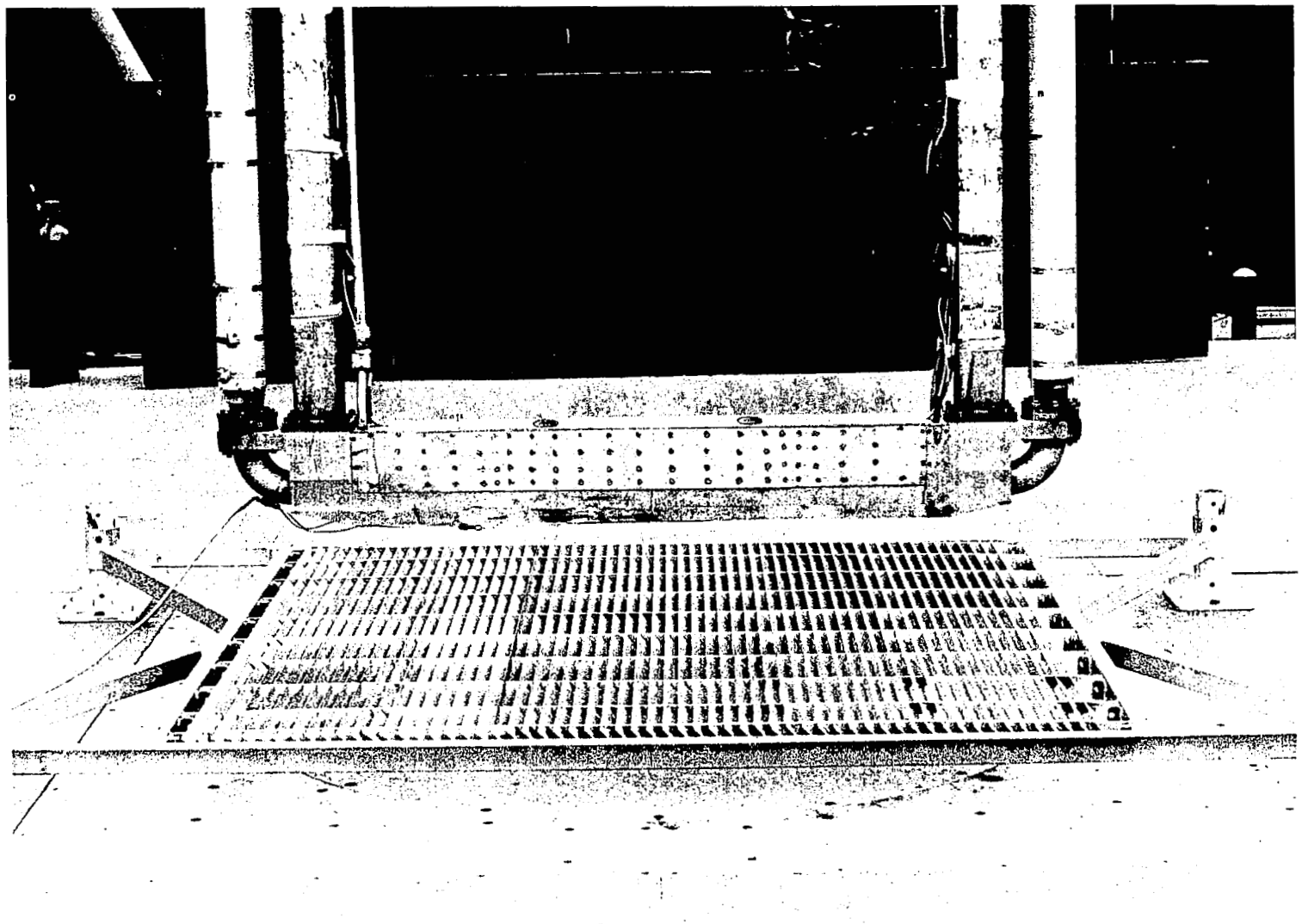

FIGURE 62. GROUND PLANE PLATFORM - LOUVERS ONLY

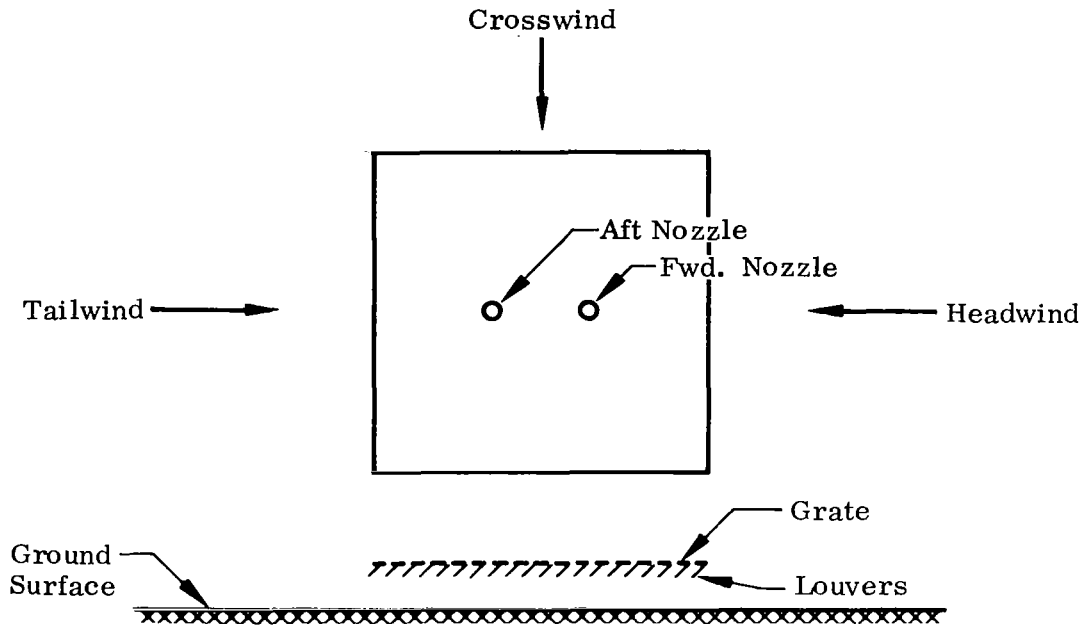

(a) Exhaust Vectored Aft

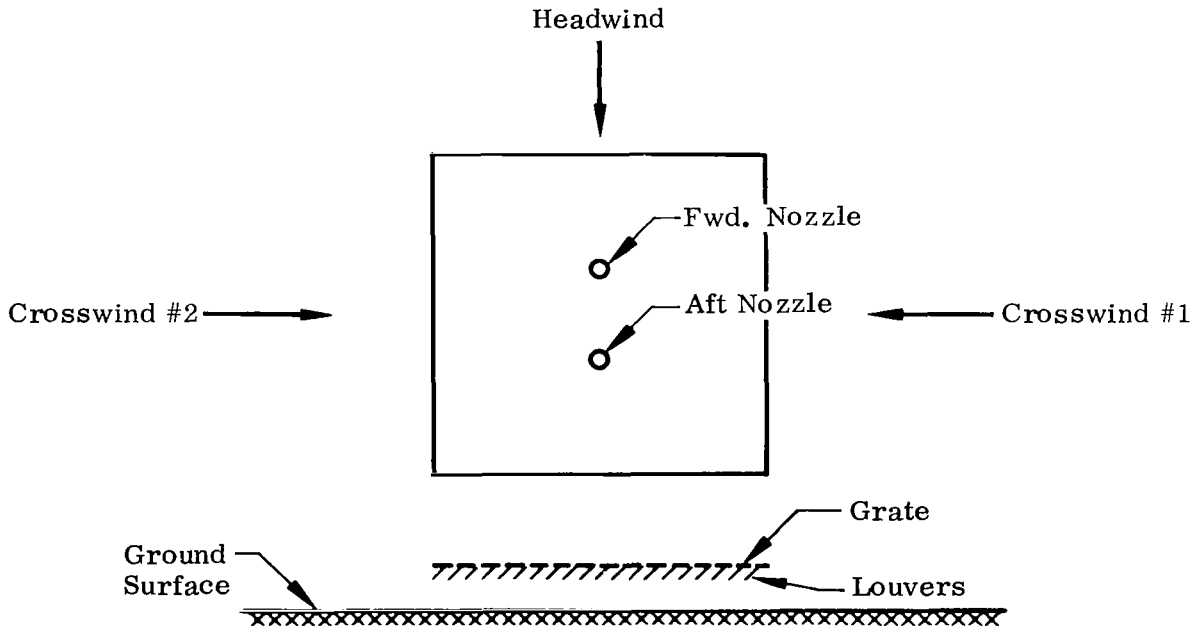

(b) Exhaust Vectored Left

FIGURE 63. GROUND PLANE PLATFORM WIND ORIENTATIONS - GRATE PLUS LOUVERS

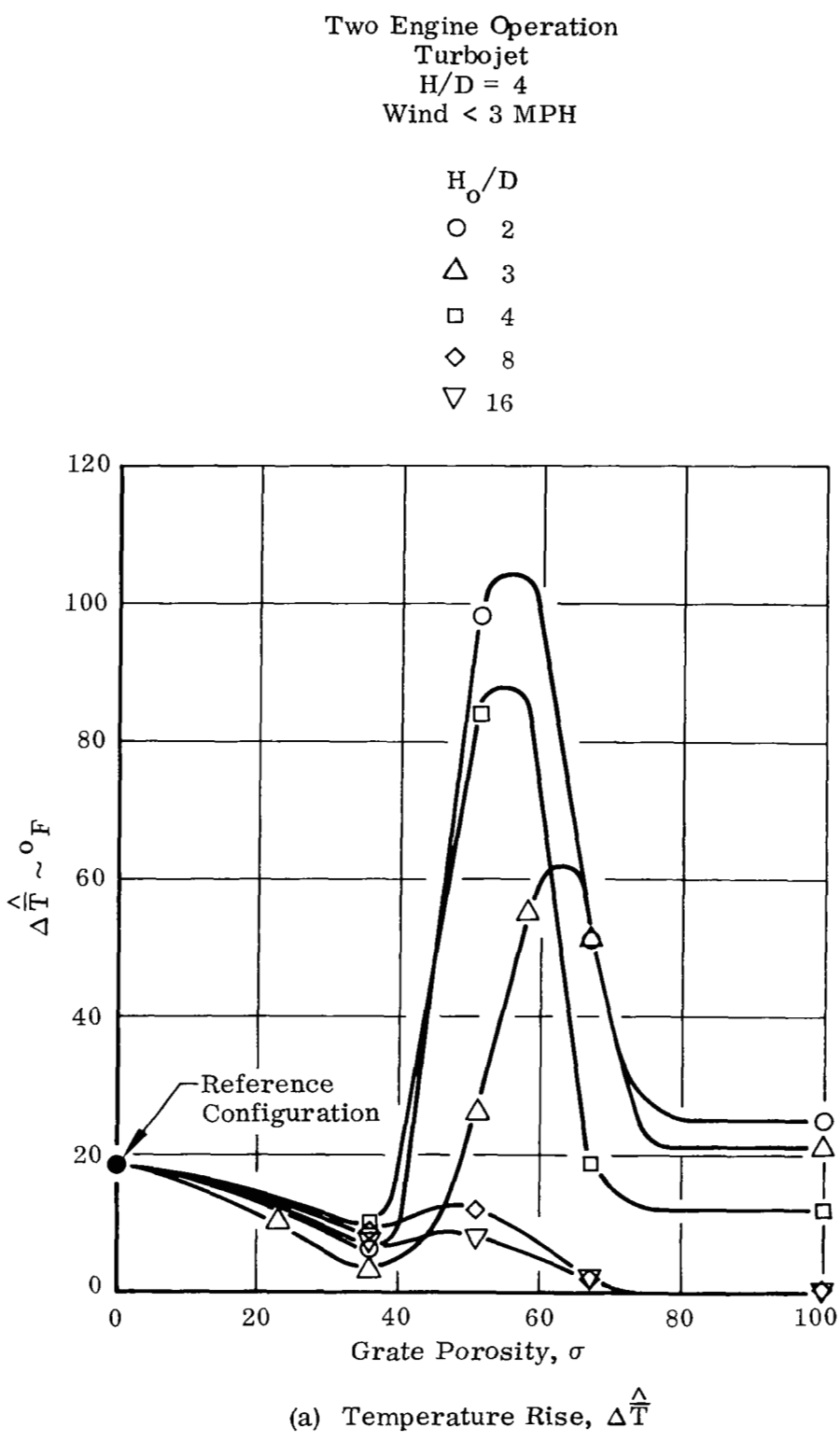

(a) Temperature Rise, $\Delta\hat{\bar{T}}$

FIGURE 64. EFFECT OF GROUND PLANE PLATFORM POROSITY AND HEIGHT - GRATE ONLY

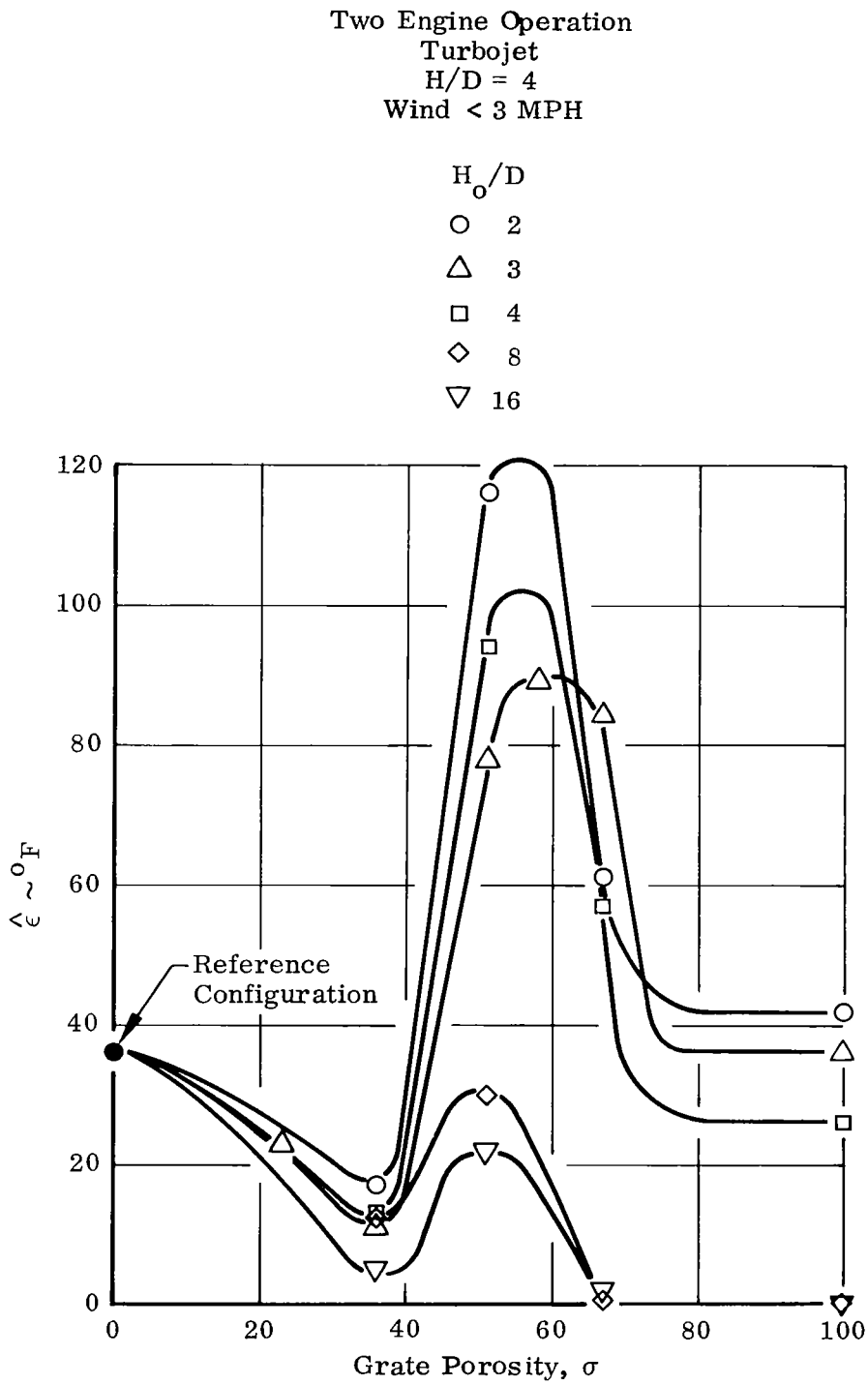

(b) Temperature Distortion, $\hat{\epsilon}$

FIGURE 64 (cont'd). EFFECT OF GROUND PLANE PLATFORM POROSITY AND HEIGHT - GRATE ONLY

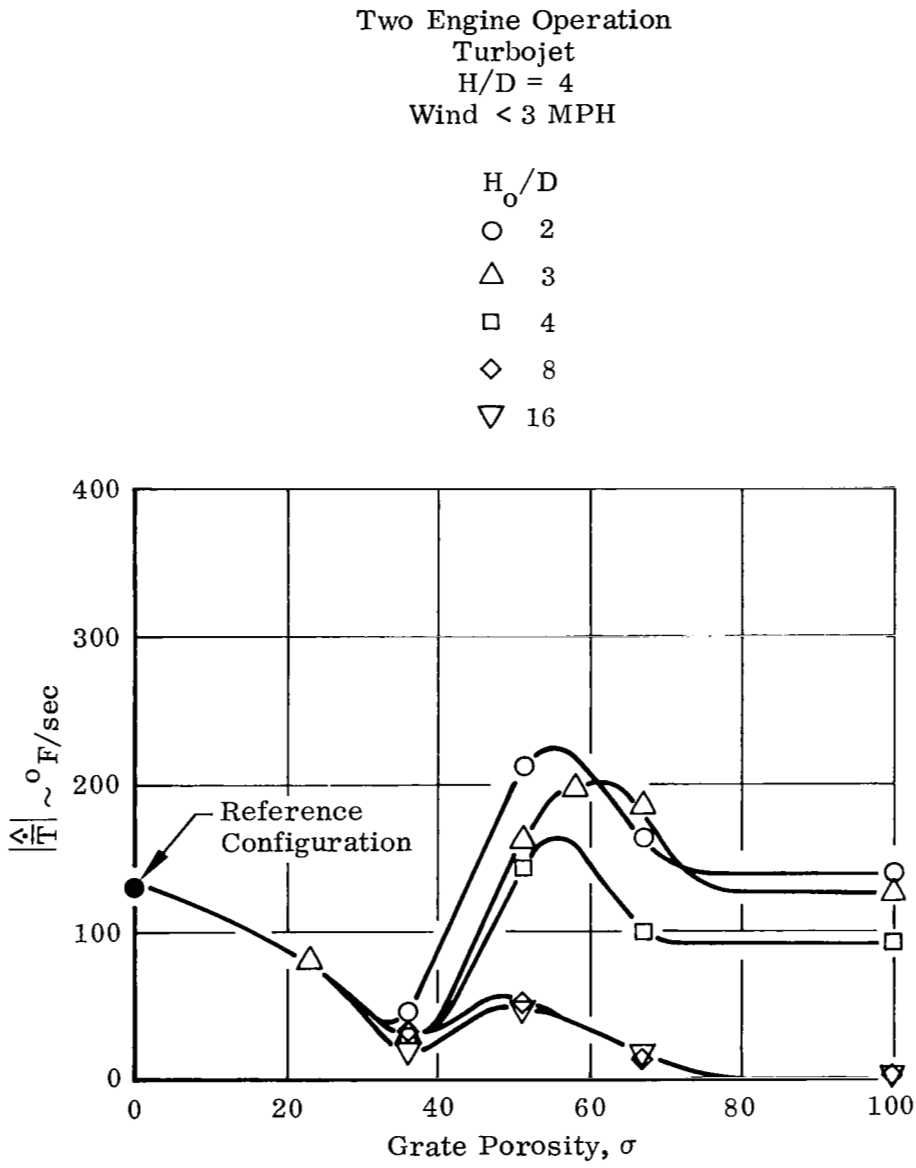

(c) Temperature Rate of Rise, $\left|\frac{\Delta}{T}\right|$

FIGURE 64 (cont'd). EFFECT OF GROUND PLANE PLATFORM POROSITY AND HEIGHT - GRATE ONLY

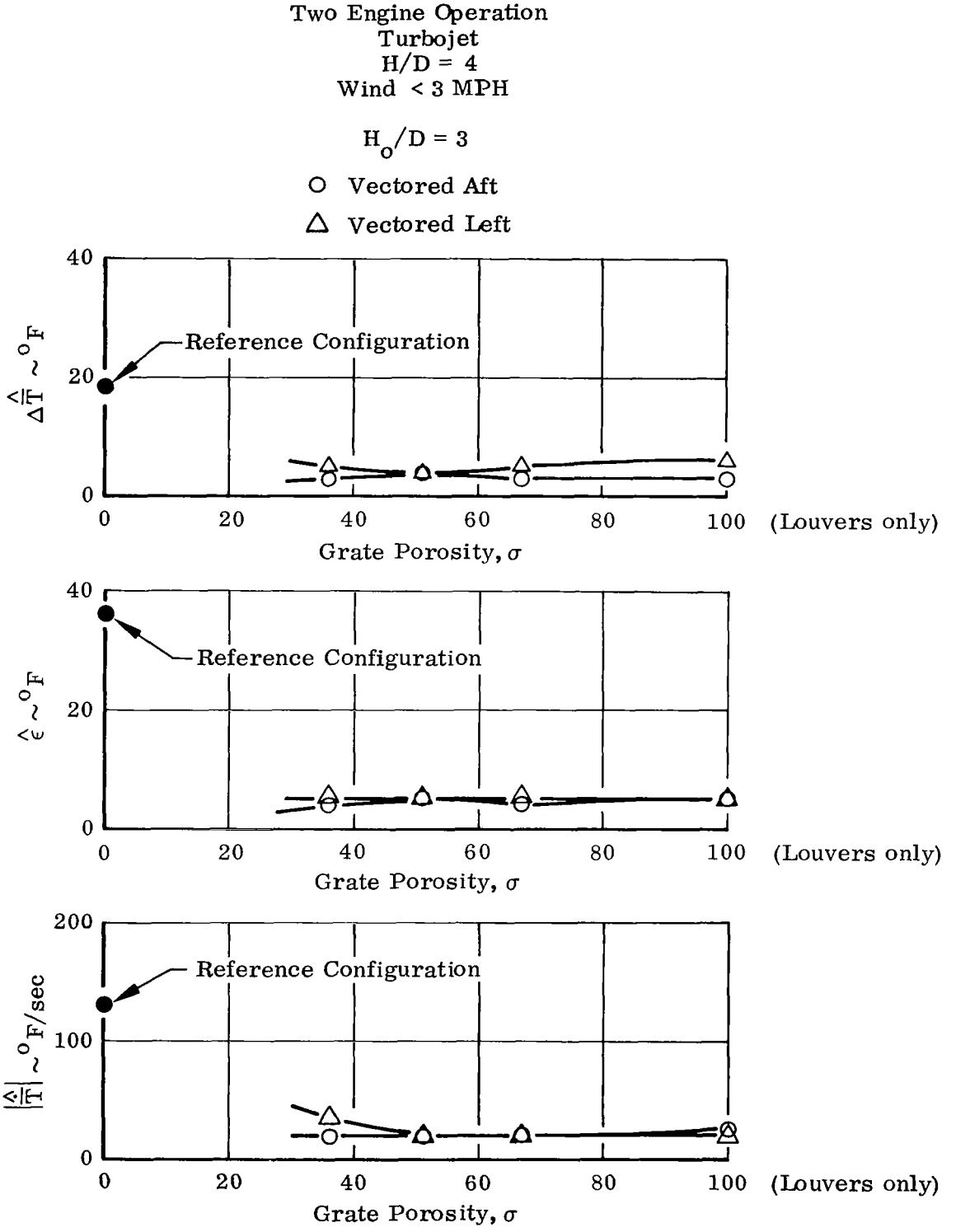

FIGURE 65. EFFECT OF GROUND PLANE PLATFORM POROSITY - GRATE PLUS LOUVERS

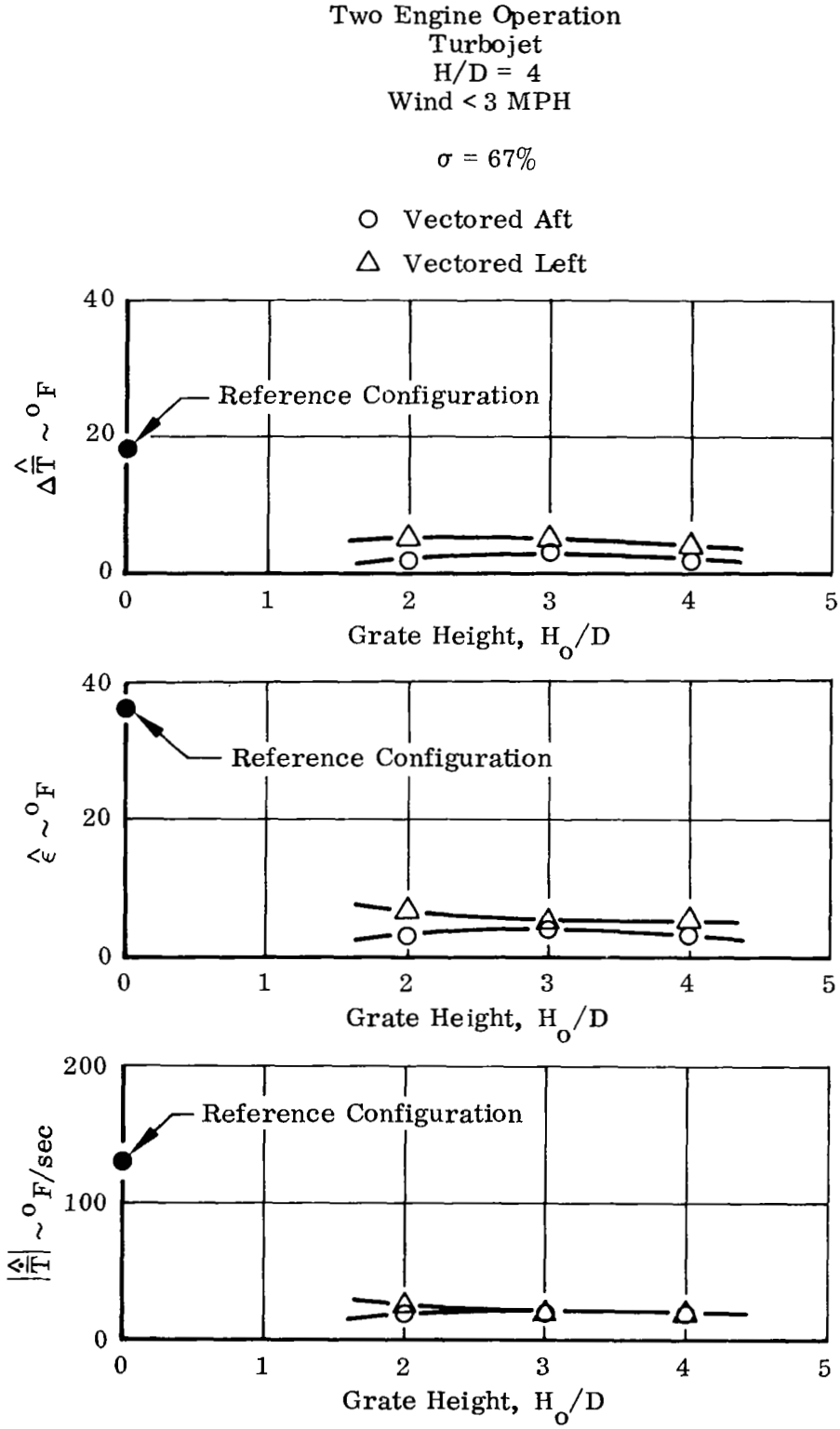

FIGURE 66. EFFECT OF GROUND PLANE PLATFORM HEIGHT - GRATE PLUS LOUVERS

Two Engine Operation
Turbojet
Wind < 3 MPH

○ Reference Configuration
△ Ground Plane Platform (Exhaust Vectored Aft)
□ Ground Plane Platform (Exhaust Vectored Left)
$H_o/D = 3$
$\sigma = 51\%$

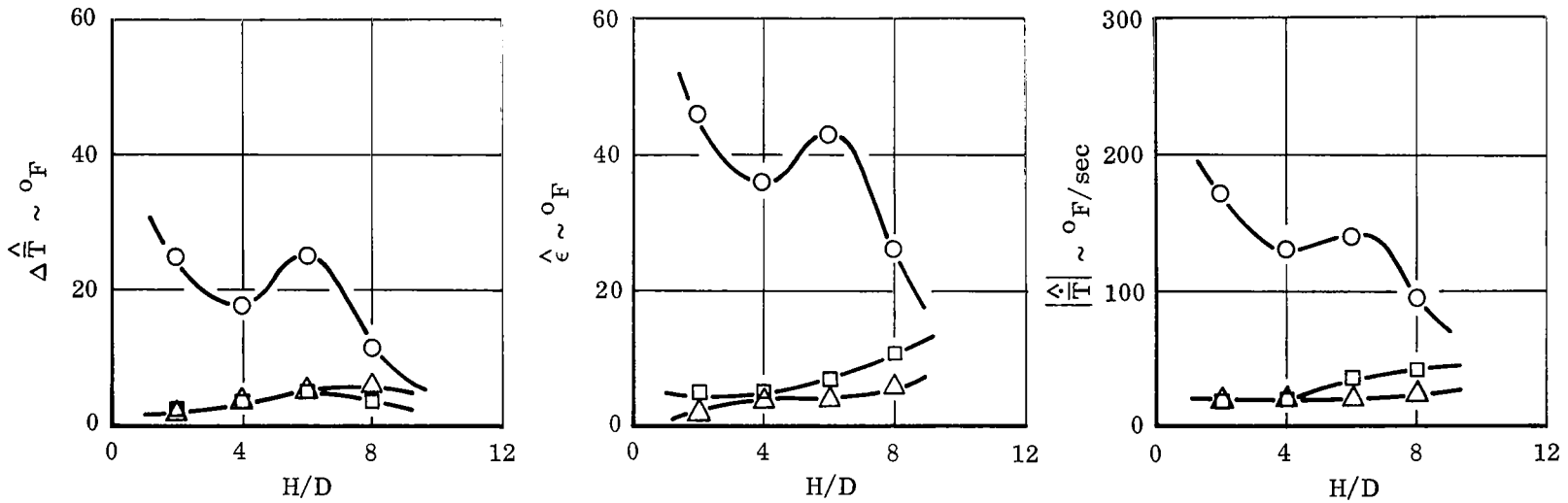

FIGURE 67. EFFECT OF H/D ON GROUND PLANE PLATFORM EFFECTIVENESS - GRATE PLUS LOUVERS

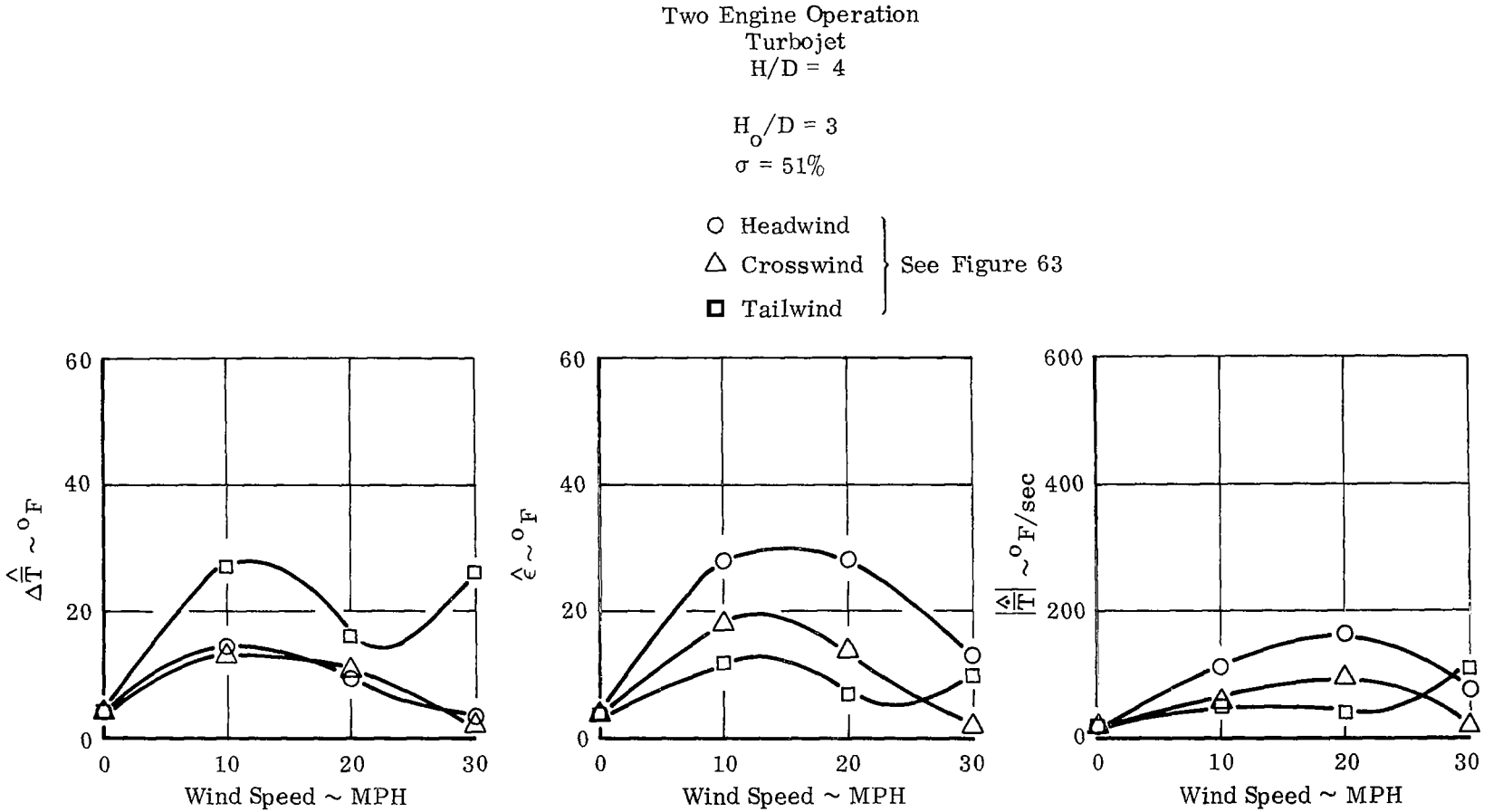

(a) Exhaust Vectored Aft

FIGURE 68. EFFECT OF WIND ON GROUND PLANE PLATFORM EFFECTIVENESS - GRATE PLUS LOUVERS

Two Engine Operation
Turbojet
H/D = 4

$H_o/D = 3$
$\sigma = 51\%$

○ Crosswind #1
△ Headwind
□ Crosswind #2
} See Figure 63

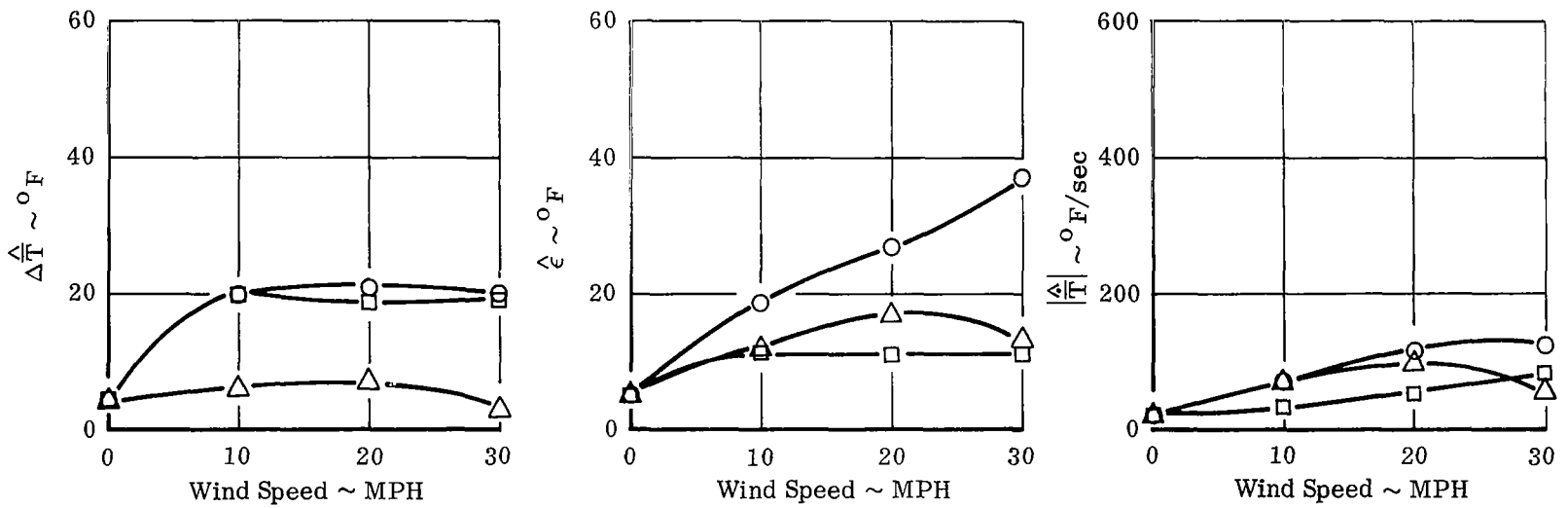

(b) Exhaust Vectored Left

FIGURE 68 (cont'd). EFFECT OF WIND ON GROUND PLANE PLATFORM EFFECTIVENESS - GRATE PLUS LOUVERS

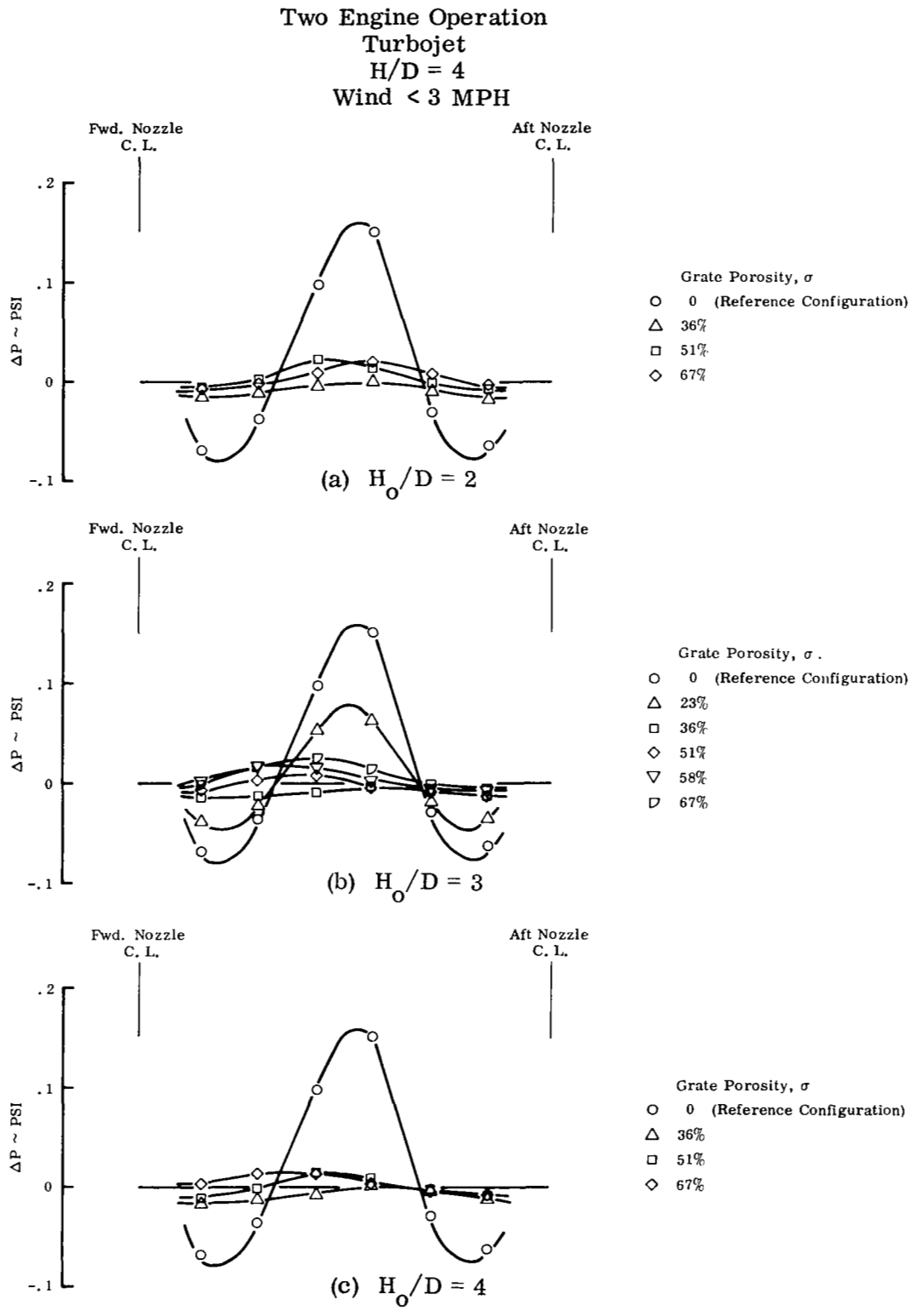

FIGURE 69. EFFECT OF GROUND PLANE PLATFORM ON POD PRESSURE DISTRIBUTION - GRATE ONLY

Two Engine Operation
Turbojet
H/D = 4
Wind <3 MPH

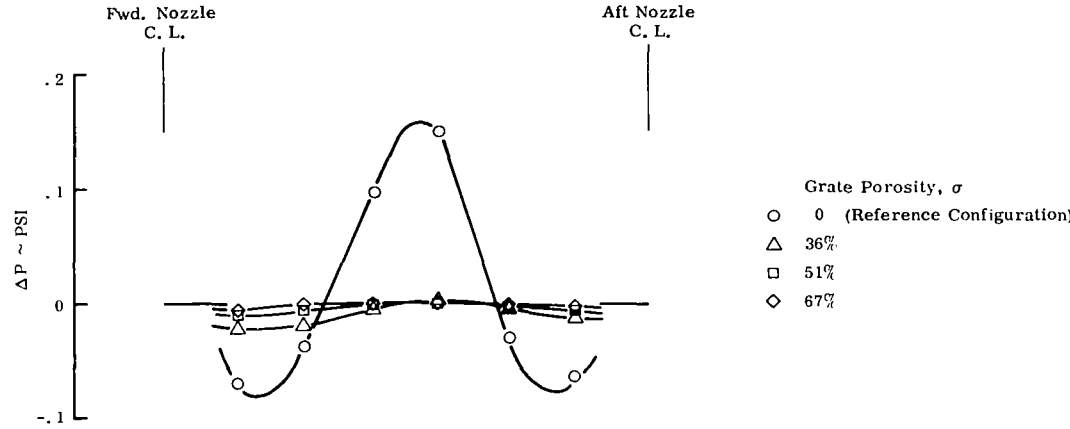

(d) $H_o/D = 8$

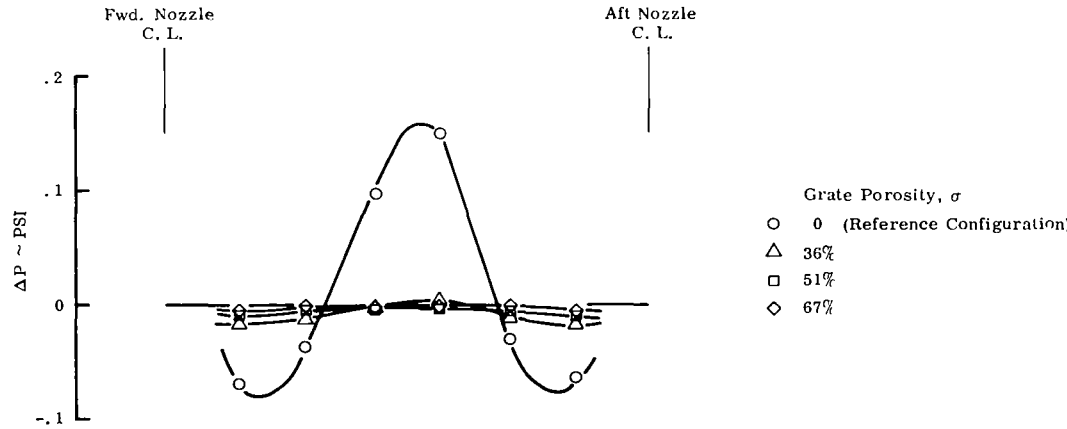

(e) $H_o/D = 16$

FIGURE 69 (cont'd). EFFECT OF GROUND PLANE PLATFORM ON POD PRESSURE DISTRIBUTION - GRATE ONLY

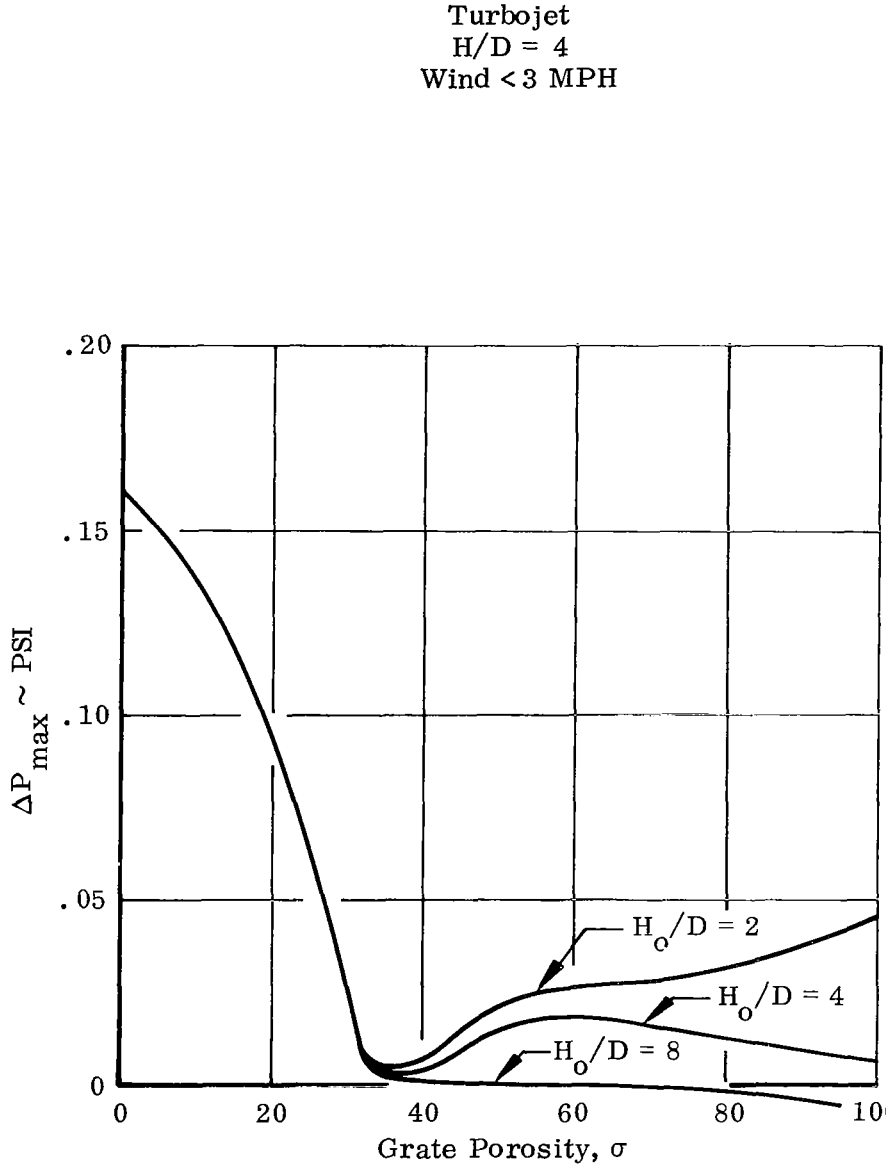

FIGURE 70. EFFECT OF GROUND PLANE PLATFORM ON POD PEAK PRESSURE - GRATE ONLY

Two Engine Operation
H/D = 4
Wind < 3 MPH

$H_o/D = 3$
$\sigma = 51\%$

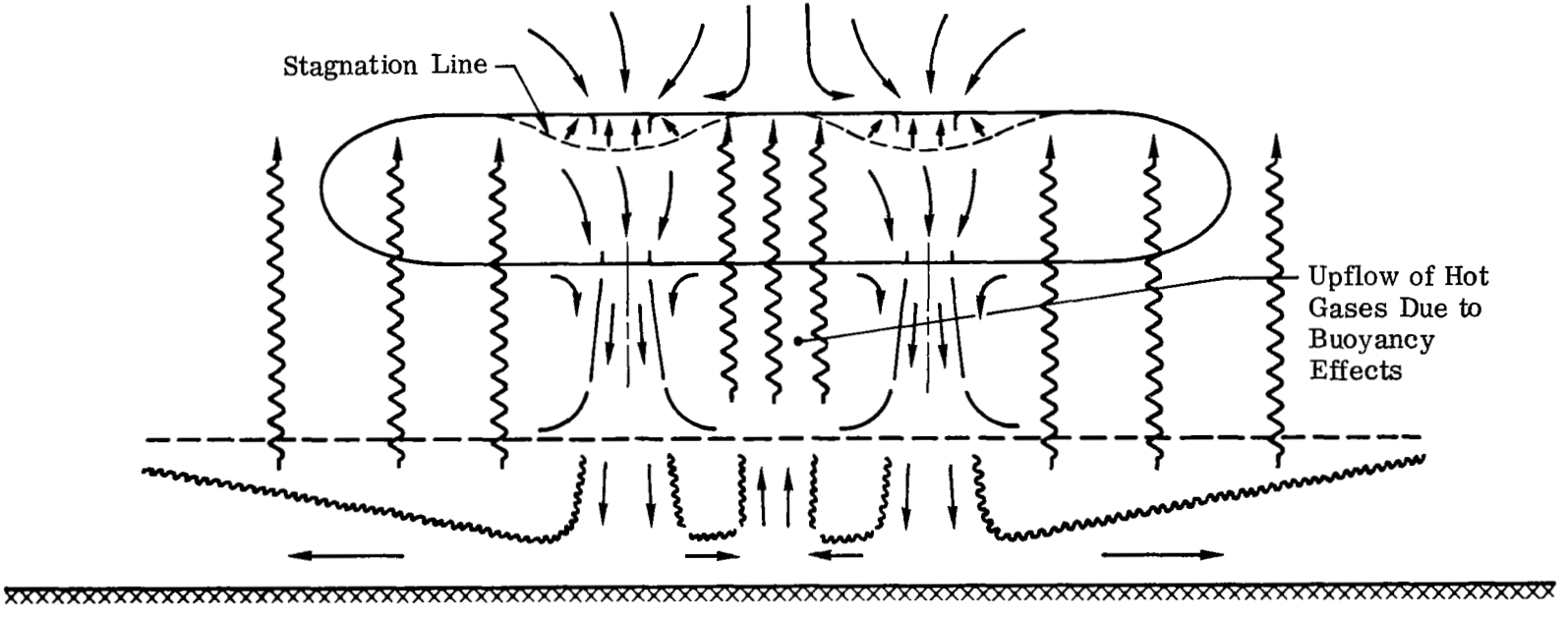

FIGURE 71. FLOW FIELD SCHEMATIC - GRATE ONLY

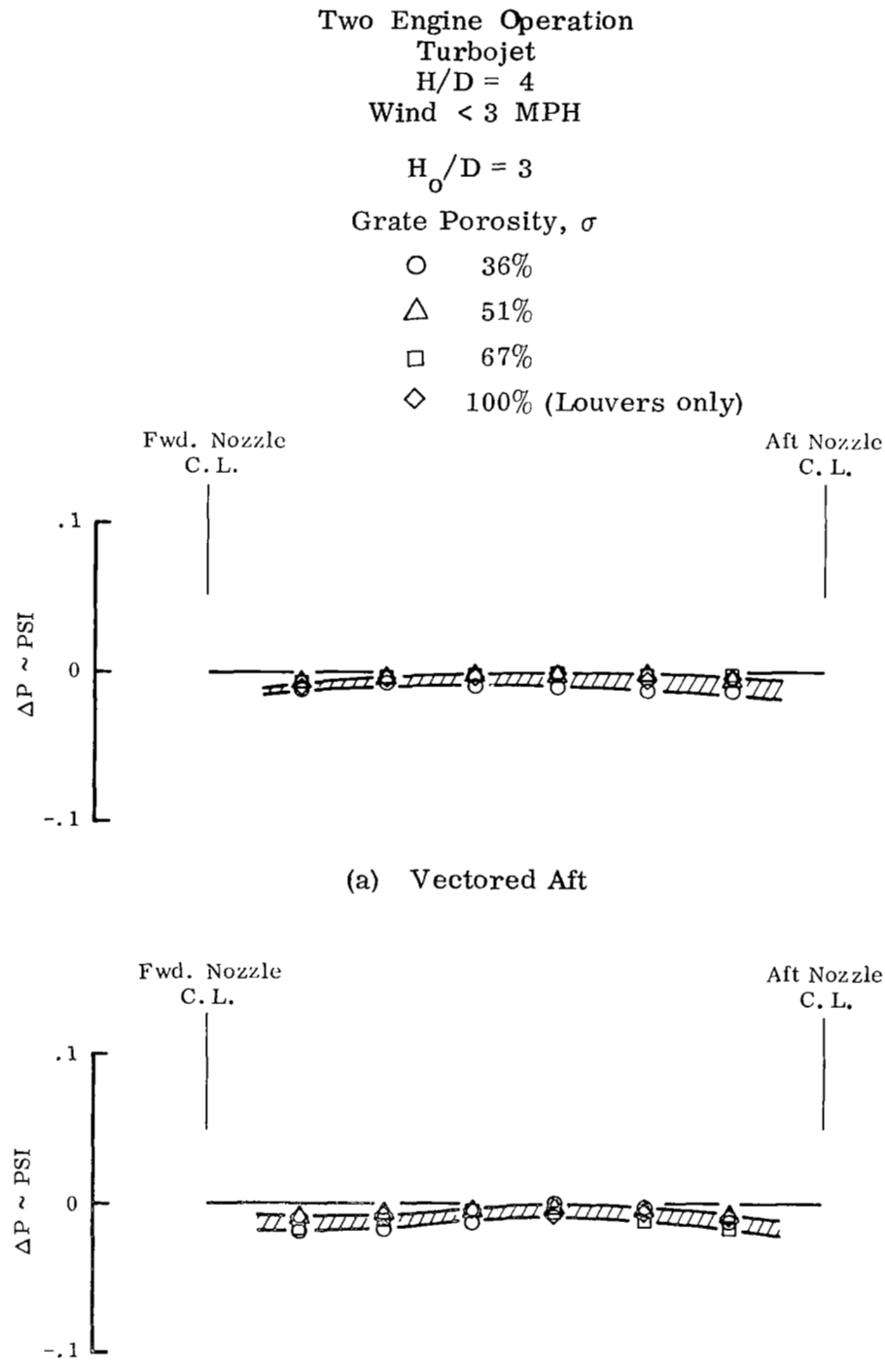

FIGURE 72. EFFECT OF GROUND PLANE PLATFORM ON POD PRESSURE DISTRIBUTION - GRATE PLUS LOUVERS

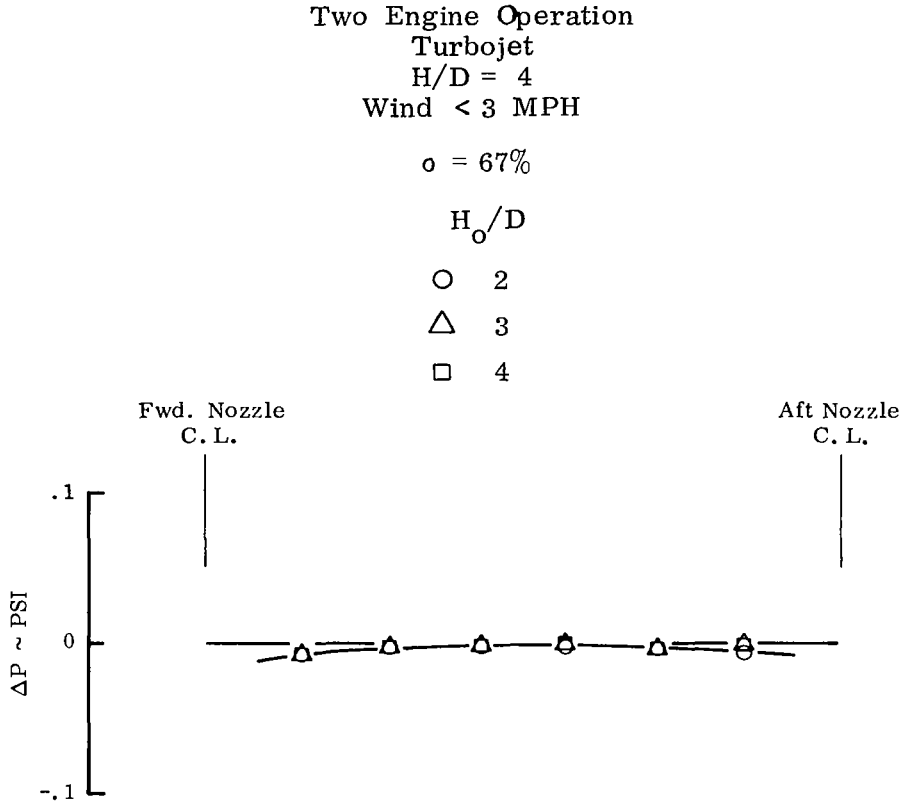

(a) Vectored Aft

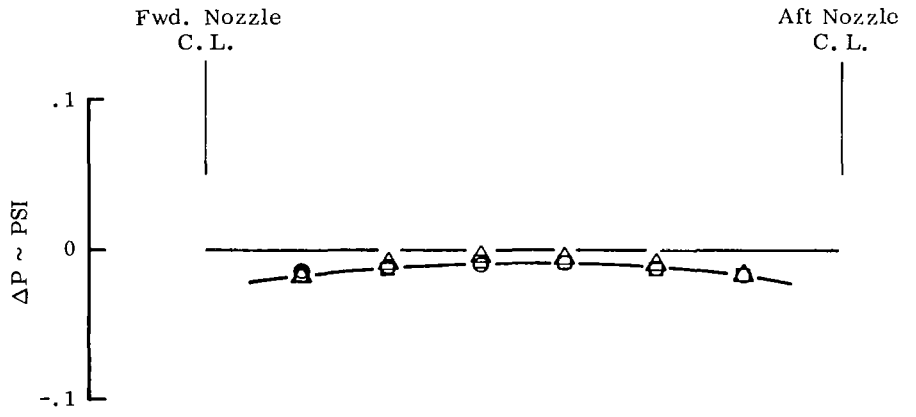

(b) Vectored Left

FIGURE 73. EFFECT OF GROUND PLANE PLATFORM ON POD PRESSURE DISTRIBUTION - GRATE PLUS LOUVERS

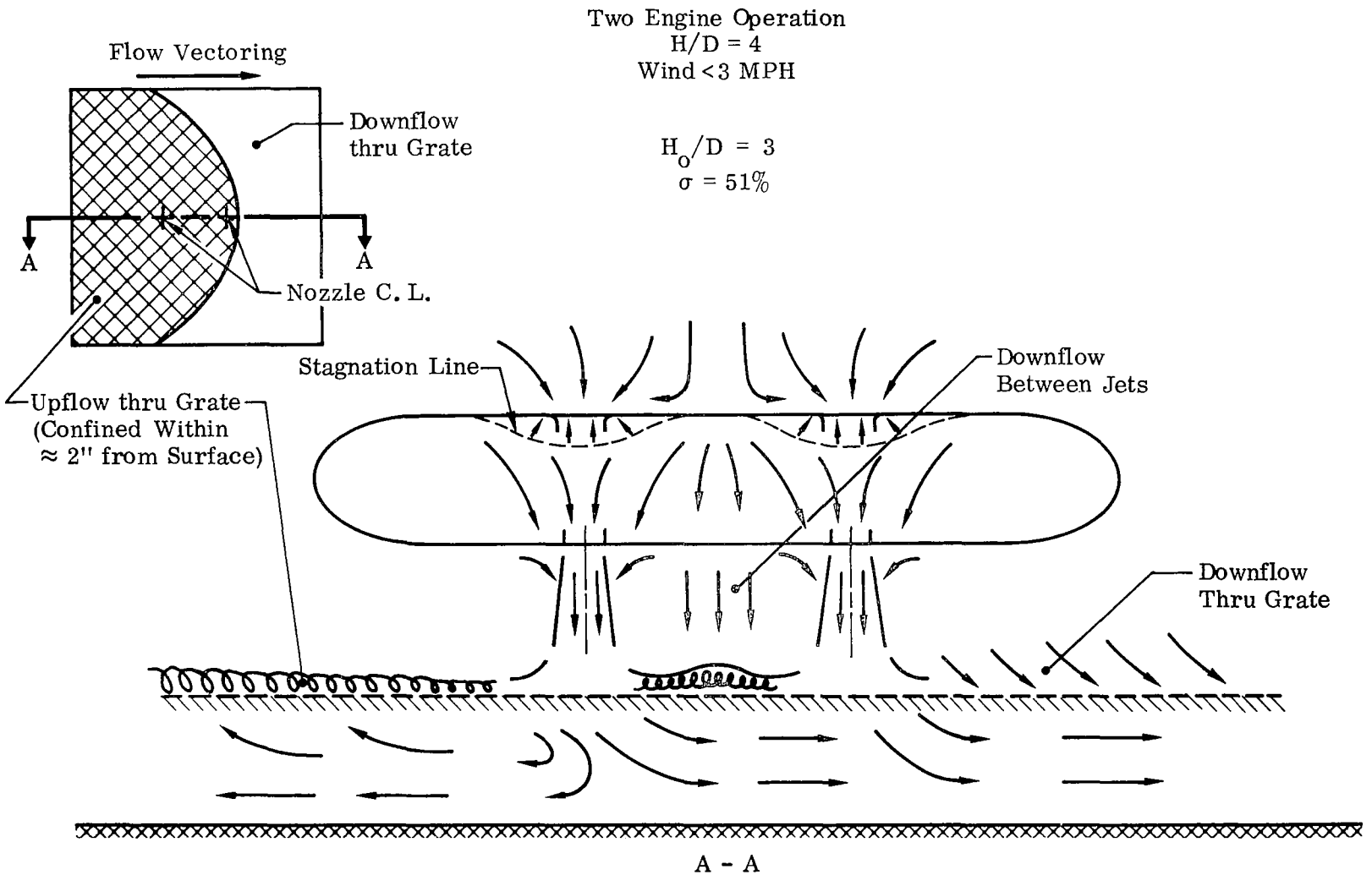

(a) Exhaust Vectored Aft

FIGURE 74. FLOW FIELD SCHEMATIC - GRATE PLUS LOUVERS

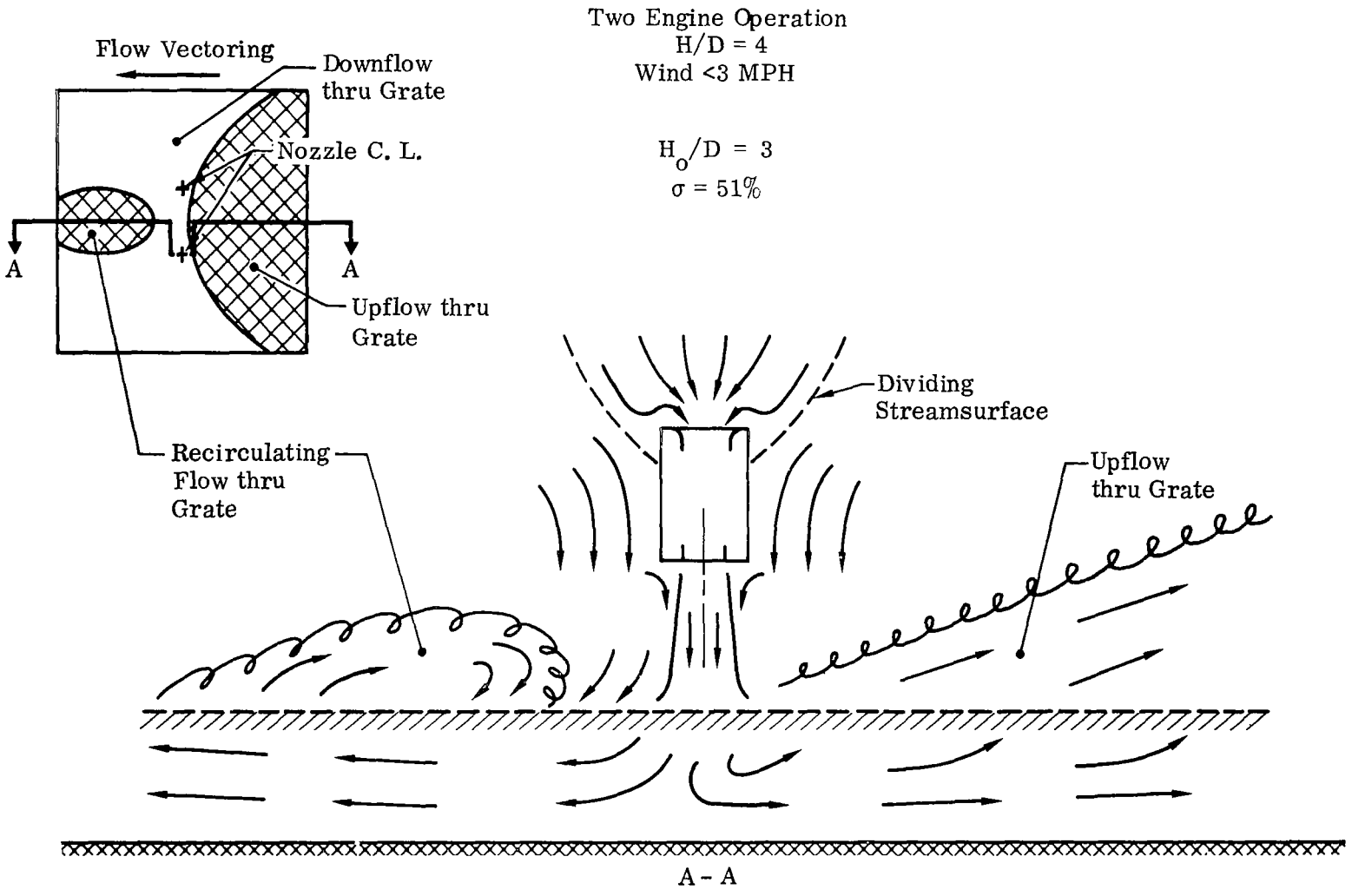

(b) Exhaust Vectored Left

FIGURE 74 (cont'd). FLOW FIELD SCHEMATIC - GRATE PLUS LOUVERS

Two Engine Operation
Turbojet
Wind < 3 MPH

$H_o/D = 3$

$\sigma = 51\%$

H/D

○ 2

△ 4

□ 6

◇ 8

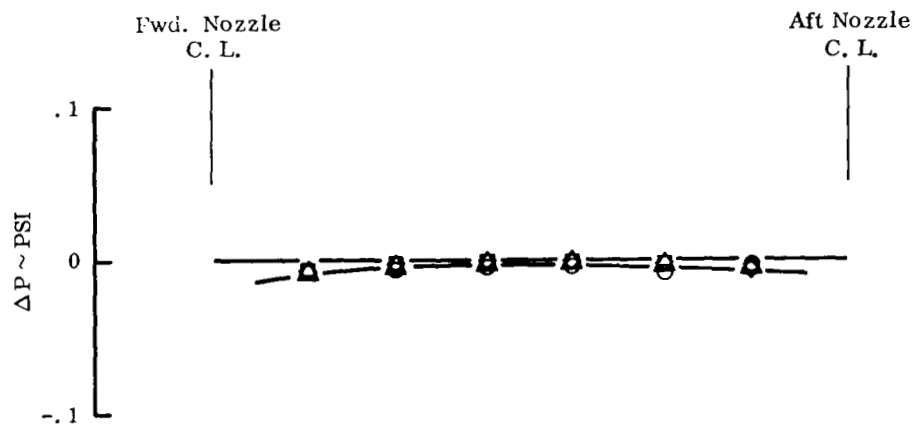

(a) Exhaust Vectored Aft

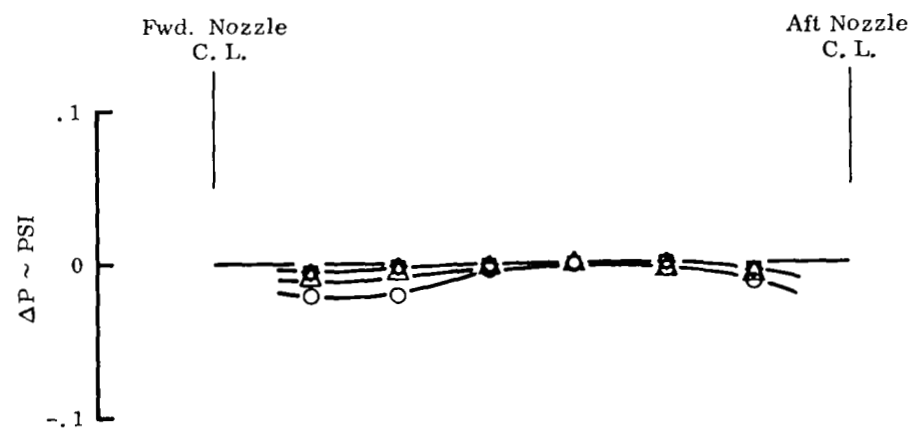

(b) Exhaust Vectored Left

FIGURE 75. EFFECT OF H/D ON POD PRESSURE DISTRIBUTION - GRATE PLUS LOUVERS

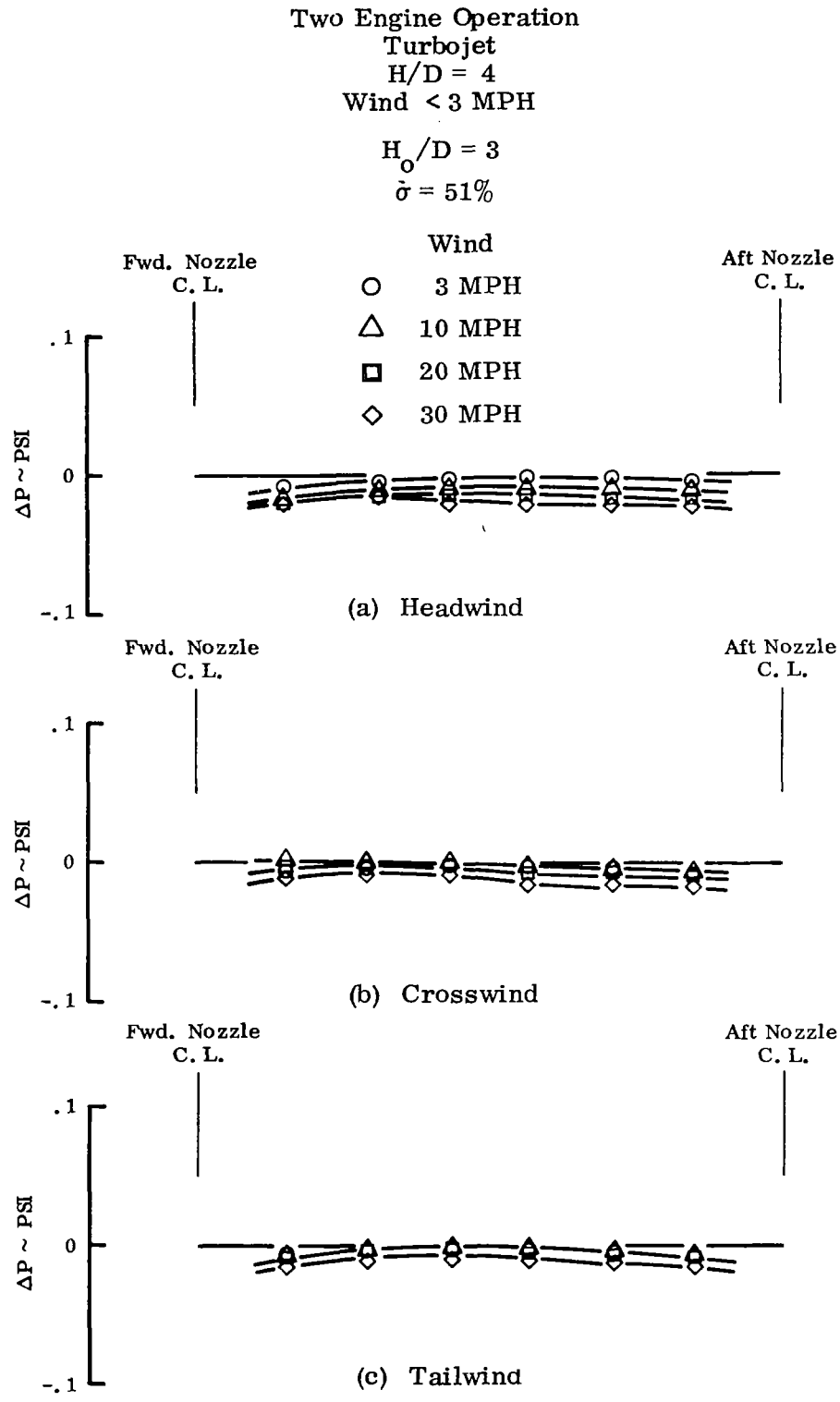

FIGURE 76. EFFECT OF WIND ON POD PRESSURE DISTRIBUTION - GRATE PLUS LOUVERS VECTORED AFT

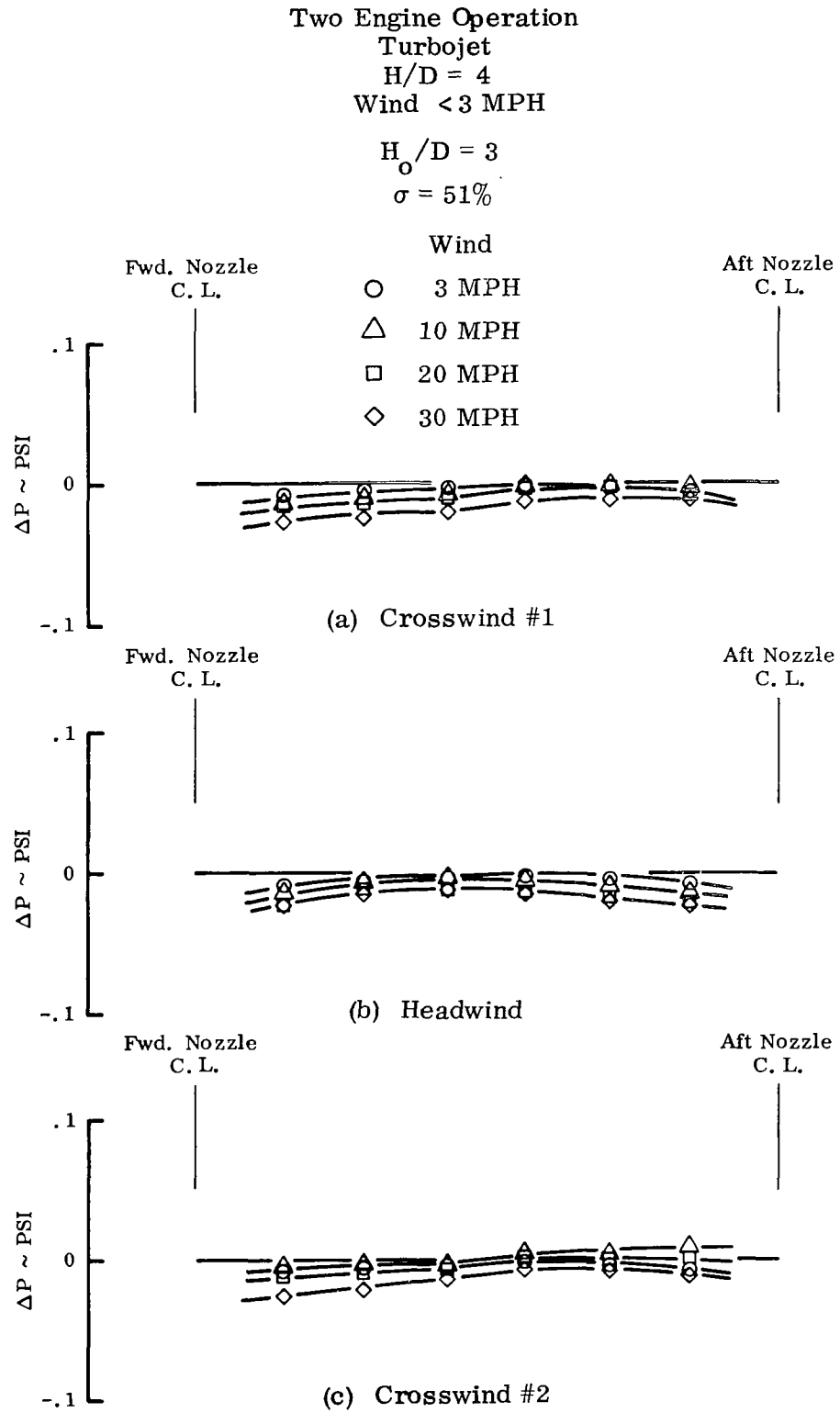

FIGURE 77. EFFECT OF WIND ON POD PRESSURE DISTRIBUTION - GRATE PLUS LOUVERS VECTORED LEFT

NASA-Langley, 1971 — 2 E-6273